Fotonische geïntegreerde circuits en vezelkoppelaars gebaseerd op InP gebonde membranen

Photonic Integrated Circuits and Fibre Couplers Based on InP Bonded Membranes

Frederik Van Laere

Promotoren: prof. dr. ir. R. Baets, prof. dr. ir. D. Van Thourhout
Proefschrift ingediend tot het behalen van de graad van
Doctor in de Ingenieurswetenschappen: Elektrotechniek

Vakgroep Informatietechnologie
Voorzitter: prof. dr. ir. D. De Zutter
Faculteit Ingenieurswetenschappen
Academiejaar 2008 - 2009

UNIVERSITEIT
GENT

ISBN 978-90-8578-244-5
NUR 959
Wettelijk depot: D/2009/10.500/2

Promotoren:

Prof. dr. ir. R. Baets, secretaris	UGent, INTEC
Prof. dr. ir. D. Van Thourhout	UGent, INTEC

Overige leden van de examencommissie:

Prof. dr. ir. D. Dezutter, voorzitter	UGent, INTEC
Prof. dr. ir. H. Benisty	Institut d'Optique, Palaiseau
Prof. dr. ir. M. Smit	TU Eindhoven
Prof. dr. ir. P. Ossieur	UGent, INTEC
Prof. dr. D. Poelman	UGent, Vaste-stofwetenschappen
Dr. ir. D. Taillaert	UGent, INTEC
Prof. dr. ir. G. Morthier	UGent, INTEC

Universiteit Gent
Faculteit Ingenieurswetenschappen

Vakgroep Informatietechnologie (INTEC)
Sint-Pietersnieuwstraat 41
9000 Gent
BELGIUM

Tel.: +32-9-264.33.39
Fax: +32-9-264.35.93

Dit werk kwam tot stand in het kader van een specialisatiebeurs toegekend door het IWT (Instituut voor de Aanmoediging van Innovatie door Wetenschap en Technologie in Vlaanderen)
Part of this work was carried out in the framework of the European IST-FUNFOX project.

Dankwoord

“Ontwerp en realisatie van een kindvriendelijke regenboogkraan”. Toen een onschuldige hand ons dit ontwerpproject Elektrotechniek in tweede proef toewees, waren de reacties verdeeld. Een exotisch onderwerp, dat wel, maar ging dit ooit werken?

Ik kan het meteen verklappen, het heeft nooit echt gewerkt, maar heeft wel in grote mate bepaald dat dit werk hier nu voor u ligt. In die periode ontstond het werkwoord “Intec-en”(of hoe schrijf je dat) en nachtelijke meet -en bricoleersessies deden hun intrede. Het zouden niet de laatste zijn. De interesse voor fotonica was gewekt, een thesis met bijhorende stage in Lyon was de definitieve aanloop naar het echte werk: doctoreren.

Een aantal mensen hebben een grote verdienste aan dit doctoraatswerk. Eerst en vooral mijn promotoren, Roel en Dries, die me de kans gaven om in het FUNFOX project te stappen. Naar verluidt was het niet eenvoudig om bij het definiëren van het project de InP membranen te rijmen met klassieke InP lagenstructuren. Blij dat het toch gelukt is. Roel, veel van jouw ideeën leidden tot samenwerking met andere Europese onderzoeksgroepen, een enorme verrijking. Bedankt! Dries, bij jou kon ik steeds terecht met kleine en grotere problemen. Meestal was je erbij op de vergaderingen, en jouw inbreng heeft dan ook een directe invloed op de inhoud van dit werk. Ook aan jou, enorm bedankt. Dirk, bedankt voor de stevige basis over roosterkoppelaars aan het begin van dit doctoraat. Günther, bedankt voor het aanleren van de bonding technologie en de PDL discussies. Elewout, de kritische vragen tijdens je thesis zitten wellicht hier en daar in dit werk vervat.

Special thanks go to the partners of the EU-FUNFOX project. Among them, Prof. Thomas Krauss and the female part of his group. It was a pleasure working with first Maria, then Melanie and Tiziana, who e-beamed most of the devices in this work. I appreciate the lots of effort you put in these tiny structures, and the high e-beam quality you obtained. Without your e-beam no PhD, so thanks a lot. Also thanks to Prof. Henri Benisty, who coordinated the FUNFOX project, and Cyril and Omer. Your TAMIS is a very rich device, hopefully future collaborations can lead to further improvement. Romain, thank you for letting me measure at Alcatel-Thales III-V lab. Thomas, Henri, thank you for carefully reading and commenting the papers we published together.

Fred, Fouad, Erik-Jan and Meint, the basis for a long-term InP membrane collaboration has been set, hopefully this will result into well-performing active devices. Good luck!

In dit werk werd er heel wat geprocessed, hetgeen vaak leidde tot mooie fotootjes. Voor het eerste verdient Steven Verstuyft een grote pluim: hij leert zijn volk processen. Voor het tweede bedank ik Liesbet, zij behield steeds de glimlach als de BCB weer eens overmatig oplaadde. Voor de sfeer zorgden de collega's, met speciale vermeldingen voor de anciens Vjeeke (die menig balletje mijn richting mikte, een handballer waardig) en Sam tijdens het eerste jaar, en Sjonnie (hoeveel Duvels sta ik nog in het krijt?) en Peter zowat de hele periode. Bedankt gasten, 't was wijs. Voor jullie geen geneurie meer.

De boog kan niet altijd gespannen staan, daar zorgden de uitstapjes met vrienden en allerhande sportactiviteiten wel voor. In de eerste jaren was het verschil tussen studeren en doctoreren niet echt zichtbaar. Wouter, Tom, Benoit en Laurens bleven nog wat plakken, enkel Stijn en Steven kozen voor "het echte leven". Stilaan gaat ieder meer zijn eigen weg, hopelijk blijven we desondanks een hechte vriendengroep. Minivoetbal -en tennisploegmaats, VDRG-vriendjes Nathalie, Jeroen, Joke, Alexander, velen onder jullie vroegen me wat ik nu precies deed, en wanneer het nu eindelijk receptie was. Welnu, the time has come.

Aan mijn ouders en zussen: bedankt voor alles. Opgroeien in een warm nest, jullie aanmoedigingen en steun, het heeft veel voor me betekend, en dat doet het nog steeds. Bedankt ook aan Marc, Chris en Dieter. An-Sofie, de hele periode stond je aan mijn zijde en hielp je me te relativeren als het eens wat minder ging. Nieuwe uitdagingen en projecten staan voor de deur, ik kijk er naar uit om ze samen met jou te verwezenlijken.

Frederik Van Laere
Destelbergen, 10 november 2008

Contents

Contents

Nederlandstalige Samenvatting

1. Fotonische IC's

Vandaag worden we geconfronteerd met een steeds stijgende vraag naar bandbreedte. In dit opzicht blijken elektrische verbindingen te beperkt qua snelheid en capaciteit. Optische communicatie heeft wel het potentieel om aan de vraag naar bandbreedte te voldoen, op voorwaarde dat ze goedkoop en betrouwbaar kan uitgevoerd worden. Miniaturisatie en integratie van verschillende functies op een chip (een fotonisch IC[1]) zijn sleutelbegrippen in deze context. Zowel actieve functies (genereren van licht, detecteren van licht, moduleren, enz) als passieve functies (geleiden van licht, filteren, routeren, enz) dienen voorzien te worden.

Het aantal componenten dat op een bepaalde chipoppervlakte kan geplaatst worden, bepaalt de integratiedensiteit. De mate waarin een optische component kan geminiaturiseerd worden en dus de integratiedensiteit opgedreven kan worden, hangt voor een groot deel af van de optische lagenstructuur waarin de component uitgevoerd wordt. In lagenstructuren met een groot brekingsindexcontrast kan het licht op een zeer efficiente manier opgesloten worden en kan het getransporteerd worden in golfgeleiders met zeer kleine afmetingen (orde enkele honderden nanometer). Bovendien kunnen zeer korte bochten gebruikt worden zonder hoge verliezen te introduceren.

Anders dan in de elektronica waar een enkel materiaal, silicium, wordt gebruikt, zijn er in de optica verschillende materialen mogelijk, elk met bepaalde voordelen afhankelijk van de toepassing. Met het oog op het implementeren van zowel actieve als passieve componenten zijn

---

[1] IC staat voor Integrated Circuit.

III-V halfgeleiders een geschikte keuze. Voor telecommunicatietoepassingen met golflengtevensters rond 1.3 μm en 1.55 μm worden InP en gerelateerde materialen gebruikt. Zij beschikken over een directe bandkloof waardoor op een efficiente manier licht kan gegenereerd worden. Dit is bijvoorbeeld niet het geval bij silicium. Toch krijgt silicium veel aandacht voor toepassing in optische communicatie omdat gebruik kan gemaakt worden van geavanceerde fabricagetechnieken uit de electronicawereld. Voor de actieve functies moet silicium dan gecombineerd worden met III-V materiaal.

In dit werk worden zowel de actieve als de passieve functies in InP gebaseerd materiaal geïmplementeerd. Nadeel van klassieke InP gebaseerde lagenstructuren is hun laag vertikaal brekingsindexcontrast, waardoor de integratiedensiteit beperkt wordt. Het is echter mogelijk om over te stappen naar zogenaamde membraanstructuren die wel een hoog vertikaal brekingsindexcontrast hebben. In dit werk worden InP membranen gebruikt als optische lagenstructuur. Ze worden verkregen door BCB bonding en combineren de voordelen van een hoog brekingsindexcontrast (hoge integratiedensiteit) met de mogelijkheid tot het efficiënt implementeren van zowel actieve als passieve functionaliteit.

2. Het koppel -en polarisatieprobleem

Elke fotonisch IC dient gekoppeld te worden met de buitenwereld. In de praktijk betekent dit meestal een koppeling tussen een optische vezel en een golfgeleider op de chip. Door het grote verschil in afmetingen tussen beide is dit verre van triviaal en het probleem wordt enkel groter aangezien de afmetingen van de golfgeleiders en componenten steeds kleiner worden.

Een bijkomend probleem is dat de werking van een optische component vaak verschillend is voor verschillende polarisaties van het licht. Deze polarisatie-afhankelijkheid is zeer uitgesproken bij structuren met een hoog brekingsindexcontrast en de technologische vereisten om ze op te heffen zijn in de praktijk niet haalbaar. De polarisatie van het licht dat uit de vezel komt in een telecommunicatienetwerk is echter een onbekende grootheid die bovendien varieert in de tijd. Dus zelfs indien de koppeling tussen vezel en chip polarisatie-onafhankelijk kan gemaakt worden, blijft de polarisatie-afhankelijkheid van de componenten op de chip een probleem. Er kan dan immers licht met een polarisatie ingekoppeld worden waarvoor de chip niet of onvoldoende werkt.

3. Roosterkoppelaars en polarisatie-diversiteit

Voor beide problemen wordt een oplossing geboden door het gebruik van roosterkoppelaars, waarbij het licht uit de vezel via een compact rooster op de chip in een golfgeleider wordt gediffracteerd (Figuur 1a). Het grootste voordeel ten opzichte van klassieke methodes die langs de zijkant van de chip inkoppelen, is de mogelijkheid tot testen op waferschaal. Op elke plaats op de chip kan een ingang of uitgang geplaatst worden, waardoor afzonderlijke componenten eenvoudig kunnen getest worden. Dit heeft een positieve invloed op de uiteindelijke opbrengst en kostprijs van de chip.

Roosterkoppelaars tussen optische vezel en golflgeleiders op de chip werden reeds ontwikkeld voor Silicium-op-Isolator (SOI) lagenstructuren. De experimenteel aangetoonde koppelefficiëntie is echter beperkt tot 31%. De totale lengte van de koppelstructuur wordt bepaald door een relatief lange adiabatische overgang tussen een 12 μm brede golfgeleider en een 500 nm brede golfgeleider. In dit werk wordt de koppelefficiëntie gevoelig opgedreven en de lengte van de koppelstructuur beperkt. In enkele gevallen dient SOI als testplatform voor InP membraanstructuren. Door een gouden bodemspiegel te introduceren kan een theoretische efficiëntie van $\approx$ 80% behaald worden. Experimenteel tonen we een efficiëntie van 69% aan voor SOI en 60% voor InP membranen. De adiabatische overgang tussen brede en smalle golfgeleiders wordt overbodig door het gebruik van focusserende roosters, hetgeen resulteert in een achtvoudige lengtereductie van de koppelstructuur.

Een tweedimensionaal rooster in combinatie met twee golfgeleiders wordt gebruikt om polarisatie-diversiteit te implementeren (Figuur 1b), de meest elegante manier om het polarisatieprobleem op te lossen. De beide orthogonale polarisaties van het licht in de vezel worden gesplitst en gekoppeld naar hun specifieke golfgeleider. In de golfgeleiders zijn de polarisaties identiek, en beide leiden naar een identieke polarisatie-afhankelijke component. Aan de uitgang wordt het licht in beide golfgeleiders opnieuw samengevoegd met een volgende roosterkoppelaar. Ook in deze configuratie wordt de koppelefficiëntie opgedreven en de koppelstructuur geminiaturiseerd.

4. Geïntegreerde componenten in InP membraan

De hierboven beschreven roosterkoppelaars worden gebruikt om te koppelen naar een reeks geïntegreerde componenten op InP membraan,

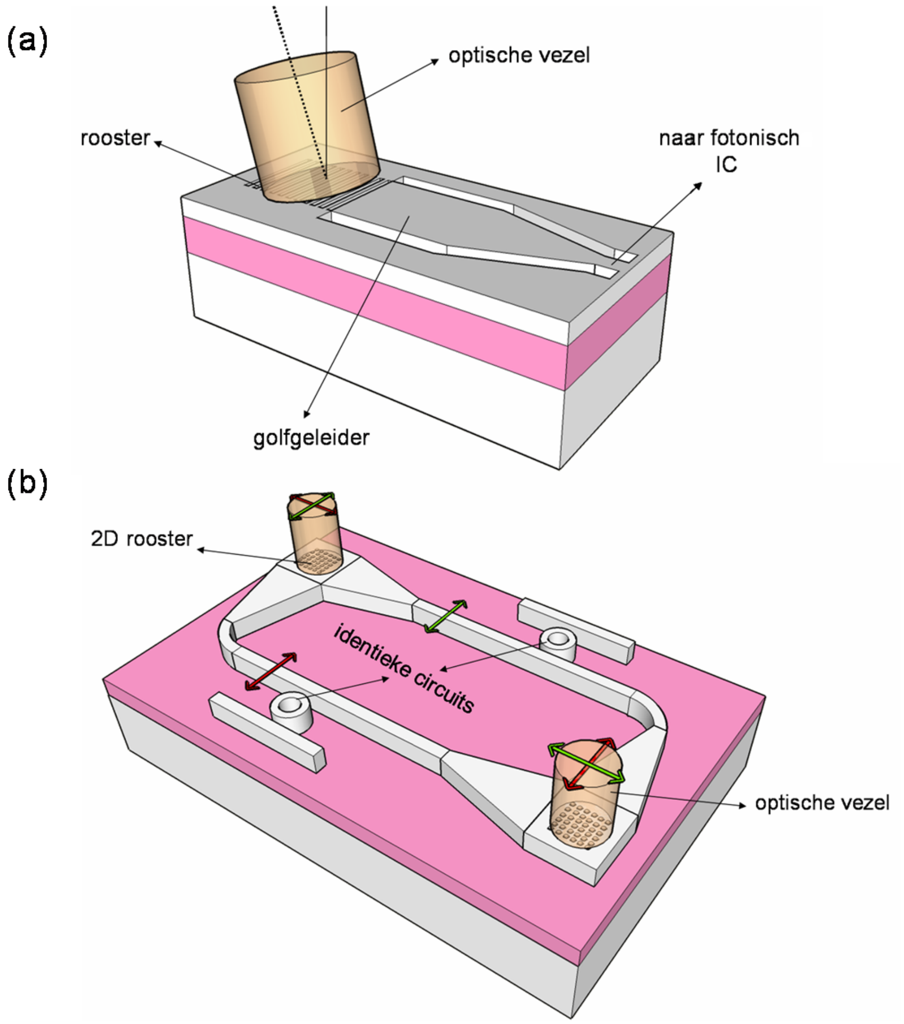

Figuur 1: Roosterkoppelaars tussen optische vezel en nanofotonische golfgeleiders. (a) Koppelprincipe. (b) Configuratie voor polarisatiediversiteit.

zowel gebaseerd op klassieke golfgleiders als fotonische kristallen. De membranen worden bekomen door een gestructureerde InP chip te bonden op een drager met behulp van een tussenliggende polymeerlaag (BenzoCycloButene, kortweg BCB), en daarna het oorspronkelijke InP substraat te verwijderen.

Passieve componenten als vermogensplitsers, ring resonator filters, en een fotonisch kristal gebaseerde golflgengte demultiplexer worden gedemonstreerd. Aan de actieve zijde worden efficiënte detectoren geïntegreerd op het InP membraan platform, die gebruikt worden om andere componenten te karakteriseren. De geïntegreerde functies worden ook telkens in polarisatie-diversiteit configuratie geïmplementeerd, waarbij speciale aandacht geschonken wordt aan de invloed van inkoppeling onder een hoek afwijkend van vertikale positie. Een coherente ontvanger chip, waarbij een telecom signaal gemengd wordt met een lokale oscillator, vormt de finale demonstratie van de ontwikkelde InP membraantechnologie.

English Summary

1. Photonic ICs

Nowadays, we are confronted with an ever growing quest for bandwidth. Electrical interconnections are too limited regarding speed and capacity. Optical communication, however, has the potential to fulfill the bandwidth requirements, provided that it can be implemented in a cheap and reliable way. Miniaturisation and integration of different functions onto a single chip (a Photonic Integrated Circuit or PIC) are key words in this context. Both active functions (light generation, light detection, modulation, . . .) and passive functions (guiding of light, filtering, routing, . . .) need to be provided.

The number of components that fit onto a certain chip area determines the integration density. The amount of miniaturisation of an optical component, and therefore the integration density, depends on the optical layer structure in which the component is implemented. Light can be confined to small structures when using high refractive index contrast layer structures, and can be transported in waveguides having dimensions of a few hundreds of nm. In addition, compact bends can be used without introducing excess loss.

Unlike in electronics where a single material, silicon, is used, there are a lot of possible materials for photonic integrated circuits, each having advantages depending on the application. With respect to implementing active functions, III-V semiconductors are the obvious choice. For telecommunication applications, with wavelength windows around 1.3 μm and 1.55 μm, InP and related materials are being used. They exhibit a direct bandgap, as a result of which light can be generated in an efficient way. This is not the case for silicon. However, silicon attracts a lot of attention since advanced fabrication processes can be borrowed from electronics. For active functionality, silicon then needs to be combined with III-V material.

In this work both active and passive functions are implemented in InP based material. A disadvantage of classical InP based layer structures is their low vertical refractive index contrast, limiting the achievable integration density. However, it is possible to use so-called membrane structures having a high refractive index contrast. In this work InP membranes are used as the optical layer structure. They are obtained by BCB bonding and combine the advantages of a high refractive index contrast (high integration density) with the possibility to efficiently implement both active and passive functionality.

2. The coupling -and polarisation problem

Each PIC needs to be connected with the outside world. In practice, this means coupling between an optical fibre and a waveguide on the chip. Due to the large difference in dimensions between both, this is far from trivial and the problem becomes even worse since the dimensions of the on-chip waveguides and components tend to become smaller.

An additional problem is the fact that an optical component operates differently for different polarisations of the light, especially when using high index contrast. The fabrication tolerances required to cancel this polarisation dependence are too stringent in practice. The polarisation of light coming from the fibre in a telecommunication network is an unknown quantity and varies randomly over time. So even if the coupling between fibre and chip can be made polarisation independent, the polarisation dependency of the on-chip components remains a problem. There can be a mismatch between the polarisation of input light from the fiber and the polarisation for which the component works properly.

3. Grating couplers and polarisation diversity

In this work a solution for both problems is given by using grating couplers, where light from a fibre is diffracted from the top into a waveguide on the chip (Figure 2.1a). The main advantage over classical methods using edge coupling is the possibility for wafer-scale testing. An input or output can be placed anywhere on the chip and separate devices can be tested in a simple way. This has a positive influence on the yield and the price of the chip.

Grating couplers between optical fibre and on-chip waveguides have already been developed for Silicon-on-Insulator (SOI) layer structures prior to this work. The experimental coupling efficiency is limited to 31%. The total length of the coupling structure is determined by a relatively long adiabatic transition between a 12 μm wide waveguide and a 500 nm wide photonic wire. In this work the coupling efficiency is substantially increased and the length of the coupling structure is decreased. In a few cases, SOI serves as a test platform for InP membrane structures. By introducing a gold bottom mirror a theoretical efficiency of $\approx$80% can be achieved. We show experimental coupling efficiencies of 69% for SOI and 60% for InP membrane. The adiabatic transition between wide and narrow waveguides can be omitted through focusing grating couplers, resulting in an eight-fold length reduction of the coupling structure.

A two-dimensional grating in combination with two waveguides is used to implement polarisation diversity (Figure 2.1b), the most elegant way to solve the polarisation problem. Both orthogonal polarisations of the light from the fibre are splitted and coupled to their own waveguide. In the waveguides the polarisation is identical and both feed an identical polarisation dependent device. At the output the light from both waveguides is recombined using another grating coupler. Also in this configuration, the coupling efficiency is increased and the coupling structure is miniaturised.

4. Integrated devices on InP membrane

The grating couplers described above are used to couple to a series of integrated devices on InP membrane, based on both classical waveguides and photonic crystals. The membranes are obtained by bonding a structured InP die onto a carrier substrate using an intermediate adhesive polymer layer (BenzoCycloButene or BCB), and afterwards removing the original InP substrate.

Passive components like power splitters, ring resonator filters and a photonic crystal based wavelength demultiplexer are demonstrated. At the active side, efficient detectors are integrated onto the InP membrane platform and used for characterising other integrated devices. The integrated functions are also implemented in polarisation diversity configuration, paying special attention to the influence of coupling under an angle. A coherent receiver chip, where a telecom signal is

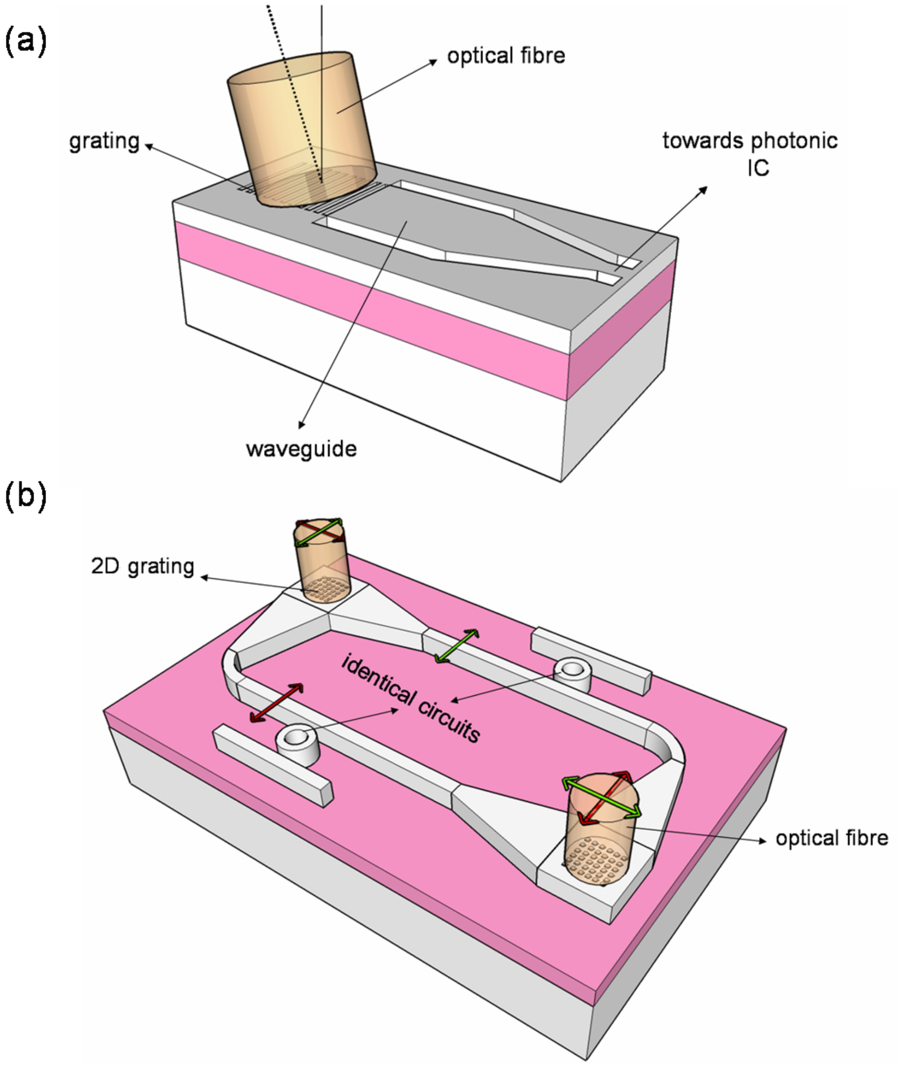

Figure 2: Grating couplers between optical fibre and nanophotonic waveguides (a) Coupling principle. (b) Polarisation diversity configuration.

mixed with a local oscillator signal, is the final demonstration of the developed InP membrane technology.

English Text

Chapter 1

Photonic integration

In this chapter we will describe the important aspects of the research carried out in this work. We first discuss integrated circuits in general. Afterwards, the materials and the relevant integration techniques are described. We then discuss two important issues in photonic integrated circuits for which we provide a solution in this work: fibre coupling and polarisation. After putting together all these elements we will motivate the choice for the used layer structure, i.e. a high index contrast InP membrane.

1.1 Optical telecommunication

Nowadays, communication is everywhere. Games can be played online between people that are thousands of kilometers apart, videos are streamed or downloaded over the internet, people abandon the classical telephone and replace it by “skype”, etc. This series of new applications results in an ever increasing quest for bandwidth and optical communication is the way to provide it.

Two inventions have initiated the field of optical telecommunication. In 1960 the first laser was demonstrated, which would become the winning light source. In 1970 an optical fibre with low enough attenuation (20 dB/km) was developed. Today the optical fibre loss has decreased to values around 0.2 dB/km. Together with other improvements (e.g. on dispersion) and the large available bandwidth, this makes the optical fibre the uncontested long-haul transport medium for light signals. The used wavelength windows are situated around 1550 nm and 1310 nm, where respectively propagation loss and disper-

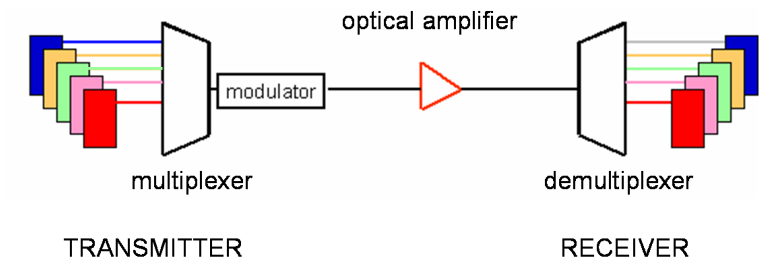

Figure 1.1: Optical communication link using Wavelength Division Multiplexing (WDM).

sion are minimal. While in the past the fibre was mostly used for long distance communication, it is now brought closer to the end user to overcome the limitations of electrical interconnections. This approach is called Fibre-To-The-Home (FTTH) and is already widely installed in Japan and the US.

The large capacity of the optical fibre can be exploited by transporting different signals on different wavelengths over a single fibre. This is called Wavelength Division Multiplexing (WDM). In [1], 140 111 Gb/s signals are transmitted over 160 km distance, resulting in an enormous capacity of 14 Tb/s. A multiplexer is used to bring the different signals onto the fibre at the transmitter side, a demultiplexer separates the signals at the receiver side. In Figure 1.1 a typical WDM link between transmitter and receiver is shown. A difference is made between two types of WDM systems based on the channel spacing: Coarse WDM (CWDM) uses larger channel spacing than Dense WDM (DWDM). In this work we will demonstrate a demultiplexer for CWDM applications.

1.2 Photonic Integrated Circuits (PICs)

In analogy with electronics, there is a trend in photonics towards integrating different components with different functionality onto a single chip. For WDM applications, this includes both active (light emission, detection, modulation, amplification) and passive functionality (waveguiding, wavelength (de)multiplexing, switching, etc). The advantages of this approach are multiple. Among others:

- Since photonic integration obviates the need for individual components, the number of packages is reduced substantially. And since the packaging cost of an optical component typically amounts for at least 50-80% of the total cost, integrated solutions are far more cost effective.

- The light is transported between different on-chip components using waveguides[1]. This implies that there is no need for difficult, time consuming and costly alignment between components, as alignment is done through lithographic processes during pattern definition.
- The coupling with the outside world (optical fibre) is typically a point of failure and potentially a source of loss. In integrated circuits the number of fibre couplings is highly reduced.

We can conclude that photonic integrated circuits are more cost effective, better performing, and more reliable than their non-integrated counterparts.

An important aspect of integrated circuits is their integration density, which is defined as the number of components per given chip area. The smaller the individual components and their interconnection, the higher the integration density that can be achieved and the more profit is gained from the integration effort. The achievable integration density is mainly determined by the layer structure. A good measure is the minimum waveguide bending radius that can be used without excess loss. For waveguides with a high refractive index contrast, the light is highly confined and the bending radius can be very small. For layer structures with a low index contrast, the achievable integration density is much lower. We will give examples of both types of layer structures in the next section.

1.3 Materials for photonic integrated circuits

Unlike in electronics where silicon is the workhorse for integrated circuits, there are a lot of materials that can be used for making photonic integrated circuits. Most widely used are silica-on-silicon, III-V materials like GaAs/AlGaAs and InP/InGaAsP, $LiNbO_3$, polymers and silicon. Each material has its advantages and disadvantages, the choice

---

[1] A waveguide is a tiny structure on the chip where the light is confined in a region with higher refractive index contrast as compared to the surrounding cladding material.

often depending on the application that is envisioned. For implementing integrated circuits featuring a variety of active and passive functions, semiconductors are most used. In GaAs/AlGaAs both active and passive functions can be implemented, but due to the bandgap the use is limited to wavelengths around 850 nm and 980 nm. In this work, silicon and InP based integrated circuits will be considered, which can be used at the telecom wavelength windows (around 1.3 μm and 1.55 μm).

1.3.1 Substrate type layer structures

In what we will call substrate type layer structures in this work, the layers are epitaxially grown onto a single substrate. The InP/ InGaAsP material platform is an example of this type of structure, the layers being epitaxially grown lattice matched onto an InP substrate. Substrate type layer structures typically have a medium to low vertical index contrast and therefore a relatively weak vertical confinement. A passive waveguide consists of an InGaAsP core surrounded by InP cladding layers (Figure 1.2a), resulting in a vertical index contrast of $\sim$ 3.3:3.17. The lateral index contrast can be influenced through etching. The minimum bend radius is a few hundred μm. Besides passive functions, also active functions with high performance can be implemented in the telecom wavelength windows due to the direct bandgap of InP based material.

From a technological point of view InP processes are not as advanced and reliable as is the case for silicon (which benefits from electronics), and the volumes that can be obtained are smaller. Additionally, InP is rather expensive.

1.3.2 Membrane type layer structures

Membrane type layer structures have a high vertical index contrast, and therefore a strong vertical confinement. In the last decade, silicon-on-insulator (SOI) has gained a lot of interest for use in high density integrated circuits. It consists of a silicon guiding layer on a buried oxide layer, carried on a silicon substrate, resulting in an index contrast of 3.45:1.45 and 3.45:1.0. An overview of different methods for obtaining SOI structures can be found in [2]. Typical dimensions of a single-mode photonic wire waveguide (or strip waveguide) are of a few hundred nm. Due to the high confinement, the minimum bending radius can be as low as 5 μm. In Figure 1.2b an SOI photonic wire is shown.

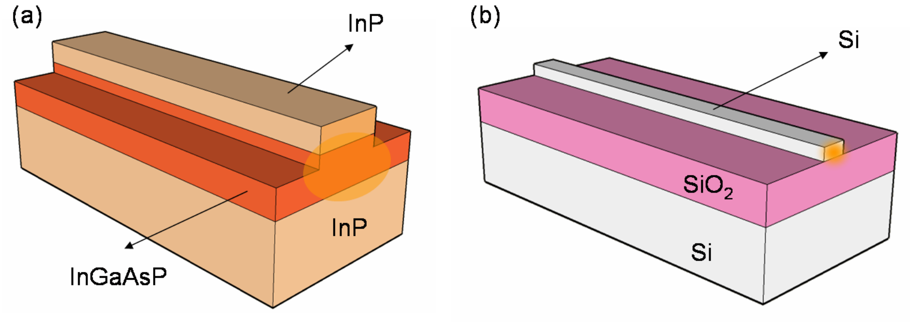

Figure 1.2: (a) Substrate type rib waveguide in InP/InGaAsP. (b) Membrane type SOI photonic wire.

For the fabrication of SOI circuits, standard CMOS processes from electronics can be used, which are very mature and allow mass production. Additionally, the optical layer can be integrated with a CMOS electronic layer. The advance on passive devices in Silicon-on-Insulator in the last few years is striking [3, 4, 5, 6]. Also active functions like detectors based on Ge on silicon [7, 8] and modulators [9] have been demonstrated. However, light emitting devices are very difficult to achieve in silicon. In contrast to InP, silicon has an indirect band gap, which makes light emission very inefficient. Although some demonstrations of silicon based light sources have been reported [10, 11], they are still outperformed by their III-V based counterparts.

Membranes can also be obtained in various other materials than silicon through bonding or local underetching. A particular field where suspended membranes are widely used are MOEMS[2] [12]. For some applications it is compelling to combine the strong confinement offered by the membrane based approach with the active functionality of III-V material, for example in [12, 13]. This will be further discussed below.

1.4 Integration techniques

The success story of electronics can be related to the fact that only one base material (i.e. silicon) and only a few base components (e.g. transistor, resistor, capacitor) are used. The situation is totally different for optical applications and as a result different integration techniques exist.

---

[2] Micro-opto-electromechanical systems.

1.4.1 Monolithic integration in InP/InGaAsP

In monolithic integration all devices and functions are implemented from a single piece of wafer. For optical telecom applications, InP based layer structures are used, as they can implement both passive and active functions in the 1.3 μm and 1.55 μm wavelength range. Monolithic integration in InP typically uses substrate type layer structures. The advantages of monolithic integration include high reliability (as no other materials are involved) and relative ease of coupling between components (as no coupling between different materials is needed). However, it is difficult to combine electronics with monolithically integrated InP/InGaAsP components.

Several techniques exist for monolithic active-passive integration in substrate type InP based material. In butt-joint coupling [14], the active layers are grown in a first epitaxial growth step and afterwards removed in the passive regions by wet etching. The passive layers are then grown in a next epitaxial step, aligned to the active region. Active and passive waveguides are butt-coupled. Another possibility is using the twin-guide approach, where an active and a passive waveguide layer are vertically stacked. Coupling between both is performed by using tapers [15, 16]. Other methods are selective area growth [17], quantum well intermixing [18] and offset quantum wells [19].

A number of issues, most importantly related to InP processing, have prevented the large breakthrough of monolithically integrated circuits based on InP. The above described processes are often rather complex, resulting in yield problems and high costs. However, Infinera [20], a company selling monolithically integrated InP based circuits, has now demonstrated a transmitter for DWDM applications by monolithically integrating 10 DFB lasers with 10 modulators at 40 Gb/s with a WDM demultiplexer, resulting in a total capacity of 400 Gb/s [21].

1.4.2 III-V/silicon integration

A promising approach is to built an integrated circuit with passive functions in membrane type SOI (thus profiting from advanced CMOS technology and enabling high density integration) and active functions in III-V material (InP based for telecom applications).

The SOI circuit and the active device have to be integrated and coupled using some integration technology. In flip chip bonding technology, individual sub-components are mounted onto the silicon substrate [22]. This approach is also referred to as hybrid integration. However, this piecewise assembly technique is very labour intensive and alignment tolerances are very tight. Luxtera [23], a fabless company active in silicon photonics, launched its first product in 2007: a 40 Gb/s optical active cable. They use flip chip technology for integrating a laser source onto the CMOS electronic-photonic chip. Another possibility for integrating III-V on silicon is hetero-epitaxial growth [24], but due to the lattice mismatch between both materials, fabrication processes are difficult. A third method uses bonding of III-V layers onto silicon, which does allow for high density integration and high quality III-V layers [25, 26]. This approach is referred to as heterogeneous integration and is a wafer-scale technique rather than the pick-and-place technique used in hybrid integration. In principle, the active device can be implemented both in membrane or substrate type III-V layer structures. However, it is very difficult to use electrical injection for membrane type active devices due to the presence of absorbing metal contacts near the optical mode. Heterogeneous III-V/silicon integration is very promising, but is still at a research stage.

Advantages of integrating different material systems include the possibility of using optimised components in their optimal layer structure, flexibility and the possibility of combining electronics and photonics. Disadvantages include the need of processing and coupling between different material systems, alignment issues in some technologies and possibly decreased reliability.

1.4.3 InP based membranes

Another option is using III-V membranes, in order to combine the advantages of high refractive index contrast with the capability of implementing active functions efficiently. Both active and passive functions can then be implemented in InP based material, without the need for processing different materials and couple between them. Passive devices are advantageously implemented in membrane type structures, while for the active devices both membrane and substrate type structures are possible. The latter approach can be seen as a mixture of monolithic and heterogeneous integration: only InP based material is used, but integration of membrane type and substrate type layer structures is required.

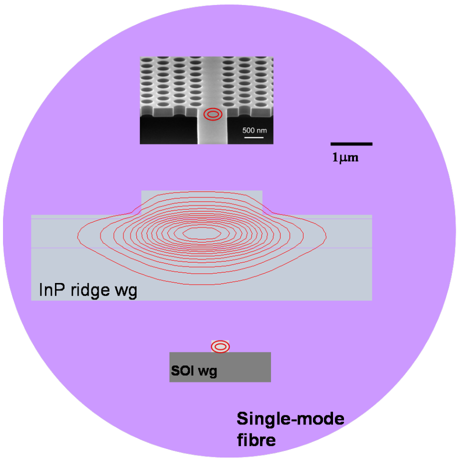

Figure 1.3: The coupling problem.

1.5 Coupling to optical fibre

In order to be of any use, optical signals must be extracted from and launched into the integrated circuit. Therefore, the connection with the outside world, i.e. optical fibre, is an important but non trivial task. A good fibre coupling solution must fulfill criteria as having a low coupling loss, large optical bandwidth, good alignment tolerances and being tolerant to fabrication. The coupling typically occurs between the optical fibre and a waveguide on the chip. Naturally, this coupling depends on the geometry of the waveguide which depends on the layer structure used.

The most important issue in fibre coupling is the mismatch between the fibre mode and the optical waveguide mode on the chip (Figure 1.3). The mode of a single-mode fibre (SMF-28) has a diameter of $\sim$ 8-10 μm and a circular field profile, while the dimensions of the on-chip waveguide modes are substantially smaller and the field profile is elliptic. Simple butt-coupling between fibre and waveguide results in unacceptable losses. As described above, the waveguides are different for membrane type and substrate type layer structures due to the difference in refractive index contrast. In the next sections we will describe the methods commonly used for fibre coupling to both types of waveguides. We will only consider integrated solutions as they are an important factor in reducing alignment tolerance and packaging costs.

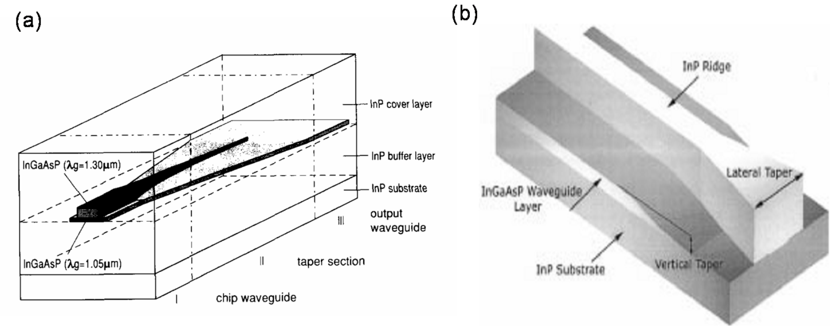

Figure 1.4: Coupling between fibre and substrate type waveguides using tapers. (a) Dual lateral overlapping buried taper (from [29]). (b) Vertical+lateral taper (from [19]).

1.5.1 Coupling to substrate type waveguides

In this case a coupling structure is required between the fibre mode with diameter of 8-10 μm and a waveguide with dimensions of a few μm. Nowadays the fibre coupling for this type of waveguides is well established, the most popular approaches being based on monolithically integrated spot-size converters and edge coupling. By gradually reducing the size of the waveguide (tapering), the mode can be transformed from small to large. If this transition is done gently, the fundamental mode of the small waveguide is transformed into the fundamental mode of the wider waveguide (or vice versa) without theoretical loss. The transition is then called adiabatic.

There exist a variety of taper designs, and a good overview is given in [27]. Both lateral tapers, vertical tapers or a combination can be used. Their fabrication requires regrowth in most cases and the structures are often polarisation dependent. In [28], a 2D overlapping waveguide taper transition from a buried waveguide to a fibre matched waveguide is used for obtaining a coupling loss of -0.4 dB, with a lateral alignment tolerance of 2.7 μm for 1 dB excess loss. In [29], a 560 μm long dual lateral overlapping buried waveguide taper is used for obtaining a coupling loss smaller than -1.1 dB (Figure 1.4a). In [19], a coupling loss of -1.55 dB to cleaved single-mode fibre and large alignment tolerance is obtained using a combination of vertical and lateral tapers (Figure 1.4b).

In Chapter 2 we will propose a different approach for coupling to substrate type waveguides using vertical coupling rather than edge coupling.

1.5.2 Coupling to membrane type waveguides

In the case of membrane photonic wires a coupling structure is required between the fibre mode with diameter of 8-10 μm and a waveguide with dimensions of a few hundred nanometer. Most of the coupling methods described below are for SOI photonic wires, but their operation principle can be easily transferred to other membrane waveguides.

A first possible solution is the use of adiabatic tapers. In [30], a 600 μm long 3D taper was used to obtain a coupling loss between fibre and photonic wire of -2.2 to -3.5 dB. However, the fabrication process is very difficult. A more elegant coupling structure is the inverted taper (Figure 1.5a). Here, the waveguide is tapered to a width of a few tens of nm. As a result, the waveguide mode is squeezed out of the wire waveguide into another waveguide which is better matched to the fibre. The difficulty lies in the lithography of the narrow taper tips. In [31], a coupling loss of -0.8 dB has been obtained between square cross-section photonic wires and high numerical aperture fibre using a 200 μm long taper and a polymer overlay waveguide. The same approach by IBM [32] has resulted in a coupling loss of -0.5 dB using lensed fibre and a taper of 150 μm length. In [33], the buried oxide layer instead of an overlay waveguide was used to delocalise the mode. The taper has a length of 40 μm, and the coupling loss is -3.3 dB (for TM-like modes) and -6.0 dB (for TE-like modes).

Another type of coupling structure is a grating assisted directional coupler. A practical realisation achieving an experimental coupling loss of -2.6 dB is described in [34] (Figure 1.5b). The light from the optical fibre is first butt-coupled with very low loss to a fibre adapted waveguide. Then, the light is coupled to an intermediate Si_3N_4 waveguide using a first grating, and to an SOI photonic wire using the second grating. However, the gratings have lengths ranging from few hundred μm to 1 mm, the structure is sensitive to polarisation and has a small optical bandwidth.

Another approach is based on waveguide grating couplers. Light is coupled from the top into the waveguide by using a diffraction grating. This approach has several advantages over the above mentioned edge coupling methods. A cleaved facet is not required and coupling can oc-

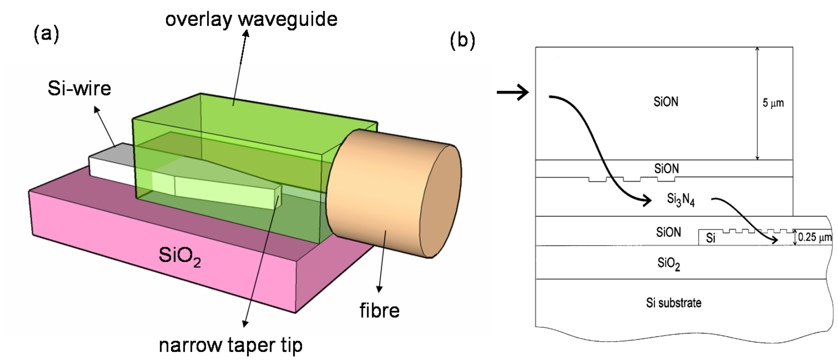

Figure 1.5: Coupling between fibre and membrane type waveguides. (a) Inverted taper with overlay waveguide. (b) Dual grating assisted coupling (from [34]).

cur everywhere on the chip. This opens the way for wafer-scale testing of devices, which reduces the cost of the integrated circuit dramatically. Drawback is a relatively small optical bandwidth. Previously reported grating couplers are either long [35] or need additional lenses to couple to fibre, since coupling to wide Gaussian beams is considered [36, 37]. In [38], compact slanted grating couplers are described having a theoretical coupling loss of -1.2 dB, but no experimental results are given.

In the PhD work of D. Taillaert [39], compact grating couplers for coupling between SMF-28 fibre and SOI photonic wires were designed and fabricated. The grating dimensions are of the order of the fibre mode ($\sim$ 10 x 10 μm^2) resulting in a 1 dB optical bandwidth of 45 nm. Furthermore, the alignment tolerances are relaxed (+/- 2 μm for 1 dB excess loss). However, a lateral spot-size convertor toward a single-mode photonic wire is still required (Figure 1.6). Although designs are described achieving coupling losses smaller than 0.4 dB, the experimental coupling loss is -5.2 dB, which is too low for practical applications. In this work, we will substantially increase the coupling efficiency of the grating coupler and avoid the in-plane spot-size convertor. Finally, we mention that the 1D grating coupler is very polarisation sensitive but a 2D grating can be used in a polarisation diversity configuration (see below).

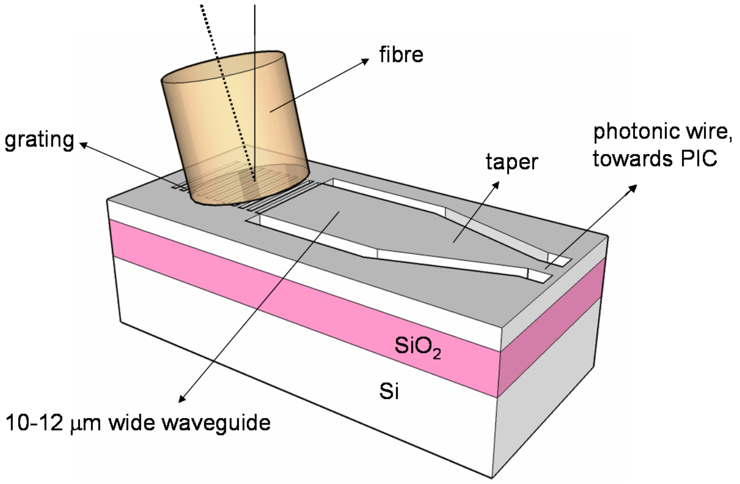

Figure 1.6: Coupling between fibre and membrane type waveguides using grating couplers. The waveguides are defined by trenches.

1.6 Polarisation

Polarisation dependence of on-chip components is another important issue in photonic integrated circuits. This polarisation dependence is mainly due to waveguide birefringence. The polarisation of the light in an optical fibre, however, is an unknown quantity which also changes during propagation due to cross-coupling between the two polarisation modes. So even if the fibre coupling can be made polarisation independent, there can still be a mismatch in polarisation between incoming light from the fibre and the polarisation needed on the chip. Polarisation Maintaining Fibre (PMF) is not a viable solution, as it can only be used for short distances and is more expensive than single-mode fibre. Several other solutions have been proposed. Most of the principles can be applied to both membrane type and substrate type structures, although the implementation is different.

The most obvious solution is to make the on-chip components polarisation insensitive by making the waveguides and all other functions polarisation independent. This can be done by fabricating symmetrical waveguides, for which an example is given in [40]. Although simple in concept, this is far from trivial in practice, especially when using membrane type photonic wires. For membrane photonic wires with dimensions of a few hundred nm, the tolerances on fabrication are almost impossible to achieve. Rib waveguides have a lower index contrast and larger cross-sections, and can be made polarisation independent more easily. This is illustrated in [41], where a polarisation independent ring resonator based on rib waveguides is demonstrated. Also the coupling to fibre is easier, but the achievable integration density is lower. Therefore, we will not consider them further.

Other approaches to overcome polarisation dependence are inserting a half-wave plate in the middle of the device [42], using layer structures with low birefringence [43] or implementing polarisation compensation through inserting a region in the device with different birefringence [44, 45, 46, 47]. The most robust approach, however, is polarisation diversity. This is the approach used in this work and we will describe the principle in the next section.

An important measure for the extent to which polarisation insensitivity is obtained, is the Polarisation Dependent Loss (PDL). This quantity is determined by the difference in peak transmission of the optical device, when varying the polarisation over all possible polarisation states:

$$PDL(dB) = 10 \log \left(\frac{T_{max}}{T_{min}}\right) \tag{1.1}$$

Polarisation diversity

The principle of polarisation diversity is shown in Figure 1.7. The (random) polarisation of the incoming light is split into its two orthogonal polarisation states. One polarisation is then rotated by 90°, resulting in two channels with identical polarisation. Both arms feed an identical polarisation sensitive device (A and B in Figure 1.7), and at the output one polarisation is rotated by 90 degrees. Finally, both now orthogonal polarisations are recombined (without interference).

Several realisations of integrated circuits using polarisation diversity have been shown. In [48], a polarisation independent add-drop filter based on ring resonators is demonstrated for silicon-rich SiN waveguides. The PDL is 1.0 dB over a 60 nm bandwidth. A 600 μm long polarisation splitter and rotator is integrated onto the chip (Figure 1.8), and no details are given on fibre coupling. In [49], a polarisation independent wavelength filter based on SOI photonic wire ring resonators is demonstrated using polarisation diversity. The PDL of the filter is about 1 dB. The total length of the polarisation diversity structure is around 250 μm, including spot-size convertor for fibre coupling (200 μm) [31], polarisation splitter (10 μm) and polarisation rotator (30-60 μm). Isolated realisations of polarisation splitters and rotators without

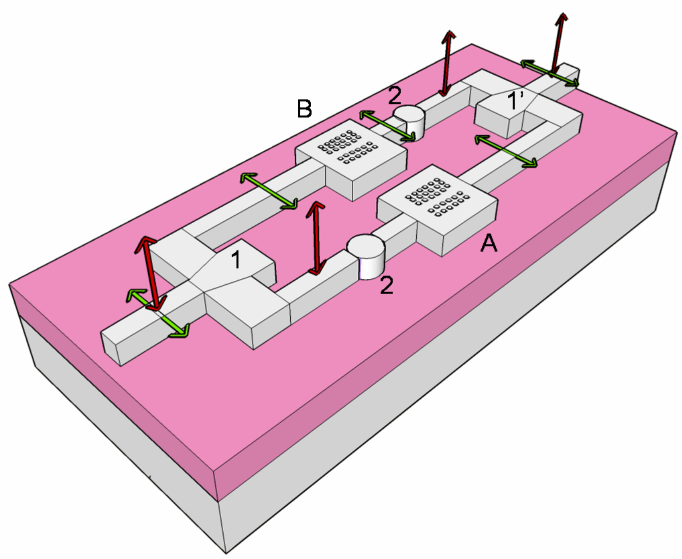

Figure 1.7: Principle of polarisation diversity. 1=polarisation splitter, 1'=polarisation combiner, 2=polarisation rotator, A and B are identical polarisation sensitive devices.

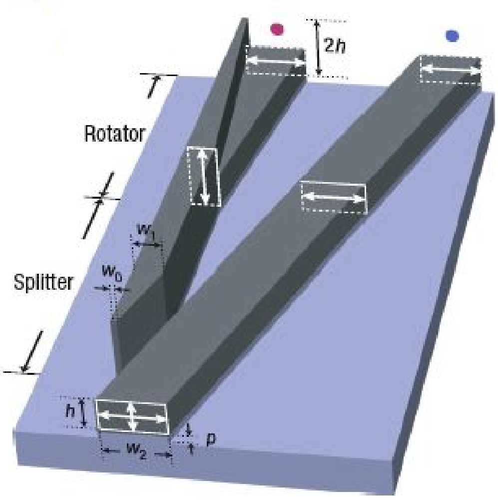

Figure 1.8: Integrated polarisation splitter and rotator for polarisation diversity (from [48]).

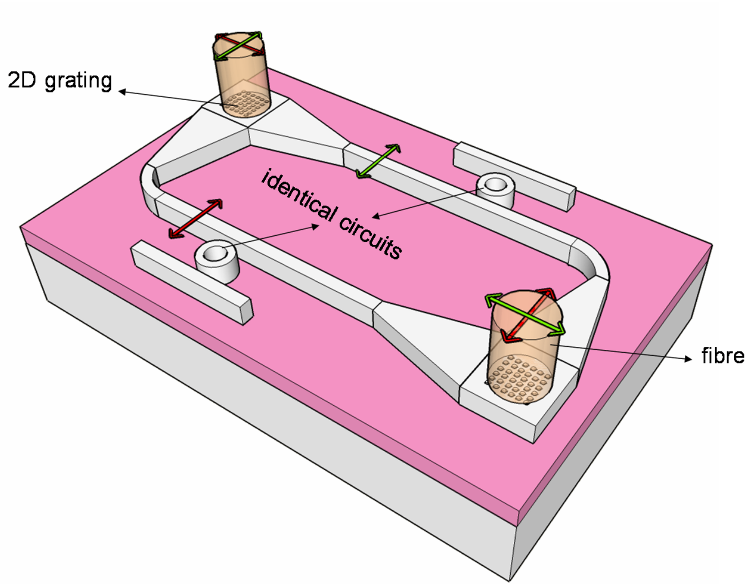

Figure 1.9: Polarisation diversity using 2D grating couplers.

application in a polarisation diversity circuit have also been demonstrated, both for InP/InGaAsP [50, 51, 52] and SOI waveguides [53, 54, 55]. Even though some of the devices are compact, the required combination of polarisation independent fibre coupling, polarisation splitting and rotating always results in a lengthy and/or lossy device.

We will use a 2D crossed grating coupler for performing polarisation diversity, without the need for integrated polarisation splitters and rotators. The polarisation sensitivity of a grating coupler is used to separate the orthogonal polarisation components of the incoming light into two (near) orthogonal waveguides [56]. In these waveguides the polarisation is identical (TE). The polarisation sensitive device (working for TE-polarisation) is then duplicated, one in each waveguide arm, and at the output another 2D grating is used for recombining both arms (Figure 1.9). This approach is the most compact, and will extensively be described in Chapter 6.

1.7 Substrate approach vs membrane approach

In the previous sections we have described different material platforms and we have given examples of integrated circuits. We have also touched

	substrate (e.g. InP/InGaAsP)	membrane (e.g. SOI)
layer structure	epitaxial (re)growth	bonding/underetching
active-passive	established	difficult
etching	difficult	easy
integration density	medium	high
fibre coupling solutions	good, but regrowth	good
compact polarisation diversity	no	yes
simulation	2D	3D

Table 1.1: Comparison between substrate approach and membrane approach.

on two important issues in photonic integrated circuits: fibre coupling and polarisation. The question can now be raised which approach is preferred in the scope of this work.

In the substrate type InP/InGaAsP platform active-passive integration is well established. Also good fibre coupling schemes exist, but they are often based on regrowth and often polarisation dependent. For simulations, a 2D approximation is acceptable in many cases. Due to the medium refractive index contrast, however, the integration density is medium. In addition, due to the larger thickness of the epitaxial layers, relatively deep etching is required, which is difficult. Finally, no compact approaches for polarisation diversity have been demonstrated.

In the membrane approach the high vertical index contrast layer structure is obtained by local underetching or bonding. As the guiding layer is very thin, no deep etching is required in general. Due to the high refractive index contrast, the integration density is very high. Good fibre coupling solutions have been demonstrated (inverted taper, grating couplers), and polarisation diversity can be implemented in a compact way using 2D crossed gratings. Major drawback is the difficulty of contacting active devices due to absorption of light at the metal contacts. Furthermore, 3D simulations are often required for membrane structures.

In table 1.1 we summarise pros en cons of substrate type and membrane type layer structures.

InP membrane

Since integration density is seen as a crucial argument for future photonic integrated circuits, we have chosen to work in the membrane approach. As discussed above, SOI is attractive for the advanced CMOS fabrication processes and the integration with electronics, but has to combined with III-V material for active devices, posing more stringent

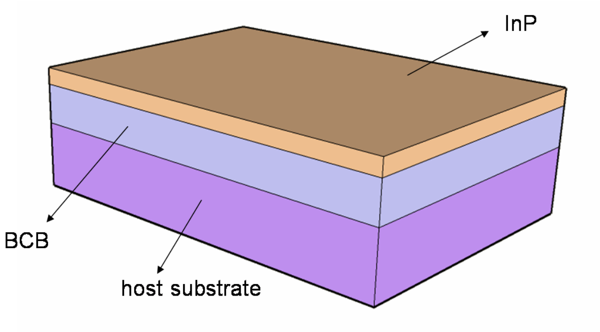

Figure 1.10: Basic InP membrane structure obtained through BCB bonding.

requirements for coupling between them. On the other hand, InP membranes are attractive for their capability of implementing both passive and active devices. The choice of the optimal layer structure depends on the application and associated chip functionality. For photonic integrated circuits requiring both active and passive devices, but where the profit from CMOS electronics processes is low compared to the complexity added by combining different materials, InP based membranes are an elegant option. This is especially the case for relatively simple circuits.

The main part of this work will therefore be dedicated to integrated circuits in the latter layer structure. The InP membrane is obtained through adhesive die-to-wafer bonding using BCB, a low refractive index spin-on polymer (n=1.54 at λ=1.54 μm). The basic layer structure is shown in Figure 1.10 and consists of a thin InP membrane layer on BCB carried on a host substrate. This results in a high refractive index contrast between guiding and cladding layers of 3.17:1.54 and 3.17:1.0, which can be used for implementing compact waveguides. The procedure for obtaining this layer structure will be described in Chapter 3.

1.8 Outline

As discussed above, the main part of this work will focus on fibre coupling and polarisation diversity for InP membrane type layer structures. For both problems surface grating couplers are used. Efficient photodetectors will be integrated on the InP membrane platform, as a first step towards other active devices.

In the next chapter we will design various grating couplers in bonded InP membrane and optimise them for efficiency and compactness. In Chapter 3 we will describe the fabrication and integration processes used in this work. Afterwards, we will characterise fabricated grating couplers in Chapter 4 and use them for coupling to integrated circuits including photodetectors in Chapter 5. In Chapter 6 we will use 2D crossed gratings for implementing polarisation diversity. In Chapter 7 we will describe the implementation of a coherent receiver chip on InP membrane, containing all concepts developed in this work.

Part of the work has been performed in collaboration with partners of several European research institutes. E-beam lithography was performed at the University of St. Andrews (United Kingdom) and the Technical University Eindhoven (The Netherlands), the latter institute also performed part of the etching. The design of a photonic crystal demultiplexer was performed at the Institut d'Optique, Palaiseau (France). This will be clearly mentioned in the text.

1.9 Conclusions

In this chapter, we have motivated our choice for implementing photonic integrated circuits in InP membrane. Key arguments in favour of this approach are the high achievable integration density, and the possibility to implement both active and passive functions in the same material. We have described two important issues in photonic integrated circuits, fibre coupling and polarisation, for which a solution by using grating couplers will be described in the next chapters.

Chapter 2

Grating coupler design and optimizations

In this chapter we will design compact and efficient 1D grating couplers. We first discuss the required theoretical concepts, after which we apply these for designing basic grating couplers in BCB bonded InP membrane. Then, optimisation of these membrane type grating couplers both in efficiency and compactness is assessed. For some of these optimisations we have chosen to work with the Silicon-on-Insulator (SOI) layer structure in order to proof the principle, since we have easier access to fabrication of SOI integrated circuits. Finally, we will design novel compact grating couplers for substrate type InP/InGaAsP waveguides.

2.1 Grating couplers

Gratings are structures having a periodic modulation of the refractive index. They have widespread applications in integrated optics, e.g. selecting a single wavelength peak in DFB lasers, design of optical filters, etc. The application we will use them for is coupling of light between an optical fibre and thin film waveguides, as shown in Figure 1.6. The first demonstrations of coupling light into thin film waveguides using gratings date back to 1970 [57, 58]. Since then, a lot of studies have been performed on the subject. An instructive analysis of grating couplers and simple design rules are given by Tamir in [59] and [60], which we will summarise in the next section.

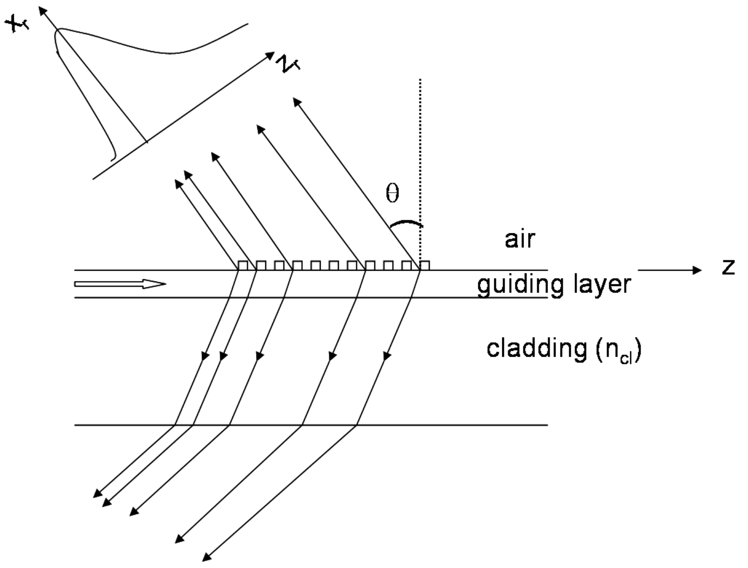

Figure 2.1: Output coupling from a thin film waveguide using grating couplers.

2.1.1 Operation principle

The grating couplers can be considered as surface wave to leaky wave converters. This is schematically shown in Figure 2.1 for an output coupler. The surface wave in the guiding layer is converted into outgoing beams in the top and bottom cladding. The surface wave, varying as $\exp[j(\beta_{sw}z - \omega t)]$, is scattered by the grating into space-harmonic fields varying as $\exp[j(k_{xm}z - \omega t)]$ with:

$$k_{xm} = \beta_n + j\alpha = \beta + m\frac{2\pi}{\Lambda} + j\alpha, \quad n = 0, \pm 1, \pm 2, \ldots \tag{2.1}$$

β is the propagation factor in the grating area and Λ is the grating period. For weak gratings $\beta \simeq \beta_{sw}$, which is not valid any more for the strong gratings used in this work. The factor α is due to the leakage of the energy into the diffracted orders by the grating. The real part of (2.1) is the well known Bragg condition, which gives the direction of the diffracted orders. For the diffraction orders into the air region we get:

$$\theta_n = \sin^{-1}(\beta_n/k_0), \quad n = 0, \pm 1, \pm 2, \ldots \tag{2.2}$$

with $k_0 = 2\pi/\lambda_0$. The angles θ_n need to be real and therefore radiation away from the grating only occurs if $|\beta_n/k_0| < 1$. And since $\beta > k_0$ this can only occur for $n < 0$.

The number of diffraction orders can be minimised by choosing a period Λ so that $|\beta_n/k_0| < 1$ for only a few values of $n < 0$. For a single diffraction order into the air region we require $|\beta_{-1}/k_0| < 1$ and $|\beta_{-2}/k_0| > 1$. However, there are also diffraction orders into the lower cladding region. If the more stringent condition $|\beta_{-2}/k_0| > n_{cl}$ is satisfied, only one diffraction order exists in this region.

Diffraction orders are forward or backward propagating if θ_{-1} is positive or negative, respectively. In the case of $\theta = 0$, corresponding to $\beta_{-1} = 0$ or $\beta_0 = 2\pi/\Lambda$, a large reflection occurs. For our application this so-called Bragg regime needs to be avoided, requiring that the magnitude of θ_{-1} is at least 3-4 degrees.

2.1.2 K-vector diagram

An instructive way of visualising the theoretical description from the previous paragraph is shown in the k-vector diagrams in Figure 2.2. The grating vector $K = 2\pi/\Lambda$ is subtracted from the propagation factor β in order to obtain the direction of the diffraction orders. A single diffraction order in air without diffraction into the lower cladding (and substrate) is impossible. The discrete k-vectors predicted by (2.1) only exist in infinite grating structures. For finite gratings, there exist a range of k-vectors around the one obtained by applying (2.1) determining the optical bandwidth of the grating coupler.

2.1.3 Beam profile

By using the appropriate grating parameters nearly all energy can leak out of the waveguide. However, the profile of the leaked beam plays an important role for determining the coupling efficiency. The profile of the beam is sketched in Figure 2.1 and is of the form [60]:

$$E = E_0 \exp(-jk_0 x_r - \alpha z_r \sec\theta)\ \mathrm{erfc}\left(\frac{\alpha W}{2} - \frac{x_r}{W}\right) \tag{2.3}$$

with $W^2 = -2jx/k_0 \cos\theta$. The exponentially decaying term describes the leaky wave and is the most important one. If we disregard the erfc term in (2.3), we can write for $z_r > 0$:

$$|\frac{E}{2E_0}| = \exp(-\alpha z_r \sec\theta) \tag{2.4}$$

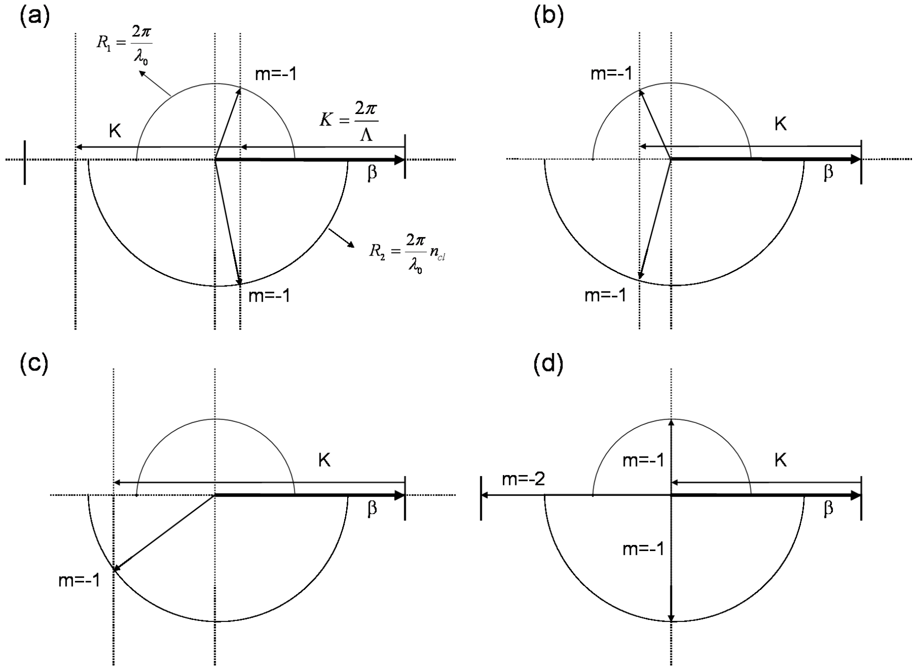

Figure 2.2: K-vector diagram for grating couplers with different grating periods. (a) Forward propagation. (b) Backward propagation. (c) Single diffraction order. (d) Bragg regime with second order reflection.

The beam profile is exponentially decaying with a beam width $w_b = \cos\theta/\alpha$. However, the mode of an optical fibre typically has a Gaussian profile. Because of the difference in profile between the beam coming from the grating and the fibre mode, a maximum coupling efficiency of 80.1% can be obtained if :

$$2\alpha w_0 \sec\theta = 1.36 \tag{2.5}$$

with $2w_0$ the width of the Gaussian beam between points at $1/e$ times the maximum amplitude. For a given Gaussian beam and a given angle of diffraction, (2.5) can be used for calculating the leakage factor α of the grating. This leakage factor is strongly dependent on grating parameters like etch depth, filling factor and layer structure.

The exponentially decaying beam profile occurs for a uniform grating structure having a constant α. By making the grating non-uniform, the leakage factor can be made z-dependent along the grating, and the beam profile can be shaped to a Gaussian profile [61]. As a result, the coupling efficiency can reach nearly 100%, provided that all the power is radiated into the required direction. The accurate fabrication of these non-uniform gratings is very difficult, however. The minimum required grating line width is very small (e.g. a few tens of nanometer) which is difficult for optical lithography techniques. In addition, different line widths have different etch rates, so very accurate control over the fabrication processes is required.

2.2 Simulation methods

2.2.1 Eigenmode expansion

In eigenmode expansion, the structure to be simulated is divided into sections having a refractive index profile that does not change in the propagation direction. For structures with a non-arbitrary index profile, this typically results in a coarse discretisation, as shown in Figure 2.3. In each section, the eigenmodes are calculated and the optical field is written as a sum of these eigenmodes. The total structure (a stack) is formed by putting together different sections. Afterwards a scattering matrix of this stack is calculated. Therefore, a mode matching technique is used at the interface between different sections and the field is propagated through the structure using the dependence of the eigenmodes in the propagation direction.

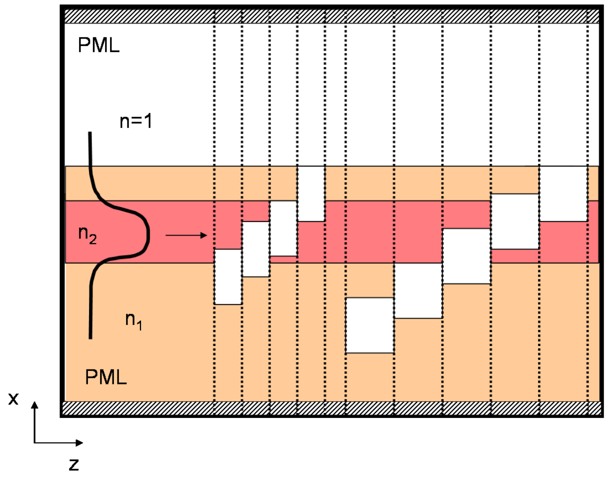

Figure 2.3: Eigenmode expansion method. The structure (2D cross-section) to be simulated is divided in sections for which the refractive index profile does not change in the propagation direction (z-direction).

CAMFR

CAMFR is a simulation tool based on eigenmode expansion developed at INTEC during the PhD of P. Bienstman [62]. It is mostly used for performing 2D simulations. The simulation is controlled by a *Python* script. After defining and exciting the structure the scattering matrix of the stack is calculated. The fields can be accessed at every position in the simulation domain. Calculations based on the scattered field components can be performed using the *Python* script. An important feature is the use of Perfectly Matched Layer (PML) boundary conditions. These artificial layers prevent unwanted reflections from the edge of the simulation domain by absorbing the incident light.

2.2.2 FDTD

In Finite Difference Time Domain (FDTD) simulations, the Maxwell equations are discretised both in space and in time. The derivatives in these equations are replaced by finite differences. The electromagnetic properties of the structure are updated at each time step. First the electric fields are calculated at a given instant of time and afterwards this information is used for calculating the magnetic fields at the next time step, etc. The fields and fluxes can be collected for any time step by placing sensors at the appropriate place. The structure is modelled

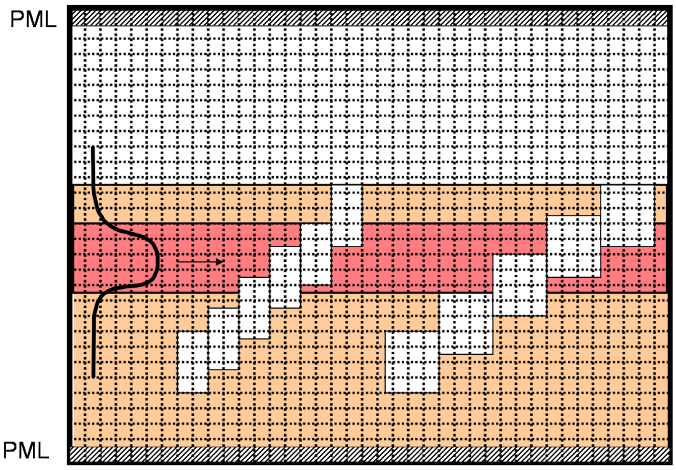

Figure 2.4: Finite Difference Time Domain (FDTD). A grid is put over the structure, each cell having a constant refractive index.

by placing a grid over the structure, each cell having a constant refractive index (Figure 2.4). A finer grid will result in more accurate results, but the time and memory required for the simulation will dramatically increase. Grid step and time step are connected by the Courant stability criterion, imposing a limit on both discretisation steps. In this work we have used commercial FDTD software (Omnisim from PhotonDesign [63]) on several structures. The programme is capable of performing 3D calculations, but for our application the required memory was too high.

2.3 Grating couplers in bonded InP membrane

2.3.1 Grating structure

Compact and efficient grating couplers in SOI have been developed in the PhD work of D. Taillaert [39]. Due to the high omnidirectional refractive index contrast, the light is diffracted over a short length, resulting in a relatively large optical bandwidth. The experimental coupling efficiency to single-mode fibre is 31%, although non-uniform grating designs exist with a theoretical coupling efficiency of more than 90%, but these are very difficult to fabricate.

Since the layer structure of SOI and InP membranes is very similar with regards to their vertical refractive index contrast (see Chapter 1),

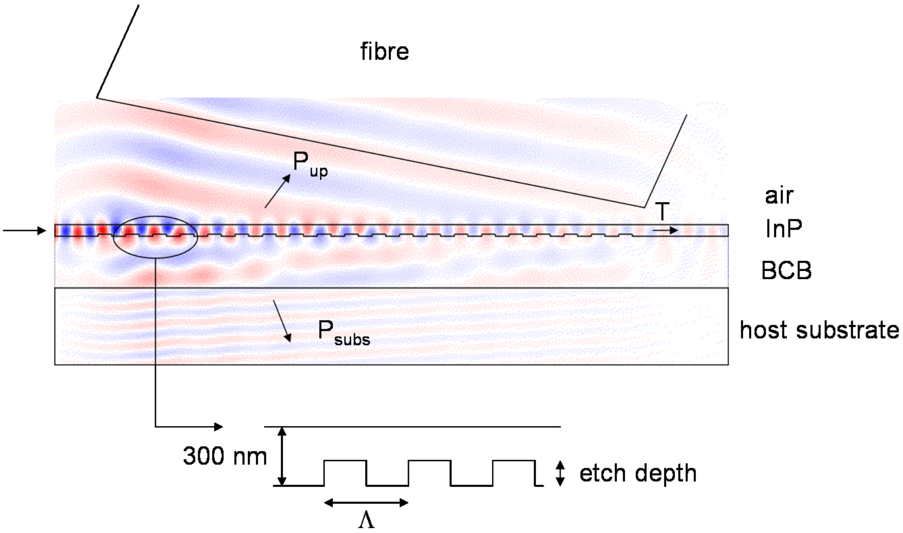

Figure 2.5: BCB bonded InP membrane grating coupler, and field profile obtained by simulation in CAMFR. The grating coupler is simulated as an output coupler, the fibre is not included in the simulation.

these gratings can also be designed for the latter layer structure. The basic grating structure is shown in Figure 2.5, together with a typical field distribution obtained by a CAMFR simulation. In our approach, the grating is at the bottom side of the waveguide. The reason is that we define the grating pattern before the bonding step needed to obtain the membrane. In that case we can use standard and well-developed fabrication processes for classical InP based layer structures and, additionally, double-sided processing becomes possible. We have used two InP membrane thicknesses in this work, 300 nm[1] and 200 nm. In both cases the slab waveguide formed by the InP membrane and the BCB and air claddings is single-mode. The light is coupled out under an angle in order to cut off the second order reflection. In the simulations below, we use an angle of 10° from vertical position.

---

[1] The choice for a 300 nm InP membrane is influenced by other devices in InP/InGaAsP waveguides developed in the framework of the IST-FUNFOX project. The optimal layer structure for these devices is a 522 nm InGaAsP waveguide layer, surrounded by a 300 nm top cladding and an InP substrate undercladding. This layer structure can also be used for obtaining the membrane. After bonding, InP substrate and InGaAsP etch-stop layer removal, the 300 nm top cladding becomes the InP membrane.

2.3.2 Determining the coupling efficiency from simulations

CAMFR simulation

The design of the grating coupler is carried out by simulating a 2D cross-section (Figure 2.5) of the grating. For 1D gratings this can be done since the width of the waveguide (10-12 μm) is much larger than the height and the wavelength. The method is extensively described in [39], we will only summarise the important aspects here.

The grating is described as an output coupler. However, the structure is reciprocal if coupling between modes is considered. The fundamental mode of the waveguide is excited and the electric and magnetic field distribution are calculated. Important design parameters are the power fluxes radiated upwards (P$_{up}$) and downwards into the substrate (P$_{subs}$), which determine the directionality D of the grating:

$$D = \frac{P_{up}}{P_{up} + P_{subs}} \tag{2.6}$$

D should be as high as possible, implying that as much power as possible is radiated into the upward direction. Reflection and transmission should be as low as possible. In the CAMFR simulation the fibre is not included. The coupling efficiency η to fibre is calculated by multiplying the ratio between P$_{up}$ and P$_{in}$ (the input power carried by the excited waveguide mode) by an overlap integral between the upwards radiated field profile (at a chosen distance above the grating, typically a few μm) and a Gaussian fibre mode with beam diameter $2w_0$=10.4 μm:

$$\eta = \gamma \times P_{up}/P_{in} \tag{2.7}$$

with

$$\gamma = \frac{|\int\int E \times H^*_{fibre}|^2}{Re \int\int E \times H^*. \int\int E_{fibre} \times H_{fibre}} \tag{2.8}$$

For a pure exponentially decaying field profile the overlap integral with a Gaussian beam is maximally 0.801, as described above. (2.7) gives the coupling efficiency of the simulated 2D problem, which is a good approximation of the 3D coupling problem. By multiplying this value by a correction factor (preferably close to 1.0), the lateral dimension of the waveguide can be accounted for. For a 12 μm wide SOI waveguide, this correction factor is 0.97 [39]. The coupling efficiency values quoted in the rest of this chapter are the efficiency values for the 2D simulation problem.

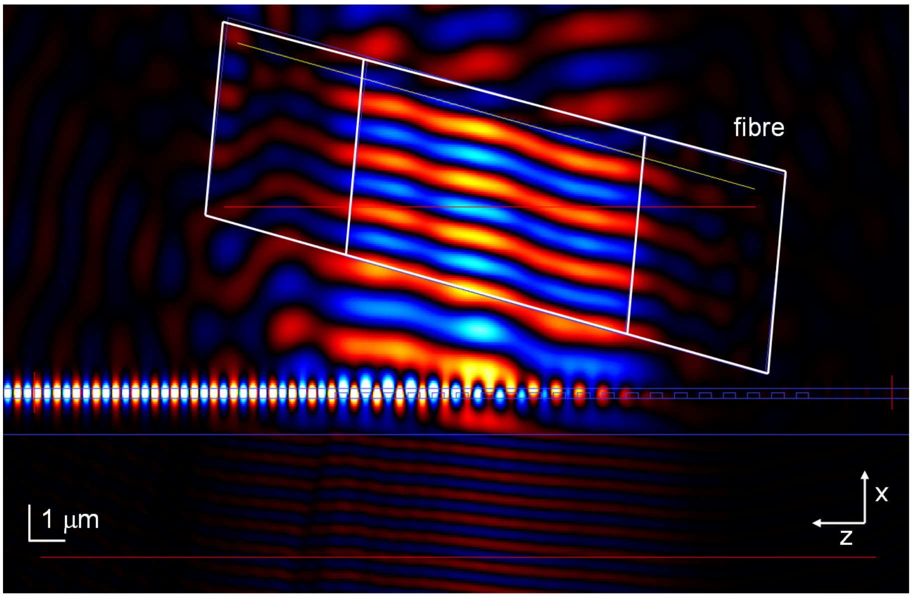

Figure 2.6: FDTD simulation of a 1D grating coupler, simulated as an input coupler.

FDTD simulation

The same overlap integral calculations can be used for obtaining the coupling efficiency when performing FDTD simulations. It is also possible to simulate the grating as an input coupler. The light from the input fibre is approximated by the fundamental mode of an appropriate slab waveguide. A mode sensor is used to calculate the amount of power that is coupled to the fundamental waveguide mode. An example of a grating coupler simulated by FDTD is shown in Figure 2.6.

2.3.3 Influence of grating parameters

Grating parameters that need to be determined are the period Λ, the filling factor, the etch depth and the number of periods. The etch depth is the most important parameter since it strongly influences the leakage factor α of the grating. If the grating is too shallow, the grating is too weak and little power is coupled upwards over a length corresponding with the width of the fibre mode. If the grating is too deep the coupling length is small and all power is radiated upwards by the first grating teeth, resulting in a low overlap with the Gaussian fibre mode. Furthermore the reflection will be high.

The optimal leakage factor α can be determined using (2.5). For a Gaussian fibre mode with $2w_0$=10.4 μm and a coupling angle of 10° from vertical, (2.5) results in an optimal α=0.13/μm. In Figure 2.7 we show the real part of the Poynting vector in the x-direction (upwards) at a distance of 1.5 μm above the grating, as a function of the distance z along the grating in the propagation direction, for various etch depths. The Poynting vector is exponentially decaying, the decay rate 2α depending on the etch depth. For the basic structure from Figure 2.5 with a 300 nm InP membrane layer the optimal etch depth is 90 nm, which indeed corresponds with the optimal leakage factor α=0.13/μm calculated above. The period Λ is chosen to determine the wavelength at which maximum coupling occurs. Light is coupled out at an angle in order to cut-off the second order reflection peak. The filling factor of the standard gratings is 0.5, which is the easiest to fabricate. The number of periods is determined by the grating strength. If all the light is radiated from the waveguide, additional periods are redundant and can be omitted. In practice, the grating length is of the order of the width of the fibre mode.

2.3.4 Influence of layer structure

BCB thickness

The thickness of the BCB layer between InP membrane and host substrate has a strong influence on the directionality of the grating. Since the interface between BCB and host substrate (Figure 2.5) is partly reflecting, some downwards radiated light will be reflected and can still contribute to the coupling to fibre. Therefore, the thickness of the BCB buffer layer has to be optimised in order to obtain constructive interference between directly upwards radiated light and reflected light at the BCB/substrate interface. The reflected wave also interacts with the grating and as a result, the coupling strength of the grating is influenced by the BCB thickness [64, 65].

In Figure 2.8, the transmission T, the total upwards radiated power (P_{up}), the total downwards radiated power (P_{subs}), and the coupling efficiency are shown as a function of BCB buffer thickness for the peak wavelength of the grating coupler spectrum. In the simulation, we have taken a GaAs host substrate with refractive index n=3.37. The optimal BCB thickness is 1.23 μm and the maximum coupling efficiency is

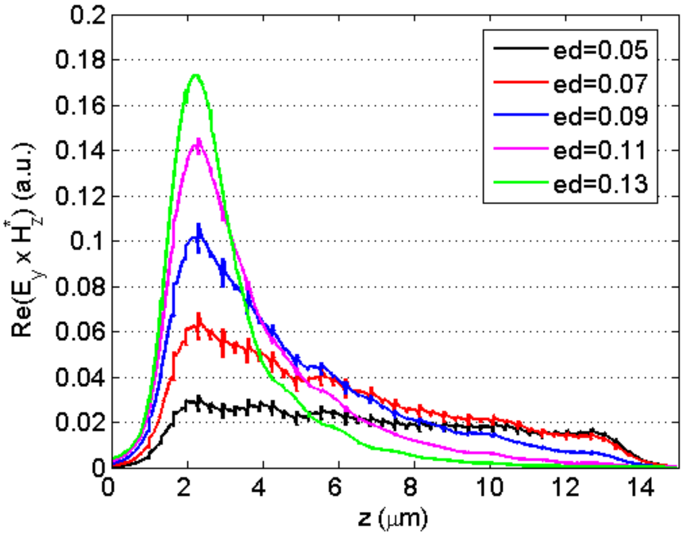

Figure 2.7: Calculated influence of the grating etch depth. The Poynting vector in upwards direction at 1.5 μm above the grating is shown as a function of distance in the propagation direction, for different etch depths.

42%. A shift in BCB buffer thickness of $\lambda/4n_{BCB}$ (i.e. around 250 nm) shifts the coupling efficiency from maximum to minimum. For BCB thicknesses where the coupling efficiency is minimal there is substantial transmission, indicating that the coupling strength of the grating is low. Furthermore, the radiation into the substrate is maximal for that BCB thickness.

Additional top layer

From Figure 2.8 we can conclude that the directionality of the most basic InP membrane grating structure is not very advantageous. For the optimal BCB thickness, the directionality D=50.5%. This can be improved by further modifying the layer structure. A possible approach is adding a dielectric layer on top the InP membrane grating. Since the grating is at the bottom side this layer can be deposited on a planar surface. We have chosen Al_2O_3 as the top layer since the layer quality was the best at the time of fabrication. The theoretical refractive index of Al_2O_3 is 1.58 at λ=1.55 μm. However, the refractive index of e-gun deposited Al_2O_3 at INTEC was 1.47 at the time samples were fabricated and we will do the calculations with this value.

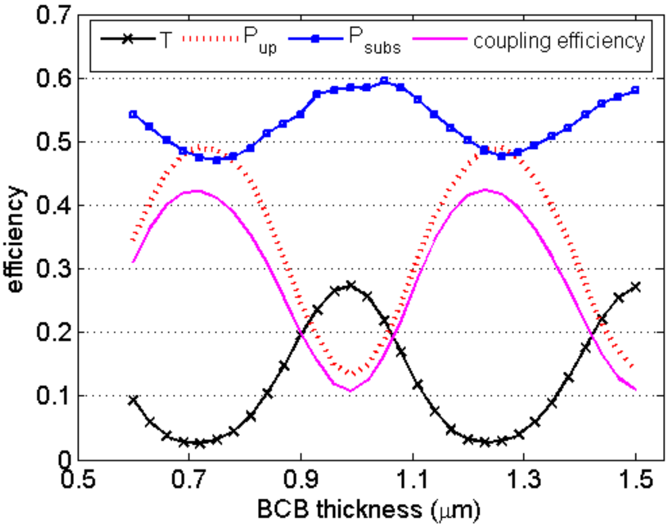

Figure 2.8: Calculated influence of BCB buffer thickness on scattered power. Simulation parameters: InP membrane of 300 nm, λ=1.595 μm, Λ=660 nm, 20 periods, ed=90 nm, ff=0.5.

The additional layer lowers the vertical refractive index contrast, and thus the coupling strength of the grating. The optimal etch depth is now 130 nm, which is substantially higher than the 90 nm obtained for the standard structure. The additional Al_2O_3 top layer can be seen as an anti-reflection coating, preventing reflection at the top InP-air interface. Its optimal thickness is 270 nm. In Figure 2.9, the transmission T, the total upwards radiated power (P_{up}), the total downwards radiated power (P_{subs}), and the coupling efficiency are shown as a function of BCB buffer thickness, for the optimal value of the Al_2O_3 top layer thickness. The optimal BCB thickness is 1.17 μm and the maximum coupling efficiency is 53%. The directionality has increased to D=64.6%. The field profile of this grating coupler is shown in Figure 2.10.

Membrane thickness

We have investigated whether the coupling efficiency can improve by choosing another membrane thickness. We have repeated the optimisation for an InP membrane thickness of 200 nm. The optimal etch depth is now 110 nm. In Figure 2.11, the transmission T, the total upwards radiated power (P_{up}), the total downwards radiated power (P_{subs}), and

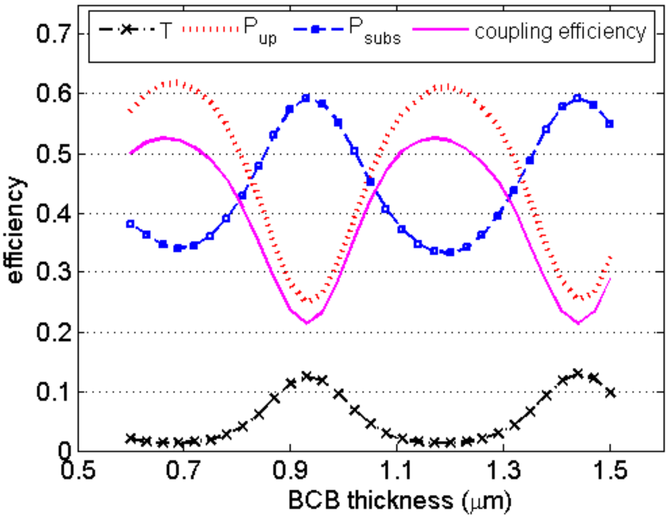

Figure 2.9: Calculated influence of the BCB buffer thickness on scattered power by a grating coupler with extra 270 nm Al_2O_3 top layer. Simulation parameters: InP membrane of 300 nm, λ=1.56 μm, Λ=660 nm, 20 periods, ed=130 nm, ff=0.5.

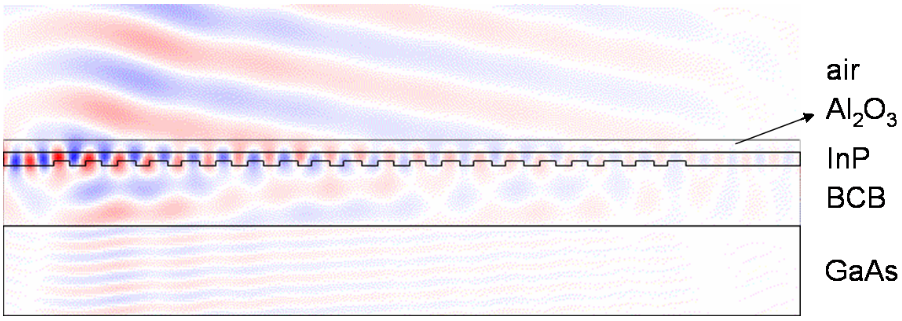

Figure 2.10: Field profile of a grating coupler with additional top layer.

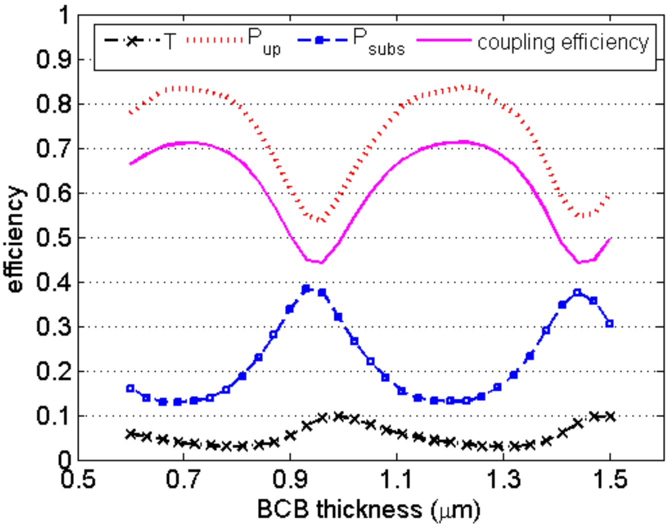

Figure 2.11: Influence of the BCB buffer thickness on scattered power when using a 200 nm InP membrane. Simulation parameters: λ=1.54 μm, Λ=770 nm, 20 periods, ed=110 nm, ff=0.5.

the coupling efficiency are shown as a function of BCB buffer thickness. The optimal BCB thickness is 1.2 μm and the maximum coupling efficiency is 71%. The directionality D=86.3% in this case. The reason for this increased directionality is attributed to optimized interferences due to the waveguide layer thickness, since the directionality is still dependent on the BCB bonding layer thickness (Figure 2.11). In [66], the directionality of SOI grating couplers is increased by adding a polysilicon overlay layer to the structure. In that case, the high directionality is an intrinsic property of the Bloch mode of the periodic structure, and independent of the buried oxide layer thickness.

The wavelength dependence of the three types of grating coupler calculated with their optimal parameters is shown in Figure 2.12. The 1 dB optical bandwidth is 45 nm.

2.4 Optimised grating designs

2.4.1 Grating couplers with bottom gold mirror

The directionality D of the grating can even be increased to nearly 100% if we modify the original interface between BCB buffer layer and host

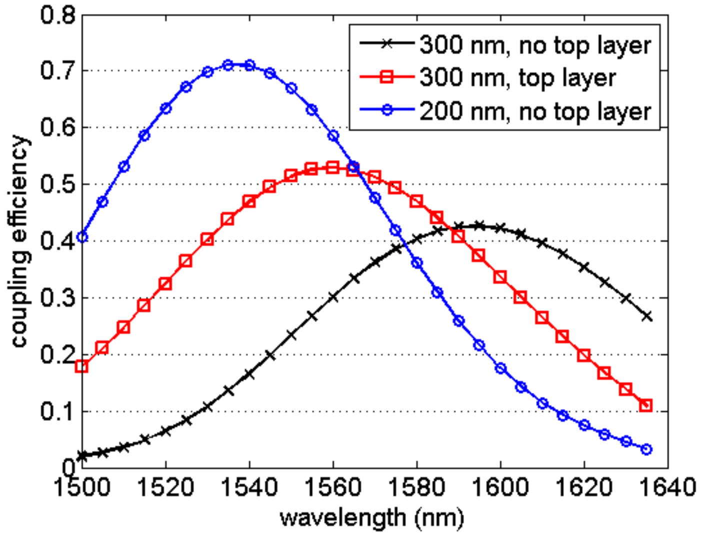

Figure 2.12: Calculated wavelength dependence of grating couplers with 300 nm InP membrane (without and with top layer) and 200 nm InP membrane (without top layer), each time for the optimal parameters (BCB thickness, etch depth, etc) determined above.

substrate into a perfect reflector. From a fabrication point of view, a metal reflector is an obvious choice and this will be elaborated in the next sections.

InP membrane grating with BCB buffer layer and gold mirror

A clear advantage of BCB is its planarising property since the buffer layer is applied on a non-planar surface. We consider two strategies for obtaining a bottom mirror with a BCB buffer layer. The grating structure can be bonded onto a gold coated host substrate in which case the BCB bonding layer also serves as the buffer layer (Figure 2.13a). Another possibility is using 2 BCB layers (Figure 2.13b). In that case, a first BCB buffer layer is applied over the grating before defining the gold mirror. Then, this structure is bonded onto a host substrate with another BCB layer. The advantage of the latter approach is that the thickness of the BCB buffer layer can be better controlled, while the BCB bonding layer thickness is unimportant. Figure 2.14 shows the transmission, the total upwards radiated power (P_{up}), the total downwards radiated power (P_{subs}), and the coupling efficiency as a function

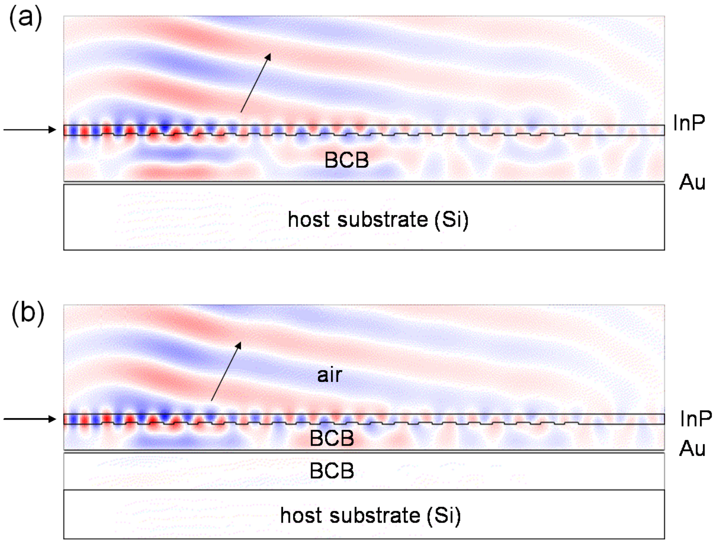

Figure 2.13: Field profile of InP membrane grating couplers with a gold bottom mirror. (a) Using a single BCB layer (1.23 μm). (b) Using 2 BCB layers, the first BCB layer (0.7 μm) serving as the buffer layer, the second as the bonding layer.

of BCB buffer thickness between grating and gold mirror. For the optimal BCB thickness (0.7 μm or 1.23 μm), nearly all power is radiated upwards, and the coupling efficiency reaches 78%. However, for the worst BCB thickness, the coupling strength of the grating and thus the coupling efficiency can reach zero.

InP membrane grating with SiO_2 buffer layer and gold mirror

The BCB layers used in the previous paragraph are spin-coated onto the sample. The layer thickness depends on spinning parameters (speed, temperature, etc) but also on sample parameters (size of the sample, pattern density on the sample, etc), which makes it more difficult to control. Therefore, we have also considered a deposited dielectric buffer layer, rather than a spin-coated one. This is done in closed chambers (e.g. e-gun, PECVD), where the process conditions can be kept identical over a long period. We have used SiO_2 as the deposited buffer layer, having a refractive index of 1.41 at λ=1.55 μm for processes used at INTEC. Drawback is the fact that the planarisation is not as good as for BCB. After buffer layer deposition, a gold layer is applied over the gra-

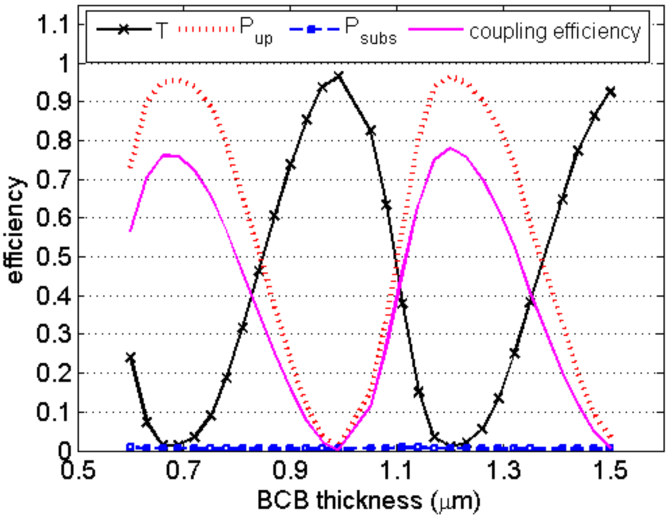

Figure 2.14: Influence of the BCB buffer thickness on scattered power for an InP membrane grating coupler with gold bottom mirror. Simulation parameters: λ=1.61 μm, Λ=660 nm, 20 periods, ed=70 nm, ff=0.5.

tings, and the structure is bonded with BCB onto a host substrate. The optimal grating structure is shown in Figure 2.15. We have calculated a structure where there is no planarisation at all (worst-case scenario). The gold mirror is another grating with the same period as the InP grating (i.e. Λ=640 nm) but only the 0^{th} order reflection can exist in the SiO_2 layer. The optimal SiO_2 thickness is 0.72 μm or 1.29 μm, and the maximum coupling efficiency is 78%, indicating that the bottom gold grating does not have a negative effect on performance.

Silicon-on-Insulator grating with bottom mirror

The same principles can be applied for obtaining high efficiency Silicon-on-Insulator grating couplers. The disadvantage here is that the bonding step is only required to add the bottom mirror, whereas for InP it is crucial in order to obtain the high vertical index contrast. Furthermore, the fabrication process might not be CMOS-compatible. During this PhD work, other possibilities have been explored at INTEC to improve the directionality of Silicon-on-Insulator grating couplers. By adding locally a poly-Silicon overlay on top of the waveguide prior to grating etching, a calculated coupling efficiency of 78% has been obtained [66].

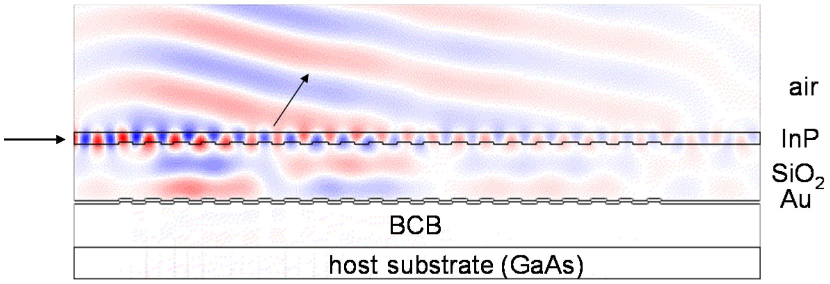

Figure 2.15: Field profile of an InP membrane grating coupler with a SiO_2 buffer layer and gold bottom mirror.

However, we will describe the SOI grating version with bottom mirror in short, and fabricate it as a proof of principle. Here, the approach with two BCB layers is used.

We start from an existing SOI grating coupler with following parameters: Si-core layer of 220 nm, SiO_2 buried oxide layer of 1 μm, period=610 nm, etch depth=50 nm, filling factor= 50%, 20 periods (Figure 2.16 top). The optimal BCB buffer layer is 840 nm and the theoretical coupling efficiency of this structure is 72%. The reason for this slightly lower coupling efficiency is the fact that the original SOI grating is too shallow to be optimal for the modified version with bottom mirror. The optimal structure would have a period of 630 nm, an etch depth of 90 nm, a filling factor of 50%, and a BCB buffer layer of 780 nm, which results in a theoretical coupling efficiency of 78%.

2.4.2 Focusing grating couplers in SOI

This optimisation does not concern the coupling efficiency of the gratings, but the miniaturisation of the whole coupling structure and thus the integration density. Standard linear gratings are defined in a broad (12 μm) multimode waveguide, which is then adiabatically tapered down to a 500 nm wide single-mode photonic wire. This taper is typically longer than 150 μm and mainly determines the length of the coupling structure. It is possible to reduce the length of the taper [67], but the fabrication of these structures is very demanding. However, by curving the grating lines the light can be focused onto the single-mode wire, and the taper can be omitted, as shown in Figure 2.17. We will elaborate on focusing grating couplers for SOI layer structures, since

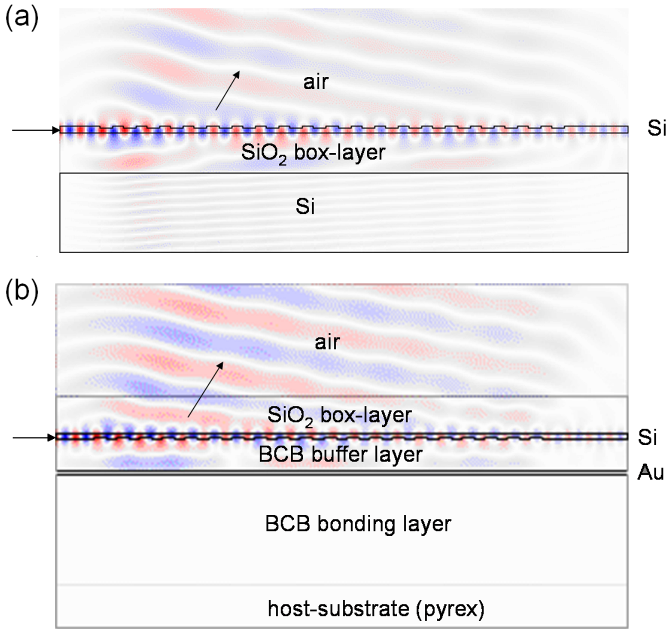

Figure 2.16: (a) Field profile of the basic SOI grating coupler without bottom mirror. (b) Field profile of the SOI grating extended with a gold bottom mirror.

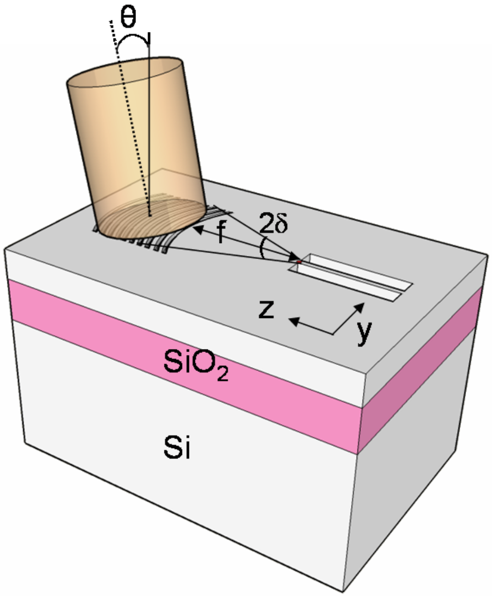

Figure 2.17: Curved focusing grating coupler.

we have easier access to fabrication of the structures. However, the principles can be easily transferred to InP membrane.

Design rules

In the case of a focusing grating coupler efficient coupling is wanted between the TE-mode of a near vertical fibre, with a plain wavefront, and the TE-mode of a broad SOI waveguide, so that the wavefront is curved cylindrically and focusing occurs towards the center of curvature of the wavefront. Rigorous design requires 3D simulations on the entire structure, which was not possible with the available computational resources. Therefore, we have followed an approximative approach based on simple phase equations to implement the focusing property of the gratings.

The top surface of the waveguide is chosen to be the (y,z)-plane of a right handed Cartesian coordinate system, with z along the waveguide axis and the origin chosen to be in the desired focal point. It is shown in [61] that a focusing grating can be obtained by curving the grating lines using following equation:

$$q\lambda_0 = n_{eff}\sqrt{y^2+z^2} - zn_t\sin\theta \tag{2.9}$$

Here, q is an integer number for each grating line, θ is the angle between the fibre and the chip surface normal, n_t is the refractive index of the environment, λ_0 is the vacuum wavelength and n_{eff} is the effective index felt by the cylindrical wave in the grating area. The right part of (2.9) is determined by the phase difference between the focusing wave toward the photonic wire and the input wave from the fibre. (2.9) is valid if the effective index in the grating area is equal to the effective index in the (slab) waveguide region. This is not the case for SOI gratings, but we will still use this equation as a first order approximation. In [61], an improved constructive interference condition is determined. However, the equation is of the sixth order in y and z and gives not much physical insight.

By taking the square of (2.9):

$$z^2(n_{eff}^2 - n_t^2\sin^2\theta) + y^2n_{eff}^2 = q^2\lambda_0^2 + 2q\lambda_0 n_t z\sin\theta \tag{2.10}$$

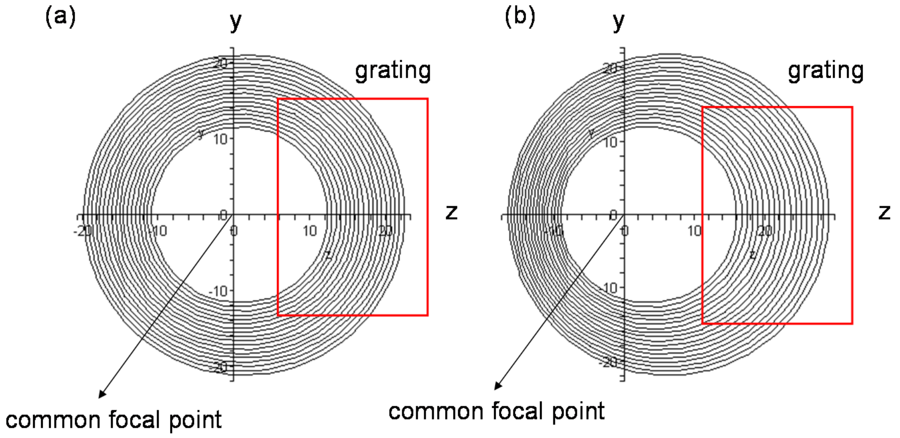

Figure 2.18: Elliptical grating lines calculated using (2.11). (a) θ=10°. (b) θ=50°.

and after some algebra, we obtain following equation for the grating lines:

$$\frac{\left(z-\frac{q\lambda_0 n_t \sin\theta}{n_{eff}^2-n_t^2\sin^2\theta}\right)^2}{\left(\frac{q\lambda_0 n_{eff}}{n_{eff}^2-n_t^2\sin^2\theta}\right)^2}+\frac{y^2}{\left[\frac{q\lambda_0}{(n_{eff}^2-n_t^2\sin^2\theta)^{1/2}}\right]^2}=1 \tag{2.11}$$

For vertical coupling (θ=0°), the grating lines are concentric circles with the common center (the origin) as the focal point. For coupling at an angle the grating lines are ellipses. In Figure 2.18, elliptical grating lines calculated using (2.11) are shown for two fibre angles. For small angles from vertical position (e.g. θ=10°) the difference with circular grating lines is hardly visible.

An ellipse given by the basic equation $\frac{(z-z_0)^2}{a^2}+\frac{y^2}{b^2}$=1 has its focal points at coordinates $(z,y)=(z_0\pm\sqrt{a^2-b^2},0)$, where a and b are half the long and short axis respectively. If we apply this on (2.11), the focal points are at:

$$f_1(z,y)=(0,0) \tag{2.12}$$

$$f_2(z,y)=(\frac{2q\lambda_0 n_t\sin\theta}{n_{eff}^2-n_t^2\sin^2\theta},0) \tag{2.13}$$

Thus for angled coupling, the grating lines are confocal ellipses with the common focal point at the origin, the common focal point being located the furthest away from the grating.

If we consider the case $y = 0$ in (2.11), which gives the intersection points of the ellipses with the positive and negative z-axis, we obtain:

$$z = \frac{q\lambda_0(\pm n_{eff} + n_t \sin\theta)}{n_{eff}^2 - n_t^2 \sin^2\theta} \tag{2.14}$$

The positive solutions for z are:

$$z = \frac{q\lambda_0}{n_{eff} - n_t \sin\theta} \tag{2.15}$$

Subsequent intersection points with the positive z-axis are spaced by:

$$\Lambda = \frac{\lambda_0}{n_{eff} - n_t \sin\theta} \tag{2.16}$$

This can be rewritten as:

$$\frac{2\pi}{\lambda_0} n_t \sin\theta = \frac{2\pi}{\lambda_0} n_{eff} - \frac{2\pi}{\Lambda} \tag{2.17}$$

which is the Bragg condition for a linear 1D grating coupler (see section 2.1).

Practical design

We will consider two practical configurations for the focusing grating coupler structure, for which more details will be given in Chapter 4. In the first configuration, the light is focused onto a single-mode photonic wire, but the focusing occurs in a short taper (Figure 2.19a). If a taper having this length would be used in combination with a standard non-focusing grating, it would be non-adiabatic. In the second configuration, the light is focused in the slab onto a low lateral refractive index contrast aperture (Figure 2.19b). The focal distance is the distance from the photonic wire or aperture to the first grating line.

Some of the parameters required for applying (2.11) are extrapolated from the standard linear grating design. The effective index n_{eff}=2.63 is approximated by the effective index obtained from the Bragg condition for a standard linear grating with period Λ=630 nm. The grating consists of 25 lines and the q-values used for the grating are determined by (2.9) using the opening angle, which depends on the used configuration. The expanded beam coming from the wire or aperture should

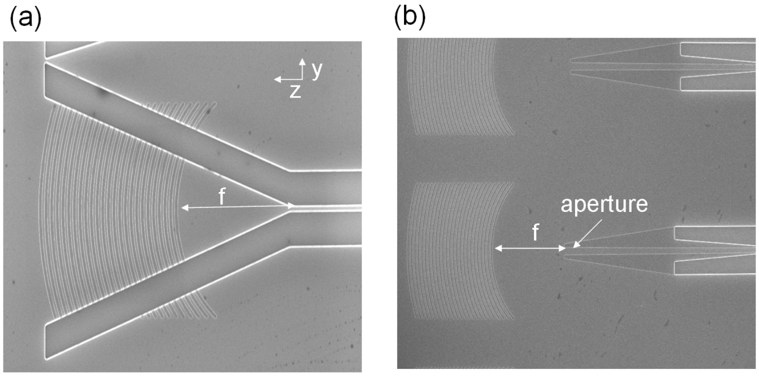

Figure 2.19: Focusing grating couplers in two configurations. (a) Short taper. (b) Low contrast aperture.

match the fibre mode in the middle of the grating. In short taper configuration the opening angle is the angle of the taper. In the case of a low contrast aperture the opening angle is given by [68]:

$$\begin{aligned}2\delta &= \frac{1}{\sqrt{2}}(-0.013113753W^6 + 0.192881257W^5 - 1.145133867W^4 \\ &\quad +3.490394736W^3 - 5.663588689W^2 + 4.287082758W \\ &\quad -0.193518937)\end{aligned}$$

with W the width of the aperture. This angle is used to calculate the length L where the beam has a width equal to the width of the fibre mode. (2.9) is then used with (z,y)=(L,0) to calculate the corresponding q-value, which is the number of the middle grating line. For a low contrast aperture of 0.8 μm width, this value q_{middle}=32. The grating is then built by using (2.11) with q-values ranging from q=20 until q=44. Other grating parameters are kept identical to the standard linear grating, i.e. etch depth=70 nm, grating line width=365 nm.

2.5 Substrate type InP/InGaAsP grating couplers

As explained in Chapter 1, substrate type InP/InGaAsP layer structures are attractive for monolithic integration with active components. Fibre coupling schemes are often based on adiabatic tapers and edge-coupling. However, grating couplers using vertical coupling offer distinct advantages, wafer-scale testing being the most important. Therefore, it would be interesting to have also a grating coupler solution for InP/InGaAsP waveguides. Another application, besides fibre coupling, is the combination of grating couplers with a vertical emitting active device like a VCSEL.

However, due to the modest index contrast of InP/InGaAsP layer structures it is not possible to transfer existing designs for strong and compact rectangular grating couplers in Silicon-on-Insulator or InP membrane to InP/InGaAsP layer structures. Etching a shallow grating in the top cladding results in weak interaction of the light in the waveguide with the grating. Deeper etching into the waveguide core causes strong reflections. A possible solution is imposing a preferential direction, by using slanted gratings instead of vertically etched gratings.

Slanted couplers have already been described in literature. Very high theoretical coupling efficiencies were reported for compact slanted grating couplers, both for low vertical index contrast polymeric waveguides (80.1%) [69] and high vertical index contrast SOI waveguides (75.8%) [38], but no experimental results have been reported. Surface emitting lasers in InGaAs-AlGaAs with blazed grating outcouplers have been demonstrated in [70]. The surface emission efficiency of the lasers using blazed grating outcouplers, was measured to be over 80%. However, the gratings were 320 μm long.

In the following sections, we will design compact and efficient slanted grating couplers for InP/InGaAsP waveguides.

2.5.1 Proposed structure

The grating we aim for is shown in Figure 2.20. By etching air slots at an angle of 45°, the vertical (outcoupling) direction is favored. Etching through the core is required to capture all of the light in the guided mode. The incident light reflects upwards at the interface with the air slot. If the slots are narrow enough, part of the light can tunnel through the slot (frustrated total internal reflection) and reach a second slot, where again it gets partly reflected and partly transmitted. In this way, the waveguide mode is coupled out vertically in a distributed way as required in order to match the mode of a fibre positioned vertically above the grating.

2.5.2 Design

The most important parameter in the design is the width of the air slots. When the slots are too wide there will be little transmission and almost all the light will be coupled out by the first slot, resulting in a poor

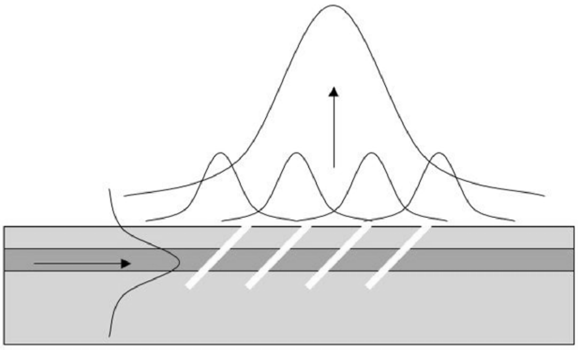

Figure 2.20: Principle of the slanted grating coupler.

overlap with the fibre mode. When the slots are too narrow, most of the light will tunnel through the slot, and little light will be reflected upwards. 2D simulation results for a single slot etched at 45 degrees completely through the core are shown in Figure 2.21.

The transmitted and upwards radiated power is calculated as a function of slot width, for slots etched at 45°completely through the waveguide core. The waveguide has a 522 nm thick InGaAsP (Q1.22) core layer and a 300 nm InP top cladding, on an InP substrate. A top AR-coating (Anti-Reflection coating, a quarter wave layer with n=$\sqrt{n_{InP}}$) is applied in order to avoid radiation back into the waveguide. The wavelength is 1550 nm and the polarisation is TE (electric field parallel to the slots). A very good agreement is obtained between eigenmode expansion calculations (CAMFR) and FDTD simulations. The upwards radiated power and transmitted power do not add up to 100%, because part of the power is scattered and radiated towards the substrate.

We have also calculated the radiation properties for TM-polarisation (magnetic field parallel to the slots). For narrow slots substantially more light is radiated upwards than in the TE-case, so it is difficult to couple light out in a distributed way for achieving high coupling efficiency. These results indicate that the slanted coupler is not polarisation insensitive. Based on Figure 2.21 we have made two designs for TE-polarisation.

First diffraction order coupled to fibre

In a first design, the first diffraction order is coupled into a vertically positioned fibre. This implies that the period is small and the number

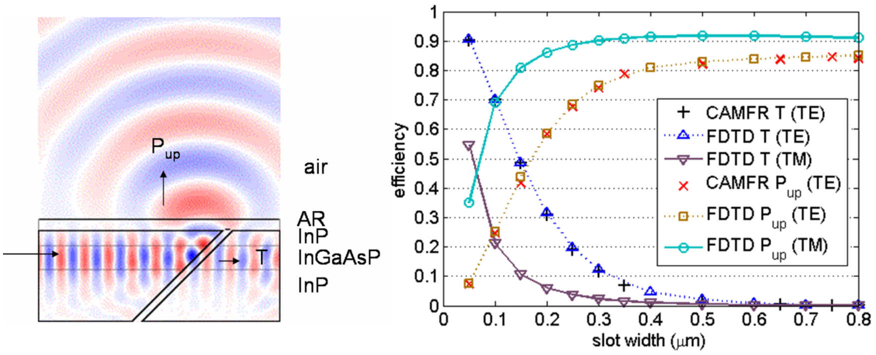

Figure 2.21: Radiation properties of a single slot etched at angle of 45° completely through the waveguide core. The field profile shown left is for TE-polarisation.

of periods is relatively large in order to match the dimensions of the fibre mode. Therefore, the slots have to be very narrow in order to allow enough transmission through them. We have chosen 50 nm slots as a lower bound. The etch depth is 1 μm (vertically), a realistic value from a fabrication point of view. However, deeper etching is preferred to avoid coupling towards the substrate. The final structure has 20 periods and the period is 0.49 μm. The maximum coupling efficiency to a vertically positioned fibre is 43% and 59% with and without AR-coating respectively. For the structure with AR-coating there is no reflection back into the waveguide. Without AR-coating, this reflection is 13%. The field distribution calculated with CAMFR is shown in Figure 2.22a.

Third diffraction order coupled to fibre

In the second design, the third diffraction order is coupled into the fibre. The period of the grating is then larger, and less periods are required to match the fibre mode. We use 4 slots of 150 nm width, etched to a depth of 1.3 μm (vertically). To couple all the remaining light upwards, the last slot is 700 nm wide. The period is 1.51 μm and has been optimised to obtain a phase front propagating in the vertical direction. The field distribution calculated with CAMFR is shown in Figure 2.22b. The maximum coupling efficiency to a single-mode fibre is 34% without AR-coating and 48% with AR-coating. For this structure, the reflection is 4% and 26% with and without AR-coating.

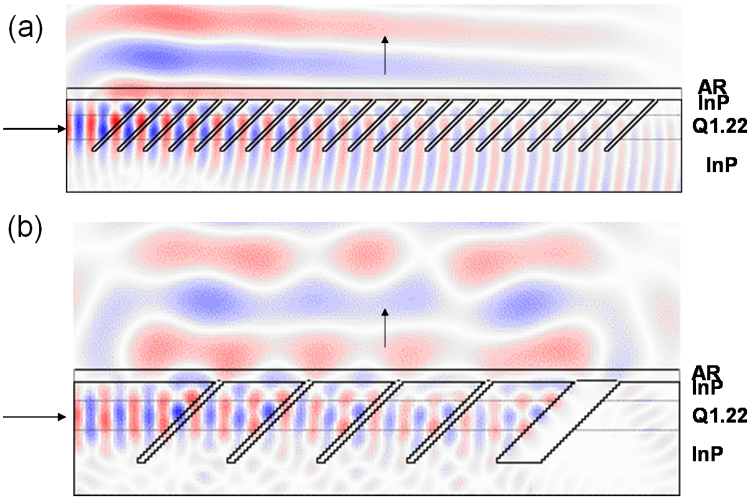

Figure 2.22: Field profile of slanted grating couplers. (a) First diffraction order is coupled into the fibre. (b) Third diffraction order is coupled into the fibre.

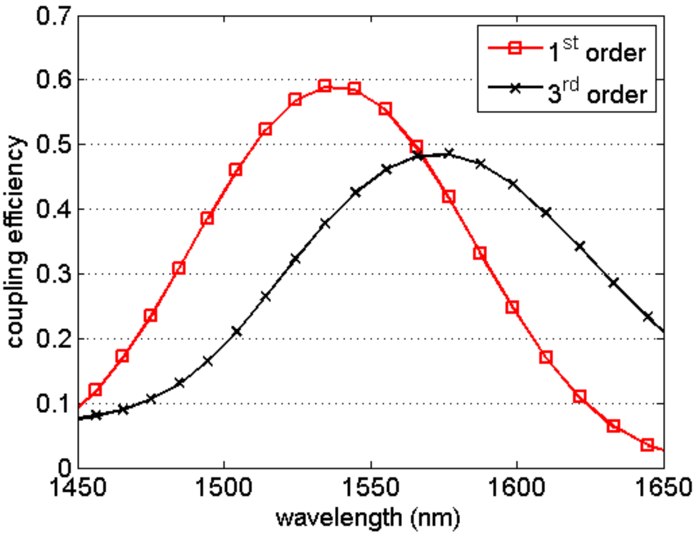

Figure 2.23: Wavelength dependence of slanted gratings calculated by FDTD simulations.

The wavelength dependence of both slanted gratings calculated by FDTD is shown in Figure 2.23. The 1^{st} order grating has a 1 dB bandwidth of 60 nm, while the 3^{rd} order grating has a 1 dB bandwidth of 75 nm.

2.6 Conclusions

In this chapter, we have described and designed different types of 1D grating couplers. For membrane type structures, we have transferred designs for Silicon-on-Insulator to a BCB bonded InP membrane. The influence of grating parameters and layer structures are discussed, resulting in 3 different basic designs which will be characterised in Chapter 4. Using a 200 nm InP membrane the grating coupler efficiency can be as high as 71% for a standard design.

Additionally, we have optimised these high-index contrast structures further, both in efficiency and compactness. Uniform grating couplers with a gold bottom mirror can achieve a coupling efficiency of 78%. Using focusing grating couplers, adiabatic transitions from wide waveguides to single-mode photonic wires can be omitted, resulting in a length reduction by a factor of 8 of the coupling structure.

For substrate type InP/InGaAsP waveguide structures with modest vertical index contrast, we have proposed slanted grating couplers, the best design achieving a theoretical coupling efficiency of 59%.

Chapter 3

Fabrication

In this chapter we will give an overview of the fabrication processes used in this work. First, the processes for pattern definition are described in a general way. Then, specific fabrication processes related to the different material systems used in this work are addressed.

3.1 Pattern definition

In order to achieve the required functionality on the chip, the appropriate pattern has to be defined. This is done in subsequent basic steps, which are shown in Figure 3.1 and will be described in the next sections. The first step is lithography, where the pattern is defined in a resist layer. We have used optical lithography and e-beam lithography. Other types are nano-imprint lithography or focused ion beam lithography, which is a variation on e-beam lithography.

After lithography, the pattern has to be etched into the semiconductor material. In a lot of cases an intermediate hard mask (e.g. SiO_2 or metal) is used. In that case, the pattern is first transferred into the hard mask layer using the resist pattern as a mask. Afterwards, the pattern is etched into the semiconductor.

3.1.1 Lithography

Optical lithography

In optical lithography, a geometric pattern from a photomask is transferred to a light-sensitive photoresist . The photomask is a quartz plate

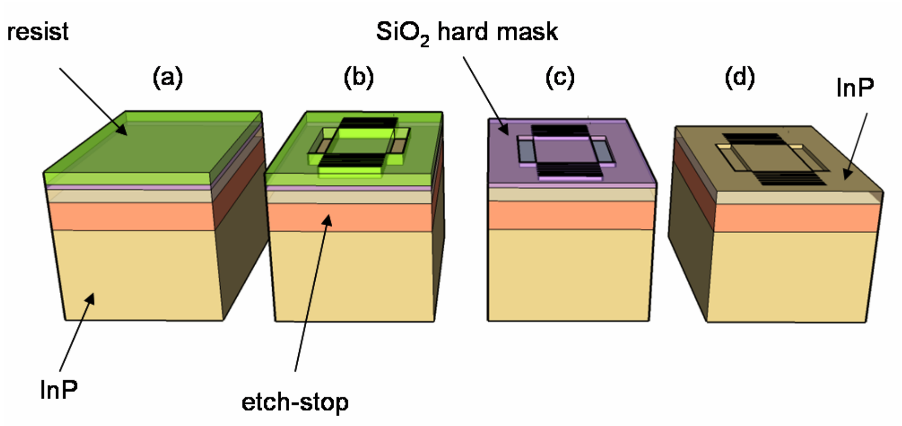

Figure 3.1: Pattern definition into semiconductor material. (a) Deposition of hard mask and resist. (b) After lithography and development. (c) Pattern transfer into hard mask and resist removal. (d) Pattern etch into semiconductor material and hard mask removal.

with features (e.g. in chrome) that block the light from an illumination lamp. The light reaches the substrate with the resist on specific places and changes the properties of the resist. During development in a chemical, the exposed (or unexposed) parts of the resist are selectively removed.

The simplest type of lithography is contact lithography. The photomask is brought into contact with the substrate and exposed to ultraviolet (UV) light. A more advanced type of optical lithography is projection lithography. Here, projection systems project the mask onto the wafer without making contact. Typically, the wafer is patterned die after die. This type of lithography is used today for high volume production.

For illumination, light from a gas discharge lamp is filtered to select a single spectral line in the UV range (e.g. INTEC uses light at λ= 320 nm). Nowadays, the trend is to use shorter wavelength light produced by excimer lasers (e.g Krypton Fluoride laser at λ= 248 nm or Argon Fluoride laser at λ=193 nm). This reduction of the illumination wavelength is important to increase the resolution of the projection. A typical resolution of 50-100 nm can be achieved with projection lithography. By using immersion techniques, this resolution can even be improved further.

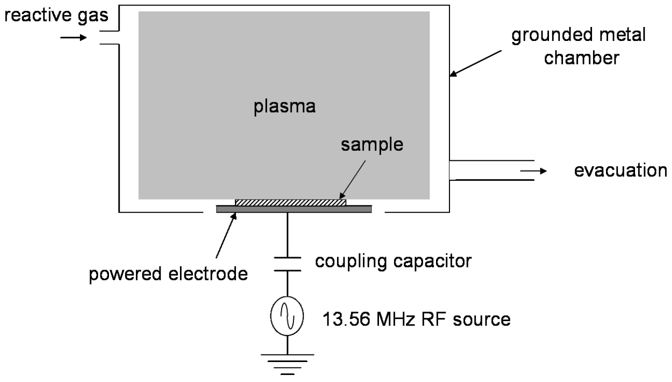

Figure 3.2: Reactive Ion Etching (RIE) (from [71]).

E-beam lithography

E-beam lithography uses an electron beam in combination with an electron sensitive resist (e.g PMMA or ZEP-520). The beam is scanned across the substrate (covered with resist), following the pattern that needs to be defined. During development, the exposed parts of the resist are removed (for a positive resist). Features with dimensions of a few nanometer can be defined using this technique. A disadvantage is the sequential nature of the technique, which makes it slow and not very well suited for high volume production. It is typically used in research and development and for photolithography mask fabrication.

3.1.2 Dry etching

Following lithography, the pattern needs to be defined in the semiconductor material through an etching technique. Often, an intermediate hard mask is used. All devices developed in this work require a high degree of etching verticality. Therefore, wet etching methods can not be used since they lead to profiles with isotropic or crystallographic characteristics. However, (dry) plasma etching methods can achieve a high etch anisotropy and dimensional control due to the utilisation of both physical and chemical etch components [71].

Reactive Ion Etching

A typical Reactive Ion Etching (RIE) configuration is shown in Figure 3.2. The vacuum chamber is filled with gases and a plasma is cre-

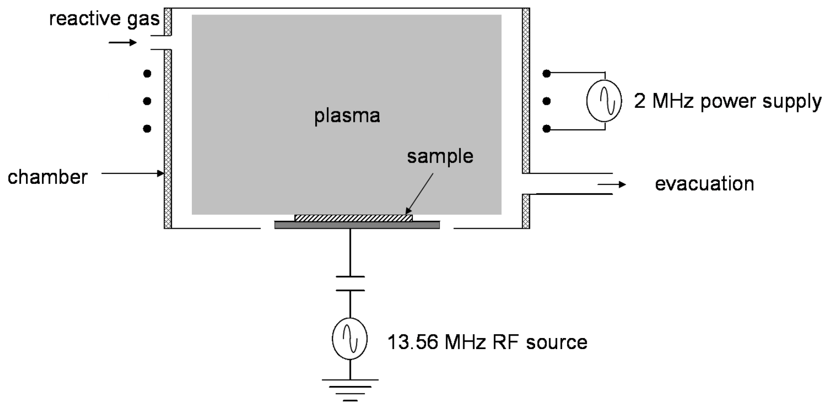

Figure 3.3: Inductively Coupled Plasma RIE (ICP-RIE) (from [71]).

ated by RF-excitation of two parallel electrodes. Ions are accelerated to the lower electrode (with the sample) and strike it at near-vertical incidence. This performs the etching. High process pressure and low voltages results in predominantly chemical etching of the substrate. Low pressure and high voltages results in physical ion sputtering of the substrate.

Inductively Coupled Plasma RIE Etching

Inductively Coupled Plasma RIE (Figure 3.3) is a high-density plasma etching technique. The plasma is generated in a chamber that is encircled by an inductive coil, and diffuses from the generation region towards the sample. The plasma has a high-density and low energy, as a result of which etching can occur with low damage and still obtaining high etch rates. ICP-RIE is used in this work for etching of InP membrane devices.

Chemically Assisted Ion Beam Etching

Chemically Assisted Ion Beam Etching (CAIBE) (Figure 3.4) uses a gridded ion source, which generates a collimated beam of ions. A plasma is created in the ion discharge chamber, from which the ion beam is extracted. A chemical etching component is introduced in the form of a reactive gas. Advantages of this etching method are the significantly increased etch rates and the low damage (due to the chemical etch component). The physical etch parameters (ion energy and current density)

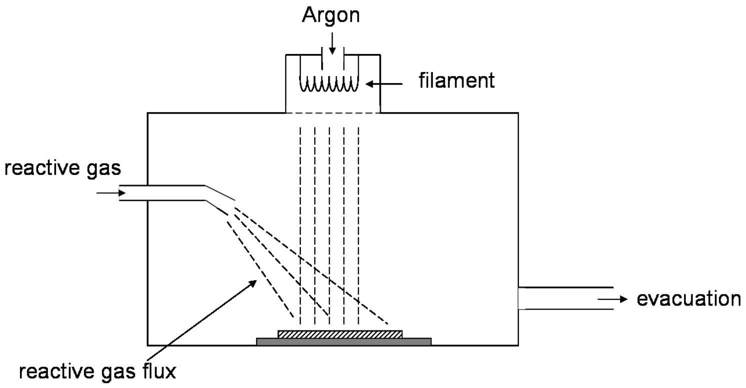

Figure 3.4: Chemically Assisted Ion Beam Etching (CAIBE) (from [71]).

and chemical etch parameters (reactive gas flow rate, sample temperature) can be varied almost independently.

CAIBE can also be used for angled etching. Due to the remote generation of the ion beam, the orientation of the sample can be changed during etching. For example, by tilting the sample relative to the ion beam, angled etching can be performed without creating a positive sloped or overcut profile.

CAIBE is used in this work for deeply etched structures in InP/InGaAsP heterostructures and slanted grating couplers.

3.2 Deposition methods

In this section we will give a short overview of the methods used for depositing thin layers, both metals and dielectrics, onto the chip surface.

Joule evaporation

This method is mostly used for depositing metal layers onto the chip and uses a vacuum chamber. A current is sent through a crucible containing the metal to be evaporated. The metal melts and the chamber is filled with metal vapour. The metal is also deposited onto the chips which are mounted upside down above the crucible. We have used this method for depositing gold bottom mirrors and detector contacts.

Sputtering

Sputtering can be done in the same machine used for Joule evaporation. In the vacuum chamber, there is a sputter unit next to the Joule evaporation unit. The sputter unit consists of a cathode made from the material to be deposited, an anode and a gas inlet. A plasma is created by applying a high voltage between anode and cathode. Ions created in this plasma (mostly Ar) are accelerated to the cathode and small pieces are eroded from it. These pieces fill the chamber and are deposited onto the chip surface. Sputtering has been used for depositing detector contacts.

E-beam evaporation

E-beam evaporation is done in a vacuum chamber and can be used for depositing both metals and dielectrics. An e-beam coming from an e-gun source is focused onto a crucible containing the material to be evaporated. The impact of the electrons makes the material melt and evaporate. The crucible can be cooled and the melting temperature of the material to be deposited can be higher than the melting temperature of the crucible, which is not the case in Joule evaporation. We have used this method for depositing SiO_2 layers.

Plasma Enhanced Chemical Vapor Deposition (PECVD)

The PECVD process is very similar to plasma etching. By applying a voltage between two electrodes, a plasma is created in a gas mixture in the chamber. The plasma contains electrons, ions and radicals, which react with each other and with the surface. Non volatile materials are formed and deposited onto the chip. The choice of the gases determines which material will be deposited. We have used PECVD for depositing SiO_2 layers onto the chip.

3.3 Processes for substrate type InP/InGaAsP

3.3.1 Deep and slanted etching using CAIBE

As discussed in Chapter 2, compact and efficient grating couplers can be obtained for substrate type InP/InGaAsP layer structures, provided that the grating teeth are very narrow and etched completely through

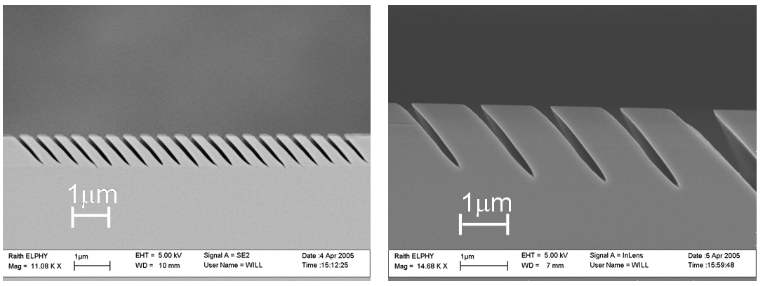

Figure 3.5: Angled InP/InGaAsP etching, performed at University of St. Andrews, UK. Left: Slanted CAIBE etching of narrow lines (100-150 nm) in InP/InGasP. Right: Slanted CAIBE etching of wider lines (300 nm and more).

the waveguide core under an angle. This implies that the aspect ratio, being defined as the ratio between depth and width of the etched feature, is high. As discussed above, angled etching can be performed using CAIBE.

A process for slanted CAIBE etching with high aspect ratio has been developed at the University of St. Andrews. To achieve the slanted etch profile, the sample is mounted on a slanted holder. Pictures of narrow lines etched under an angle of 45° are shown in Figure 3.5. First, the pattern is defined using e-beam lithography and PMMA resist and transferred into a SiO_2 hard mask with RIE using CHF_3 chemistry. Then, this hard mask pattern is etched at an angle into the InP/InGaAsP heterostructure using CAIBE with Cl_2 chemistry. The parameters of this process are described extensively in [72]. Lines of 150 nm width can be etched 800 nm deep, while 300 nm wide lines can be etched over 1.3 μm deep.

3.4 Processes for InP membrane

3.4.1 Shallow etching using ICP-RIE

A clear advantage of membranes is the fact that the required aspect ratio is moderate. The membrane layer typically has a thickness of $\lambda/2n$, which is $\sim$ 200-300 nm for semiconductor membranes. The aspect ratio of the features in this work is about 1:1. For all the structures, a 150 nm PECVD SiO_2 hard mask is used.

The patterning is done by e-beam lithography using PMMA or ZEP-520 as a resist. This pattern is transferred into the hard mask using RIE

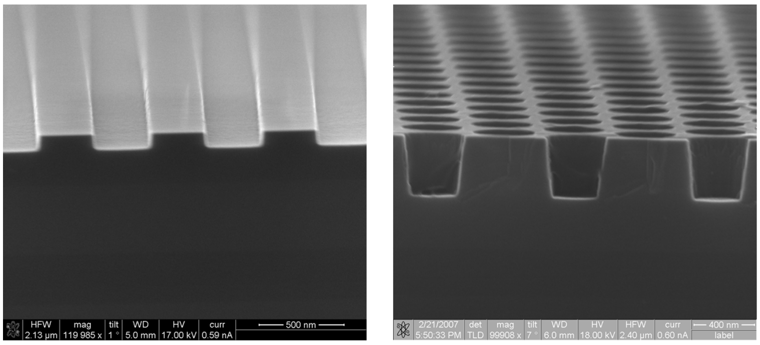

Figure 3.6: Left: 3-cycle InP etching of a grating. Right: 15-cycle etching of photonic crystal holes.

with CHF_3 chemistry. Both steps are performed at the University of St. Andrews. The pattern is then etched into the top InP membrane layer with ICP-RIE at Ghent University. The process is done in cycles, consisting of a 90 seconds InP etch step using CH_4/H_2, followed by a 60 seconds O_2 plasma cleaning step. One etching cycle typically removes 25-30 nm of InP. The InP etch parameters are: a CH_4/H_2 15/40 sccm mixture, RF power of 240 W, ICP power of 100 W, a pressure of 20 mTorr at 100°C. The O_2 plasma parameters are: 50 sccm , RF power of 100 W, ICP power of 150 W, a pressure of 40 mTorr. After etching the SiO_2 hard mask is removed using diluted Hydrogen Fluorid (HF).

Figure 3.6 shows results of the ICP-RIE InP etching. A shallow grating coupler typically requires 3 cycles of etching, while a photonic crystal etched through the membrane requires 15 cycles. The sidewall and etch floor roughness is low, but the sidewalls are not perfectly vertical, especially for the PhC holes. Further optimising of the etching parameters could improve this sidewall slope.

3.4.2 Bonding

The vertical index contrast that can be obtained through epitaxial growth is moderate. In order to achieve a high vertical index contrast, additional processing steps are required. In general, there are two ways for obtaining the membrane. The first approach is using local wet underetching of a sacrificial layer [73]. In that case a suspended semiconductor membrane in air is obtained. Special care needs to be taken when drying the samples in order to prevent sticking of the free-standing membrane to the substrate [74]. We have used bonding to obtain the high index contrast membrane.

Several types of bonding exist, each with their advantages and disadvantages. We will give a short overview of the most important techniques and then focus on adhesive wafer bonding using BCB, which is the method used in this work.

Direct bonding

In direct bonding two wafers are brought into contact and bonded together by applying pressure and/or a high temperature. The physical principle behind the initial bonding is the Van der Waals attraction force. After annealing the bonds become covalent. The surfaces of the wafers need to be very flat and clean, which may be difficult to obtain. In principle, a variety of material combinations can be bonded together. The high temperature often required (>500°C for some material combinations) is a drawback, especially when combining materials with largely different thermal expansion coefficients. In addition, it may cause problems for metallisation if processing is done before bonding and cause unwanted diffusion of dopants.

In molecular bonding, a thin SiO_2 layer is applied on both surfaces. A small amount of roughness can be removed by Chemical Mechanical Polishing (CMP) of the oxide layer, although the requirements on flatness and cleanliness of the substrates remain stringent. This approach was used to obtain the InP membranes in [12].

Anodic bonding

This type of bonding is used to bond glass substrates containing sodium (Na) to silicon substrates. By applying high temperature (around 300-500°C) and a high voltage (1 kV), sodium ions drift from the glass surface to be bonded, while oxygen ions remain at the surface. As a result, a depletion layer with large electric field is created and both substrates are bonded by $Si\text{-}O_2$ chemical bonds.

Metallic bonding

In metallic bonding, a metal is deposited on both substrates and after bringing them into contact the temperature is elevated until the metal melts and a bond is formed. Typical melting temperatures are in the range of 120-350°C. In most cases an eutectic alloy is used, the most common common material being AuSn. For some applications metal bonding is interesting for forming electrical contact between different materials.

Adhesive bonding

In adhesive bonding one or both substrates are covered with an adhesive layer, serving as the bonding agent. The advantage of this approach lies in the fact that in a lot of cases some roughness can be tolerated due to the planarising properties of the adhesive. Typically, the adhesive has a material dependent curing temperature and maximum temperature for post-processing. In literature, a wide variety of materials have been used, including SU8 [75], PMMA [76], spin-on-glass [77], etc.

We use DVS-BCB (divinilsiloxane-bis-benzocyclobutene)[1] from The Dow Chemical Company as the adhesive layer, a spin-on polymer widely used in the microelectronics industry. Interesting properties of this adhesive include: low cure temperature of 250°C, low dielectric constant, high degree of planarisation, transparency at telecom wavelengths, thermal stability, chemical resistance, low outgassing. The bonding process was developed in the PhD work of I. Christiaens [78] and G. Roelkens [79]. We have used and adapted this process for our application.

We perform die-to-wafer bonding (in contrast to wafer-to-wafer bonding) using the process depicted in Figure 3.7. We start from an epitaxially grown InP based layer structure, consisting of a thin InP membrane on an etch-stop layer (InGaAsP or InGaAs) on an InP substrate. The etch-stop layer can be selectively removed with regards to the surrounding InP layers. The pattern is defined before bonding (Figure 3.7a), using e-beam lithography and etching processes as described above. The advantage of this choice is that standard patterning processes for InP/InGaAsP can be used. Additionally, this approach allows for double-sided processing. The yield of the bonding process should be very high in this case, in order not to waste the patterning effort. This is the case when using thick (i.e > 1 μm) bonding layers. Pattern definition after bonding would also be possible, but then the patterning processes are less standard and need re-optimisation.

It is important that the substrates are very clean before bonding, especially when using thin bonding layers. The requirements are less stringent for the thicker bonding layers used in this work, since they

---

[1] We will use the short name BenzoCycloButene or BCB in this work.

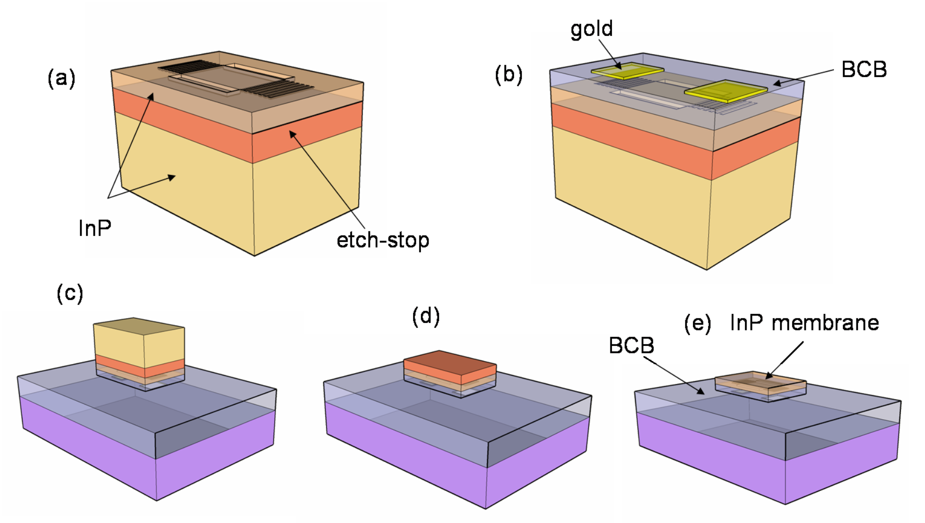

Figure 3.7: BCB wafer bonding process. (a) patterned InP sample to be bonded. (b) BCB buffer layer and gold mirror deposition. (c) bonding step. (d) InP substrate removal. (e) etch-stop layer removal.

can planarise some of the particles on the dies. Since the InP dies are patterned before bonding, we can not remove sacrificial layers as a cleaning method. However, the removal of the hard mask in diluted HF renders the InP surface hydrophilic, which has a positive influence on the bonding strength [79]. Afterwards, we use a simple cleaning of the III-V dies with acetone:IPA:DI-water.

After drying, a buffer layer with the appropriate thickness has to be applied onto the sample. This can be a deposited SiO_2 layer (PECVD or e-gun) or a spin-coated BCB layer. In the latter case, the spinning speed determines the layer thickness. A curve of layer thickness as a function of spinning speed is shown in Figure 3.8 for a 8x8 mm^2 non-patterned sample. In section 2.4.1 we have calculated the optimal BCB thickness to be 700 nm, which is obtained for a spinning speed of 9000 rpm. Next, the BCB buffer layer is hard cured in a N_2 environment using the temperature profile shown in Figure 3.9. Then, a gold layer is defined onto the gratings using Joule evaporation and lift-off. This layer will serve as the bottom mirror (Figure 3.7b).

This die is then bonded onto a host substrate using another BCB layer. Therefore, a BCB layer is spin coated onto a cleaned host substrate (Si, GaAs, pyrex, etc) and the host substrate is placed on a hotplate for 5 minutes at 150°C in order to evaporate remaining solvents.

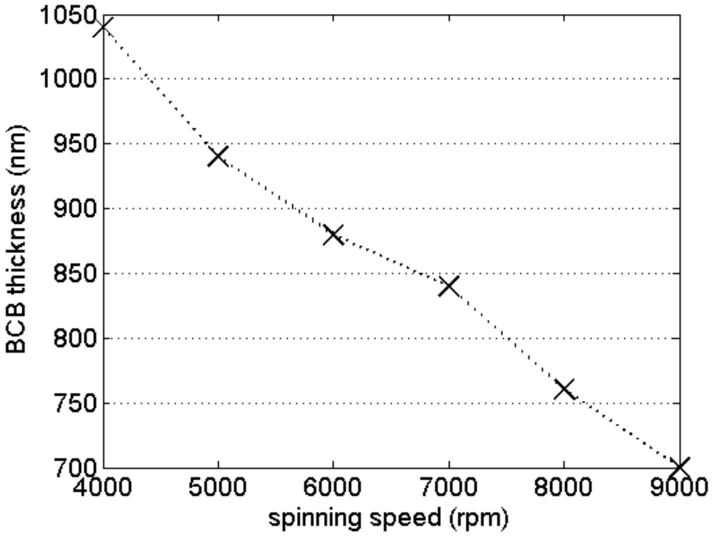

Figure 3.8: BCB thickness as a function of spinning speed.

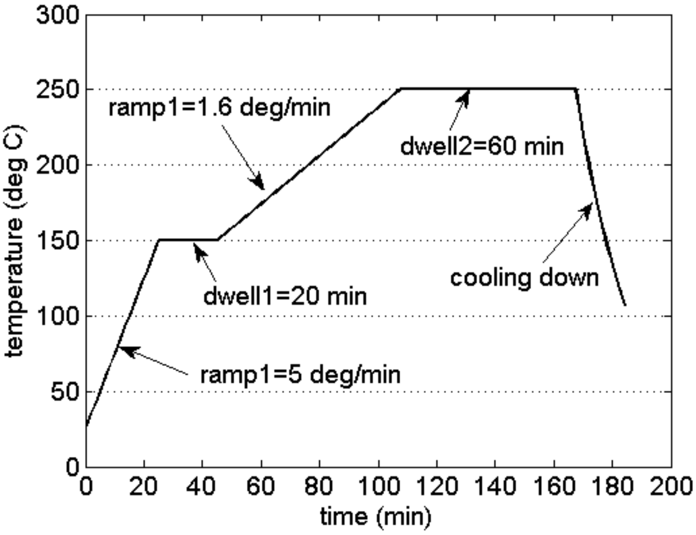

Figure 3.9: Temperature profile for hard curing of BCB.

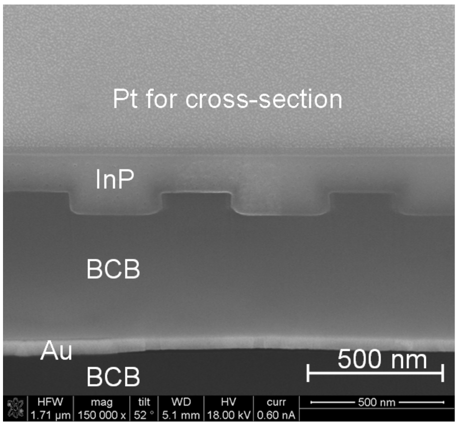

Figure 3.10: Cross-section of a bonded InP membrane grating coupler with bottom mirror.

Then, the InP die is brought into contact (epitaxial layers down) with the host substrate which is kept at 150°C (Figure 3.7c). Bonding can be done manually using (clean) tweezers to handle the substrates. When both substrates are in contact, included air bubbles are removed by moving the bonded sample around. This is possible since the BCB is liquid at 150°C. After bonding, the sample is cured following the temperature profile of Figure 3.9.

Then, the original InP substrate and etch-stop layer are removed. The InP substrate is removed by lapping, using a slurry of AlO_x powder suspension until a remaining thickness of $\sim$ 70 μm. The last part of the InP substrate is removed by selective wet etching in HCl (Figure 3.7d) . Finally the etch stop layer is removed by selective wet etching in $8H_2O$:H_2O_2:H_2SO_4 (Figure 3.7e). An SEM picture of a Focused Ion Beam (FIB) cross-section of a bonded InP membrane grating coupler with bottom mirror is shown in Figure 3.10.

3.4.3 Integration of detectors onto InP membrane

For the integration of detectors onto the InP membrane platform, the basic InP membrane layer structure needs to be extended with a p-i-n junction. The epistructure and doping levels are summarised in table 3.1. It consists of a 80 nm highly p-doped InGaAs contact layer, a 500 nm intrinsic InGaAs absorbing layer, a 300 nm slightly n-doped InP membrane layer, an InGaAs etch-stop layer on an InP substrate.

material	thickness (nm)	doping (1/cm^3)
InGaAs	80	p-type, 1 x 10^{19}
InGaAs	500	intrinsic
InP	300	n-type, 2 x 10^{17}
InGaAs	500	-
InP substrate	-	-

Table 3.1: Layer structure for integrating detectors onto InP membrane (from top to bottom).

The integration scheme is shown in Figure 3.11, starting from the epitaxial InP wafer (Figure 3.11a). First, the detector mesa is defined using optical contact lithography and etching until the InP membrane layer is reached. In order to avoid underetch of the resist mask, the first part of the mesa is dry-etched (ICP-RIE) and only the very last part of the mesa is wet-etched selectively with respect to the underlying InP layer. The result is shown in Figure 3.11b. A 150 nm SiO_2 hard mask is then PECVD-deposited for patterning (Figure 3.11c). The gratings, photonic crystals, waveguides, via holes, etc. are defined using e-beam lithography aligned to the detector mesas and etched into the hard mask (at the University of St. Andrews) (Figure 3.11d). Then, the pattern is etched into the InP membrane using a two-step etch process. First, photonic crystals and via holes are ICP-RIE-etched through the 300 nm InP membrane layer (15 cycles), while covering the gratings with photoresist (Figure 3.11e-f). Afterwards, the resist is removed (Figure 3.11g) and the whole pattern is etched for another 3 cycles (70-90 nm), in order to etch the gratings (Figure 3.11h). Then the photoresist is removed with acetone and the hard mask is removed with HF (Figure 3.11i). After this sequence, we obtain a pattern in InP, aligned to detector mesas.

Now the sample is ready for processing of the detector p-contact. A 700 nm BCB layer is spun onto the sample for passivation (Figure 3.11j) and hard cured for 1 hour at 250°C (Figure 3.9). Then the p-contact windows are defined using optical contact lithography, and opened by ICP-RIE etching of the BCB using SF_6 and O_2 (Figure 3.11k). A 20/200nm Ti/Au contact covering also the via hole is deposited using lift-off (Figure 3.11l). At this stage, a gold mirror for improving the grating coupler efficiency can also be deposited.

This die is then bonded onto a host substrate using a 1 μm BCB layer (Figure 3.11m), using the process described in previous section.

The last part of the processing involves the access to the p-contact and the definition of the n-contact. Therefore, another 700 nm BCB

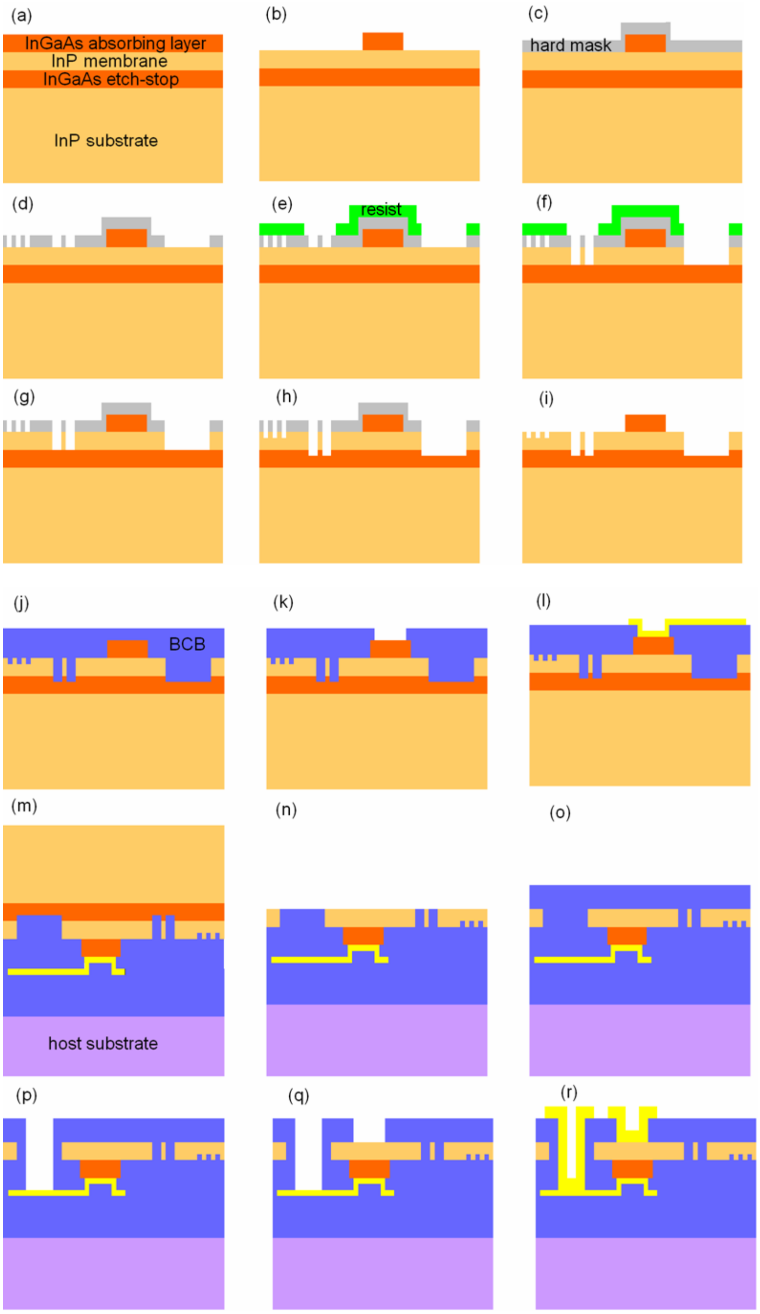

Figure 3.11: Integration of detectors onto InP membrane.

passivation layer is spun onto the sample (Figure 3.11o). Access to the p-contact is provided by BCB etching through the via hole, until the p-contact is reached (Figure 3.11p). Then the n-contact windows are defined and opened with another BCB etch (Figure 3.11q). Finally, a Au/Ge/Ni n-contact is deposited, and the p-contact is accessed from the top by filling the via hole with metal (Figure 3.11r).

An overview of the most important stages in the integration scheme are shown in the 3D pictures of Figure 3.12. Pictures of a sample at different stages of the processing are shown in Figure 3.13.

3.5 Processes for Silicon-on-Insulator devices

The technology for Silicon-on-Insulator nanophotonic integrated circuits was developed in the PhD work of W. Bogaerts [80] and is carried out at IMEC, Leuven. The whole process flow uses standard CMOS fabrication methods on SOI wafers having a 220 nm top guiding Silicon layer and a 1 μm or 2 μm buried oxide layer. Both Deep UV projection lithography at 248 nm and 193 nm are used to define the patterns. The patterns are etched into the Silicon layer with the resist pattern as a mask using Cl_2/O_2/He/HBr ICP-RIE. A two-step etch process has been developed in order to obtain shallow etched parts (70 nm) and deeply etched parts (220nm, full silicon top layer etch). The alignment accuracy between both lithography steps is of the order of 50 nm. We have used this process to fabricate focusing grating couplers. The two-step etch process is illustrated in Figure 3.14, showing a low contrast aperture.

3.6 Conclusions

In this chapter we have described the fabrication processes developed and used in this work, for different layer structures. The main part involved nanophotonic devices in InP membrane technology. In that case, e-beam lithography and dry-etching is used to define gratings, waveguides, photonic crystals, etc. Adhesive wafer bonding by means of BCB is used to obtain the InP membrane. A detailed scheme for integrating detectors onto this InP membrane platform is described and implemented.

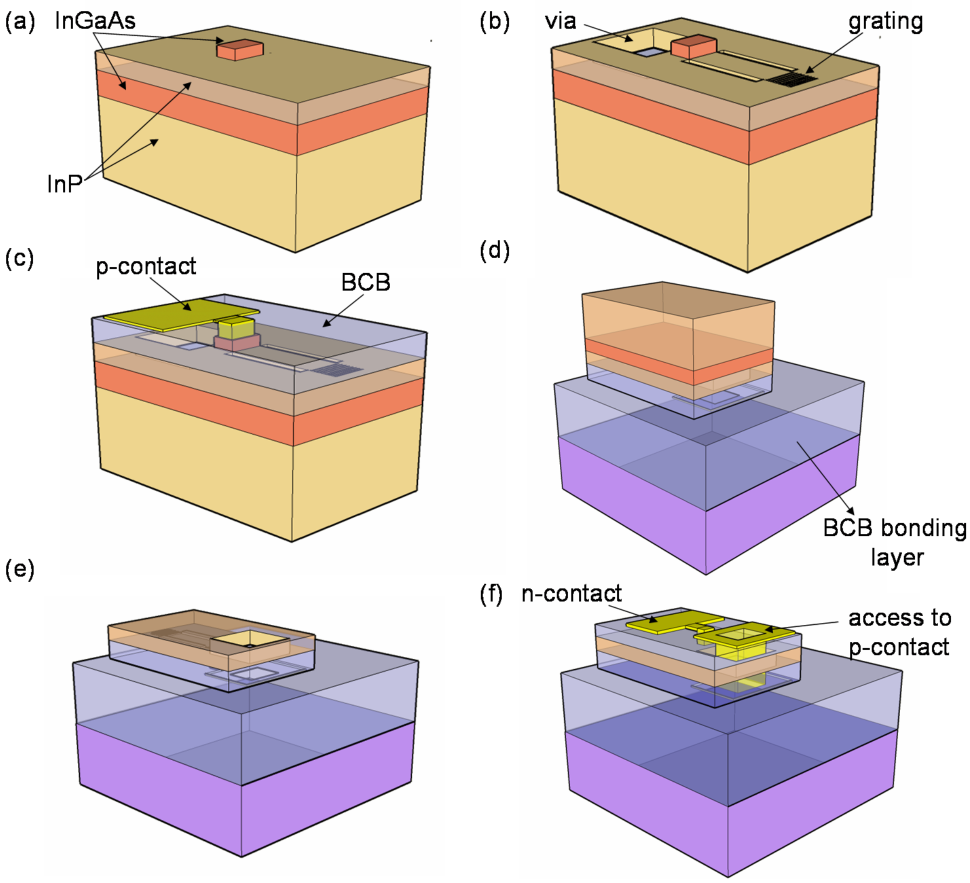

Figure 3.12: Important stages of the integration scheme. (a) detector mesa definition. (b) InP etching of pattern and via holes. (c) passivation and definition of the p-contact. (d) BCB bonding. (e) substrate removal and etch-stop layer removal. (f) n-contact definition and access to the p-contact.

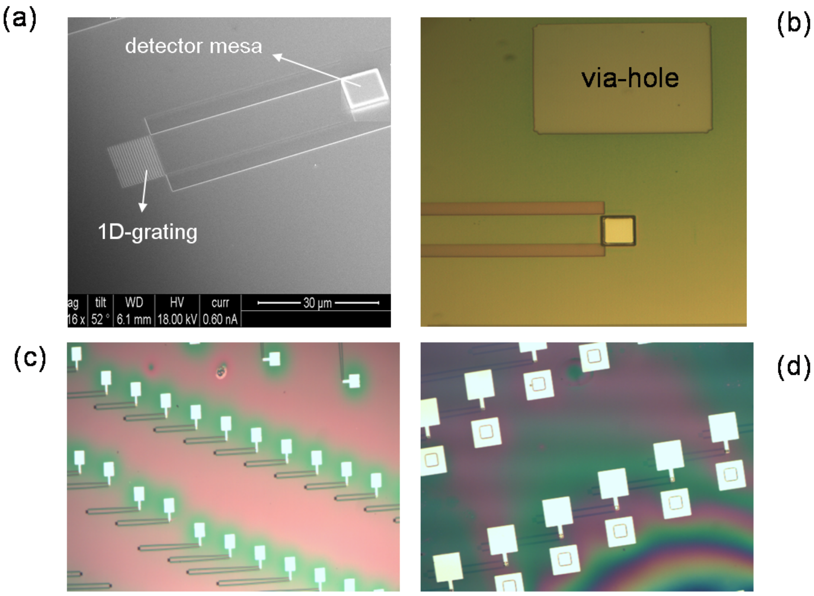

Figure 3.13: Pictures at different stages of the detector integration scheme (a) after mesa definition and InP etch. (b) after opening p-contact. (c) after p-contact lift-off (covering the via hole), before bonding. (d) final device.

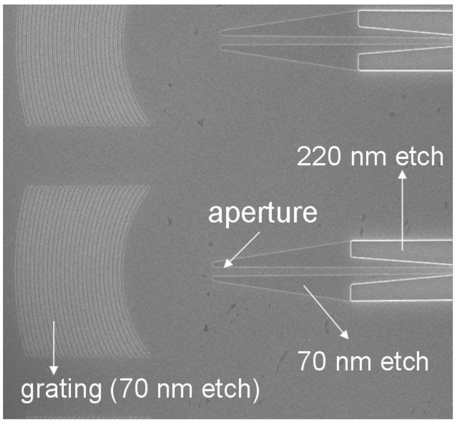

Figure 3.14: Low contrast aperture in SOI using a 2-step etch process.

Chapter 4

Characterisation of 1D grating couplers

In this chapter we will characterise the grating couplers designed in Chapter 2. The main part focuses on grating couplers in BCB bonded InP membrane. For the optimised versions we take advantage of the advanced and high volume processing capability of Silicon-on-Insulator integrated circuits. Experimental results for slanted grating couplers in InP/InGaAsP waveguides are shown. We compare the experimental results with simulations for the actual fabricated structures.

4.1 Characterisation method

The standard method for grating coupler characterisation at INTEC is shown in Figure 4.1. The sample typically consists of an input grating coupler, a connecting waveguide circuit and an output grating coupler. A fibre connected with a tunable laser is positioned over the grating at a distance of approximately 10 μm. At the output, a fibre connected with a photodetector is positioned over the output grating. In most cases, both fibres are tilted 10 degrees from vertical position in order to avoid second order reflections. The transition to single-mode photonic wires is omitted in these test structures. Therefore, waveguide losses can be neglected since the waveguides are 3-12 μm wide. By assuming that input grating and output grating are identical, the coupling efficiency of a single grating coupler can be calculated from :

$$\eta = \sqrt{P_{in}/P_{out}} \tag{4.1}$$

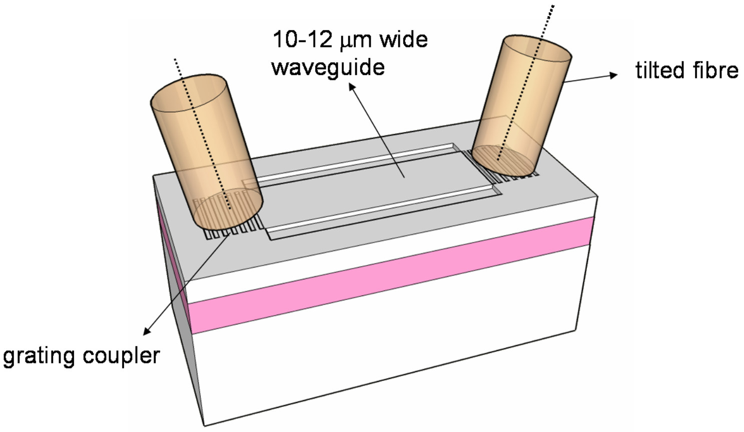

Figure 4.1: Fibre-to-fibre characterisation of grating couplers.

where P_{in} is the optical power reaching the input grating and P_{out} is the optical power measured at the detector.

4.2 Membrane type grating coupler structures

4.2.1 BCB bonded InP membrane grating couplers

First and second generation gratings have been fabricated in the framework of the European IST-FUNFOX project. E-beam lithography and pattern transfer into the hard mask have been performed at the University of St. Andrews, while InP etching and bonding have been performed at INTEC.

First generation gratings (300 nm InP membrane)

The first generation gratings are fabricated following the optimal design with additional Al_2O_3 top layer. They show an experimental coupling efficiency of 19% without top layer, which increases to 30% after applying an Al_2O_3 top layer. The experimental coupling efficiency is substantially lower than calculated for the optimal design (53%), which is caused by deviations between fabricated structure and design. The parameters of the grating structure are extracted from an SEM picture after making a cross-section using Focused Ion Beam (FIB) (Figure 4.2a). The etch depth of the grating is 139 nm (design: 130 nm), the bonding BCB layer thickness is 1.3 μm (design: 1.17 μm) and the Al_2O_3

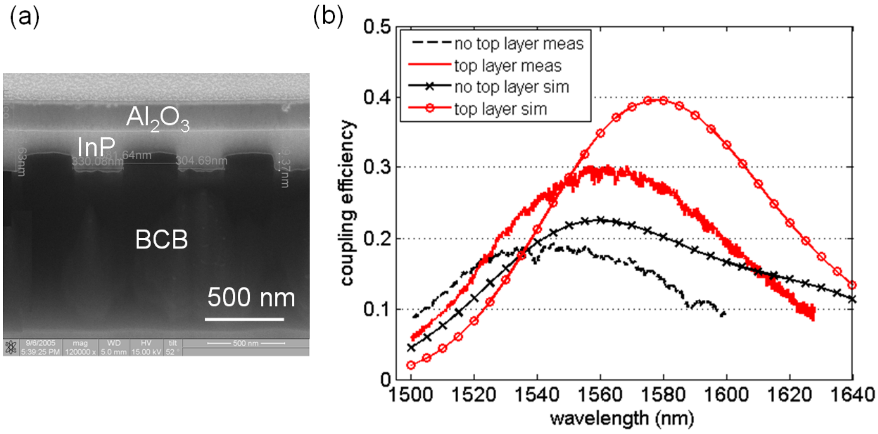

Figure 4.2: First generation grating couplers. (a): SEM picture of a cross-section, with Al_2O_3 top layer. (b) Measurement and simulation for the fabricated structure, with and without Al_2O_3 top layer.

layer thickness is 240 nm (design: 270 nm). In Figure 4.2b, a comparison between simulation of the fabricated structure and the experimental results is shown. We observe a wavelength shift of 20 nm between theory and simulation. All parameters of the structure (including refractive indices, filling factor, period, etch depth) have an influence on the coupling wavelength, so they should all be known to a very high precision. For the case without top layer, the experimental coupling efficiency is only slightly lower than the theoretical value. The discrepancy increases when adding the top layer, indicating that the quality of this layer is not optimal.

Second generation gratings (300 nm InP membrane)

The second generation gratings are fabricated following the optimal design without additional top layer. The etch depth is reduced to 91 nm, while the BCB thickness (1.13 μm) is close to the optimal value (1.2 μm). On top of the sample, a BCB layer of 442 nm is applied, serving as a passivation layer for detector structures elsewhere on the sample. The measured coupling efficiency is 33%, while the theoretical coupling efficiency for this structure is 38% (Figure 4.3b). We observe the same wavelength shift of 20 nm between experiment and simulation.

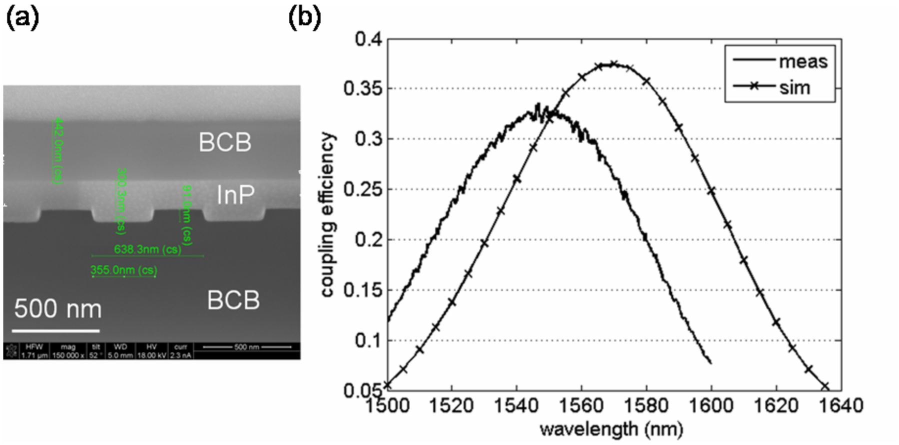

Figure 4.3: Second generation grating couplers. (a): SEM picture of a cross-section. (b) Measurement and simulation for the fabricated structure.

Third generation gratings (200 nm InP membrane)

In the framework of a collaboration with the Technical University, Eindhoven (The Netherlands), we have fabricated grating couplers in a 200 nm InP membrane. Both e-beam lithography and InP etching are performed in Eindhoven. The measured coupling efficiency is 46%, while the maximum theoretical coupling efficiency for a 200 nm InP membrane is 71%. The fabricated structure deviates slightly from the optimal design. The etch depth is 118 nm (design: 110 nm) and the BCB thickness is 1.33 μm (design: 1.2 μm). A comparison between measurement and simulation for the fabricated structure is shown in Figure 4.4. A wavelength shift of 7 nm is observed between both, together with a discrepancy of 13% in coupling efficiency.

4.2.2 Grating couplers with gold bottom mirror

In order to further improve on the coupling efficiency, we have fabricated the optimised designs with gold bottom mirror from section 2.4.1. By adding the bottom mirror, radiation towards the substrate is avoided. The Silicon-on-Insulator design was used to proof the principle and develop the technology. Afterwards, BCB bonded InP membrane versions were implemented.

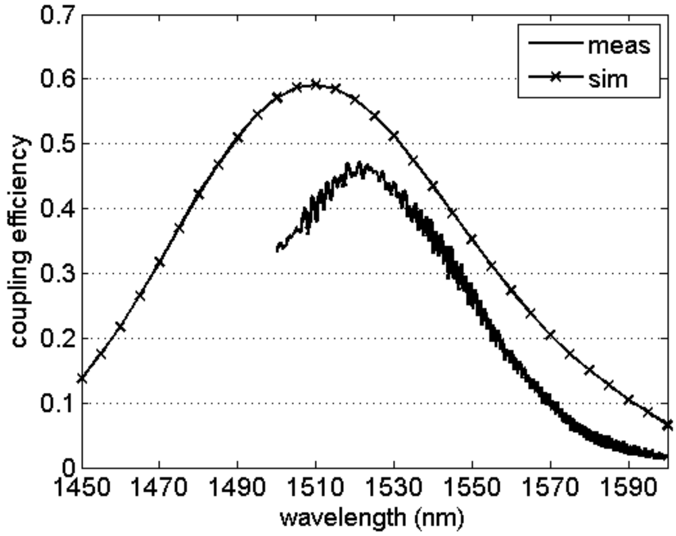

Figure 4.4: Third generation grating couplers on 200 nm InP membrane. Measurement and simulation for the fabricated structure. The minimum wavelength of the tunable laser source used for the measurements is λ=1500 nm.

Silicon-on-Insulator grating with gold mirror

The grating structure uses 2 BCB layers, a buffer layer between grating and bottom mirror and a bonding layer. First, the BCB buffer layer with appropriate thickness (840 nm in this case) is spin-coated onto the SOI die. After curing, a gold layer is deposited onto the gratings and the die is bonded with another BCB layer onto a host substrate. Finally, the silicon substrate is removed while the buried SiO_2 layer remains as the top layer. Pictures of the structure are shown in Figure 4.5, prior to and after bonding.

On this sample, only the input coupler has a gold bottom mirror. First, the coupling efficiency of a bonded grating coupler without bottom mirror is determined by measuring the transmission of reference structures (without mirror). From this measurement, the coupling efficiency is deduced to be 26%. This value is then used for determining the coupling efficiency of a grating coupler with bottom mirror. The results are summarised in Figure 4.6, together with the simulated coupling curves. The measured coupling efficiency is 69%. Apart from the wavelength shift there is good correspondence between simulation and experiment.

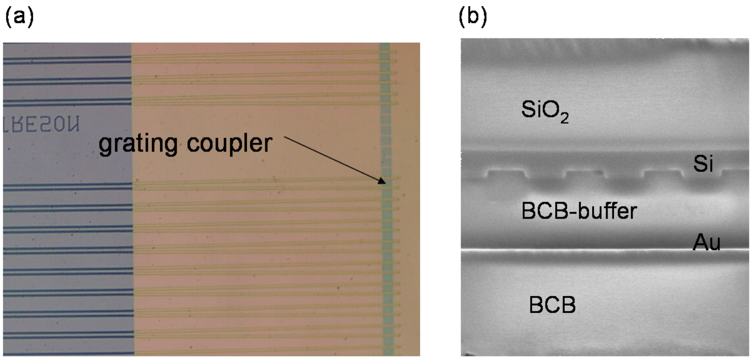

Figure 4.5: (a) Top-view of the fabricated SOI structure with bottom mirror, prior to bonding. Gratings are poorly visible due to the gold. (b) SEM picture of a FIB cross-section, after bonding.

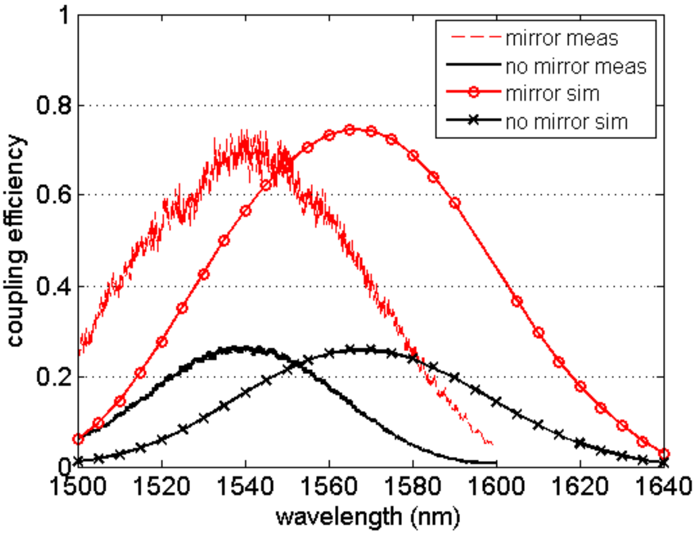

Figure 4.6: Characterisation of bonded SOI grating couplers with and without gold bottom mirror.

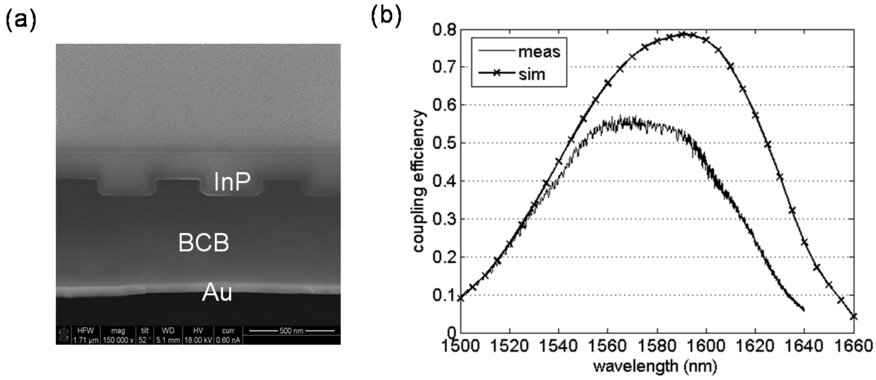

Figure 4.7: Characterisation of BCB bonded InP membrane grating couplers with gold bottom mirror and BCB buffer layer. (a) SEM picture of a cross-section, showing nearly perfect planarisation. (b) Measurement and simulation for the fabricated structure.

InP membrane (300 nm) grating with BCB buffer and gold mirror

Here, both input and output grating couplers have a bottom mirror. Figure 4.7 shows the results for a grating coupler where we bonded directly on a gold coated substrate. The experimental coupling efficiency is 56%. The fabricated structure has a lower filling factor than designed (41% instead of 50%) and the etch depth is 84 nm (design: 70 nm). The BCB buffer thickness is 1.18 μm (design: 1.23 μm). Still, there is a relatively large discrepancy between experiment (56%) and simulation (78%).

InP membrane (300 nm) grating with SiO_2 buffer and gold mirror

The structure with gold mirror and BCB buffer layer from previous section was close to target. However, it is very difficult to reproduce the buffer thickness between grating and mirror, especially if the BCB buffer layer also serves as the bonding layer. Since this buffer thickness is very critical, we have fabricated a structure where a SiO_2 (instead of BCB) buffer layer is PECVD-deposited. This process has better thickness control and reproducibility than spin-coated BCB, but planarisation is less good.

A cross-section of the structure is shown in Figure 4.8a. The PECVD SiO_2 planarises to some extent, and smoothens out the rectangular profile of the grating at the mirror side. However, the grating profile is

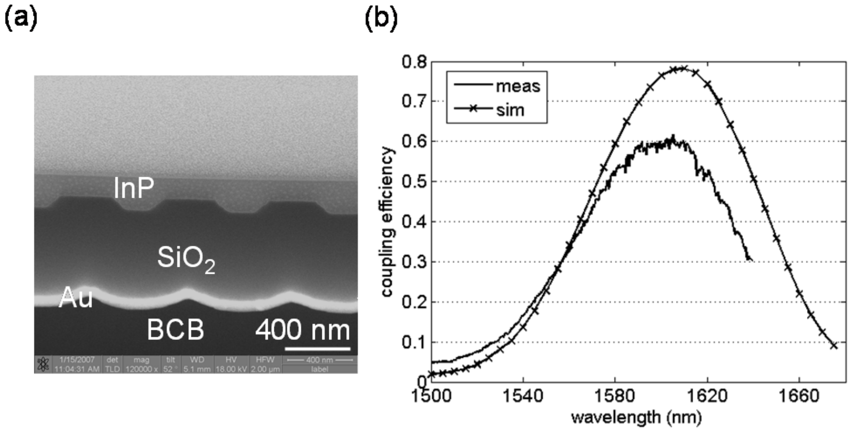

Figure 4.8: Characterisation of BCB InP membrane grating couplers with gold bottom mirror and SiO2 buffer layer. (a) SEM picture of a cross-section, showing planarisation to some extent. (b) Measurement and simulation for the fabricated structure.

still visible in the Au layer, which is not the case for the nearly perfect planarising BCB. The measurement results are shown in Figure 4.8b. The experimental coupling efficiency is increased to 60%. The buffer thickness is close to target (690 nm instead of 720 nm designed) with a reproducible process and the etch depth is 67 nm (design 70 nm). The theoretical coupling efficiency calculated for a perfect planarising SiO$_2$ layer (which is an approximation) is 77%.

4.2.3 Focusing grating couplers in Silicon-on-Insulator

In this section, the length of the coupling structure will be minimised in order to increase the integration density on the chip. For coupling to a functional integrated circuit the length of the coupling structure is mainly determined by an adiabatic transition from 10-12 μm wide waveguides to 500 nm wide single mode photonic wires. By focusing the light onto the wires this long transition (typically $>$150 μm) can be omitted.

We have implemented focusing grating couplers in two versions. The difference between both is the transition to the single-mode wire. In a first configuration, a short taper is used to "guide" the focusing wave onto the wire. In a second configuration, the light is focused in the slab onto a low lateral refractive index contrast aperture, which reduces

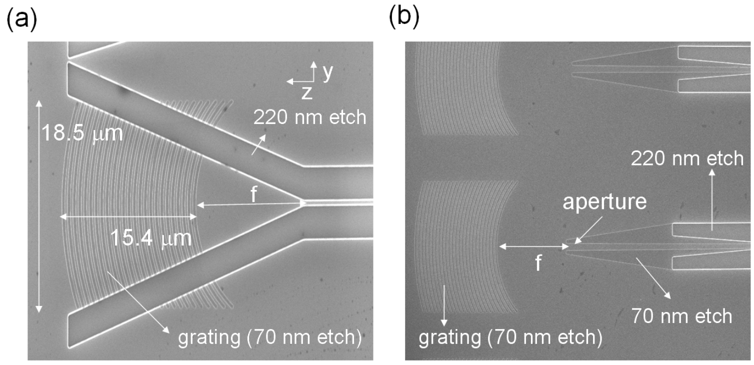

Figure 4.9: Focusing grating couplers in two configurations. (a) With short taper. (b) With low contrast aperture.

reflections at the interface. In that case, the transition from low contrast to high contrast photonic wires is done adiabatically over a length of 30 μm. Both versions are illustrated in Figure 4.9, with typical dimensions indicated.

Short taper vs low contrast aperture

We have measured the performance of the focusing grating couplers for designs with different focal distances in the two configurations. For all measurements the input couplers are focusing grating couplers, while the output couplers are standard linear grating couplers with known efficiency. Reference structures with standard linear grating input and output couplers are also included. The fibre-to-fibre transmission measurements are shown in Figure 4.10.

In the short taper configuration we have considered designs with focal distances of 12 μm and 32 μm (equal to the length of the "assisting" taper). The opening angle of the taper determines the grating design, as described in section 2.4.2. In the first design, having a short focal distance, the grating lines have a relatively strong curvature, while for the latter design this curvature is rather modest. No performance penalty is observed for both focusing grating couplers as compared to standard linear gratings.

In the low contrast aperture configuration we consider two designs for two different widths of the aperture. The focal distance (and the grating curvature) is determined by the opening angle of the aperture. A low contrast aperture of 0.8 μm width corresponds with a focal distance

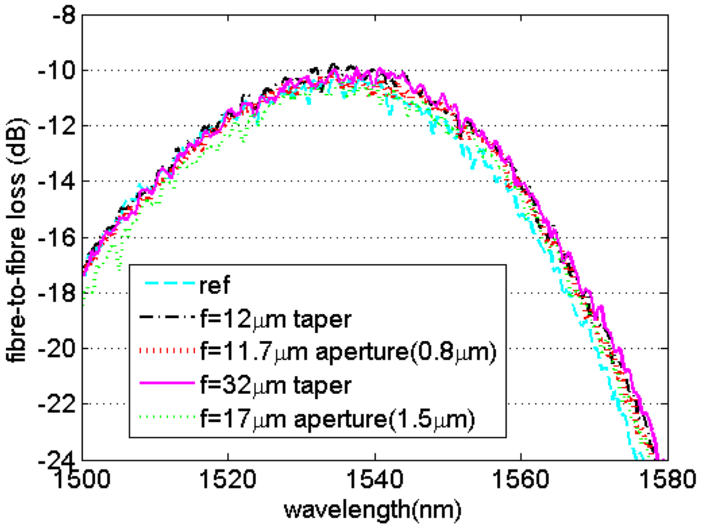

Figure 4.10: Transmission measurements for focusing grating couplers in short taper and low contrast aperture configuration. Differences in peak transmission are barely visible.

of 11.7 μm, while a low contrast aperture of 1.5 μm width corresponds with a focal distance of 17.1 μm. In this configuration, no performance penalty as compared to standard linear gratings is observed.

Influence of defocus

For all designs described in the previous paragraph we have investigated the influence of a defocus. For the short taper configuration this means that the wire is put closer (negative defocus) or further away (positive defocus) from the grating (which is kept identical) and that the "assisting" taper becomes shorter or longer. For the low contrast aperture configuration, the slab area where the focusing occurs becomes shorter or longer. The results are summarised in Figure 4.11.

For the short taper configuration and the design with focal distance of 32 μm, there is no influence at all of defocus. This indicates that the taper is very effective in the guiding of the light onto the wire. This is totally different for the design with focal distance of 12 μm. A negative defocus of 5 μm results in 1.2 dB excess loss, a positive defocus of 5 μm in 0.5 dB excess loss and a positive defocus of 10 μm in 3 dB excess loss. In the case of a negative defocus, the taper is too steep to "assist"

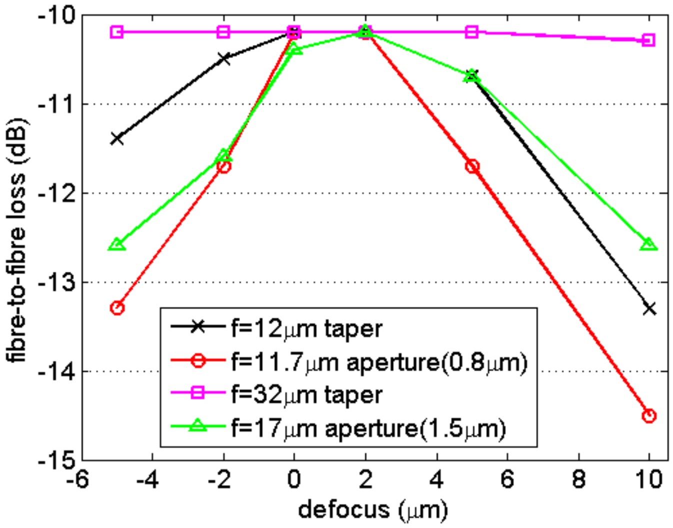

Figure 4.11: Influence of defocus for focusing gratings in short taper and low contrast aperture configuration.

the focusing without extra loss. In the case of a positive defocus, the spot is smaller than the taper width at the designed focal point, so the "guiding effect" of the taper is not fully exploited any more.

For the low contrast aperture configuration with aperture width of 1.5 μm (focal distance of 17.1 μm), a negative defocus of 5 μm results in 2.4 dB excess loss, a positive defocus of 5 μm in 0.5 dB excess loss and a positive defocus of 10 μm in 2.4 dB excess loss. The optimal focal distance is equal or slightly higher than the value resulting from the calculations. The narrow aperture (0.8 μm, corresponding to 11.7 μm focal distance) is more sensitive to defocus. A negative defocus of 5 μm results in 3.1 dB excess loss, a positive defocus of 5 μm in 1.5 dB excess loss and a positive defocus of 10 μm in 4.3 dB excess loss.

4.3 InP/InGaAsP slanted grating couplers

Previous measurements were for high vertical index contrast membrane type grating couplers (BCB bonded InP membrane or SOI). Here, we will characterise the two elaborated designs for slanted grating couplers in low vertical index contrast substrate type InP/InGaAsP waveguides. SEM pictures of a cross-section of fabricated couplers are shown

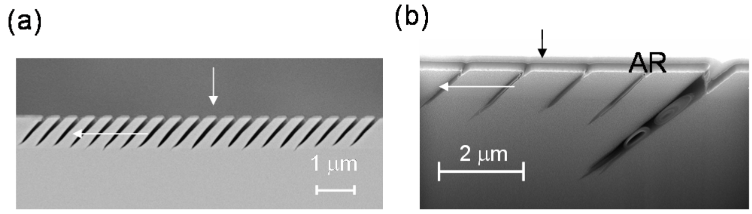

Figure 4.12: SEM pictures of slanted grating couplers. (a) first order slanted grating. (b) third order slanted grating.

in Figure 4.12. Some voids originating from depositing an Al_2O_3 AR-coating after etching can be seen. The samples were fabricated at the University of St. Andrews, except for the AR-coating which was deposited at INTEC.

The measurement method deviates from standard fibre-to-fibre measurements. Input and output grating would require different angles (-45 ° and +45 °), which can not be done in a single etching step. Therefore, we have chosen to fabricate only one slanted input grating coupler in an InP/InGaAsP waveguide. The light coupled from the fibre to the waveguide is collected at a cleaved facet using a microscope objective and measured by a detector. For these designs, the fibre is positioned vertically above the grating.

The method for calculating the grating coupler efficiency from this transmission measurement is described in detail in [39]. In these calculations, Fabry-Perot cavity effects between grating and output facet are taken into account. From the depth of the measured Fabry-Perot fringes, and with the known reflectivity at the output facet, the grating reflection can be calculated. All cavity parameters are then known, and the relation between transmission efficiency and coupling efficiency can be calculated. The transmission efficiency is defined as:

$$\eta_{trans} = \frac{P_{in}}{P_{detector}} \tag{4.2}$$

The relation between transmission efficiency and coupling efficiency is shown in Figure 4.13 for different reflectivities of the grating. The curves are calculated by a transfer matrix method using a fixed facet reflectivity of 28% and a cavity length of 1 mm.

The transmission efficiency of the first order slanted coupler (only without AR-coating) and of the third order slanted coupler (without and with AR-coating) are shown in Figure 4.14. The depth of the fringes

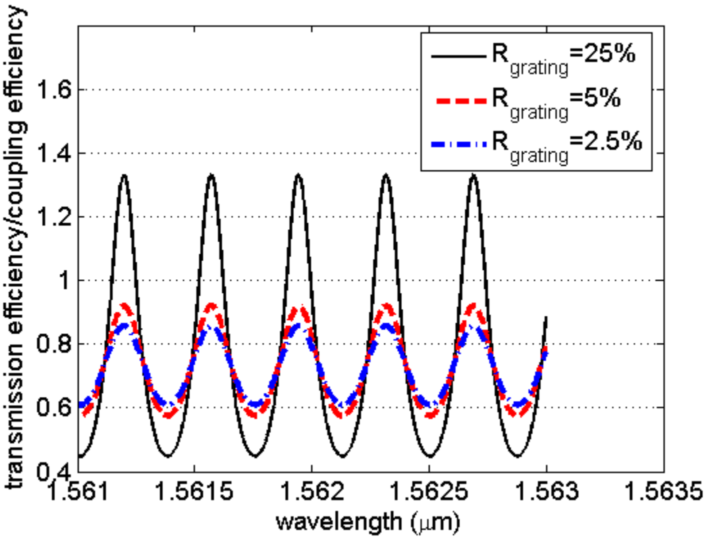

Figure 4.13: Relation between transmission efficiency and coupling efficiency calculated by a transfer matrix method, for different reflectivities of the grating.

(ratio between maximum and minimum) is used for determining the grating reflectivity and the coupling efficiency using Figure 4.13. For the third order grating without AR-coating the grating reflectivity is 6%, which decreases to 3.5% when adding the AR-coating. For the first order grating without AR-coating, the reflectivity is 2.2%. These reflectivities are substantially lower than calculated in the simulations in paragraph 2.5. For the third order slanted coupler, the coupling efficiency is 14% and 16% without and with AR-coating, respectively. For the first order slanted coupler, the coupling efficiency is 8%.

The measurements show a rather large deviation from the optimal calculated coupling efficiency, which is 48% for the third order coupler with AR-coating. However, the fabrication of the devices is very challenging. It is very difficult to etch narrow slots (50 or 150 nm) very deep (1.0 μm and preferably more) at an angle. This etch depth is required to capture all of the mode and radiate the power upwards. In addition, if the slots are wider than designed, most of the light is coupled out by only the first few slots, resulting in a poor overlap with the fibre mode. For the actual fabricated first order coupler (vertical etch depth of 850 nm, slot width of 70 nm), the calculated coupling efficiency (no AR-coating) is 28%. For the actual fabricated third order coupler (vertical

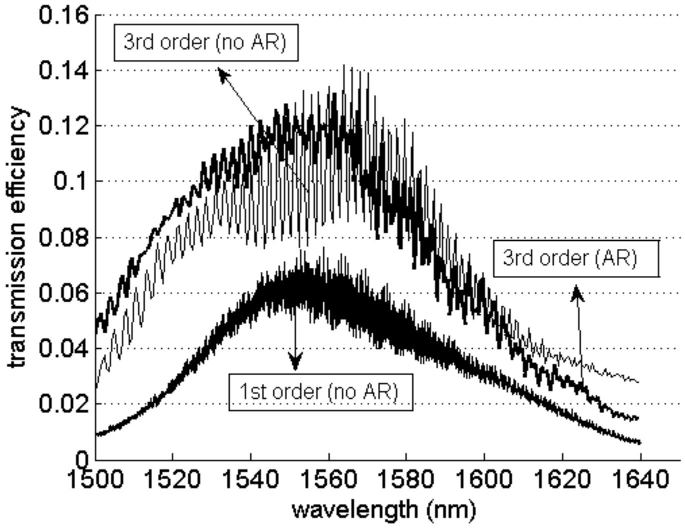

Figure 4.14: Characterisation of slanted grating couplers.

etch depth of 1.1 μm and slot width of 138 nm, except for the last one), the calculated coupling efficiency is 33% (without AR-coating) and 45% (with 267 nm Al_2O_3 as AR-coating). Although nice in concept, this type of grating coupler has proven to be very hard to fabricate, and satisfying experimental results have not been obtained. Intensive optimisation of the fabrication, together with more fabrication tolerant designs is required to make this type of grating coupler a viable option.

4.4 Overview

In table 4.1, we give an overview of the fabricated grating couplers and their theoretical and experimental coupling efficiency. For BCB bonded InP membrane grating couplers, the coupling efficiency improved from 30% for first generation gratings to 60% for optimised gratings with bottom mirror. For bonded SOI grating couplers with bottom mirror, the experimental coupling efficiency is 69%.

We have compared the experimental performance with the performance expected from simulations, with parameters extracted from cross-sections of the grating. In almost all devices, we observe a wavelength shift between experiment and simulation. This can be explained by the fact that every grating parameter (etch depth, filling factor, period, re-

layer structure	maximum	experimental	simulated
300 nm InP membrane, top layer	53%	30%	39%
300 nm InP membrane	42%	33%	38%
200 nm InP membrane	71%	46%	59%
300 nm InP membrane, gold mirror, BCB buffer	78%	56%	78%
300 nm InP membrane, gold mirror, SiO_2 buffer	78%	60%	77%
bonded SOI, gold mirror, BCB buffer	72%	69%	72%
InP/InGaAsP, 3^{rd} order, AR	48%	16%	45%
InP/InGaAsP, 1^{st} order, no AR	43%	8%	28%

Table 4.1: Overview of fabricated grating couplers and their performance. The used layer structure, the maximum theoretical coupling efficiency, the experimental coupling efficiency and the theoretical efficiency of the fabricated structure are indicated.

fractive indices) influences the peak wavelength of the grating coupler. The precision of extracting these parameters from cross-sections or ellipsometry (refractive index) is limited to some extent, and these errors add up to the observed wavelength shift. However, they do not influence the peak coupling efficiency that much to explain the discrepancy in coupling efficiency between experiment and simulation. This discrepancy is relatively large for InP based grating couplers (BCB bonded membrane and InP/InGaAsP), while for SOI grating couplers, the correspondence in coupling efficiency is good. This gives an indication that the processes for obtaining the InP gratings (e-beam lithography, etching) induce some extra loss (e.g. through roughness, non verticality) as compared to the advanced CMOS processes used for Silicon-on-Insulator circuits.

4.5 Conclusions

In this chapter, we have characterised 1D grating couplers, which were designed in Chapter 2. The main part concentrated on high vertical index contrast grating couplers. Three generations of basic BCB bonded InP grating couplers were fabricated and characterised. The best experimental result for a standard grating design is a coupling efficiency of 46%. The coupling efficiency can be further increased by adding a bottom mirror to the structures, resulting in experimental values of 69% and 60% for SOI and InP membrane respectively. The length of the coupling structure can be decreased by a factor of 8 without performance penalty by implementing focusing through curved grating lines. This results in a footprint of the coupling structure of 18.5 x 28 μm^2.

Slanted grating couplers for low vertical index contrast InP/InGaAsP waveguides grating couplers were experimentally demonstrated, but the experimental coupling efficiency is low. However, fabrication of this type of couplers is very challenging.

Chapter 5

Grating coupled integrated devices in bonded InP membrane

In this chapter we will use the InP membrane grating couplers from Chapter 4 to couple to other integrated devices. A difference is made between photonic wire based devices and photonic crystal devices. First we characterise the propagation loss of photonic wires. Afterwards, we characterise wire based notch filters and power splitters. Then, a photonic crystal (PhC) based wavelength demultiplexer is discussed. Finally, we integrate passive membrane devices with p-i-n photodetectors. In the next chapter polarisation diversity will be added to these integrated devices.

5.1 Photonic wires vs photonic crystals

5.1.1 Photonic wires

"Photonic wire" is a term typically used for membrane type waveguides. They use the refractive index contrast, both in plane and vertically, to confine the light to a small volume through total internal reflection (Figure 5.1a). For single-mode operation the dimensions of the waveguides are typically a few hundred nm. An important amount of the propagation loss in a photonic wire is caused by scattering due to sidewall roughness. The smaller the wire cross-section, the higher the propagation loss. State-of-the-art SOI photonic wire loss at INTEC is

2.4 dB/cm for 220 x 500 nm^2 wires fabricated using DUV lithography [81], while recently losses of 0.92 dB/cm have been reported by Glasgow University for photonic wires with the same dimensions. They use a hydrogen silsesquioxane e-beam resist [82] for pattern definition. Losses for membrane photonic wires in other materials are less frequently reported. In [83], a loss of 50 dB/cm is achieved for 300 x 300 nm^2 GaAs nanowires using BCB bonding. In [84], the loss of 2 x 2 μm^2 suspended waveguides in InGaAsP, with lateral tethers for support, is 2.2 dB/cm.

5.1.2 Photonic crystals

Photonic crystals are structures having periodicity and a high index contrast on a wavelength scale in one, two or three dimensions. The gratings used in this work can also be seen as photonic crystals. The theoretical basis of photonic crystals is described in [85], the most important feature being the possibility to achieve a photonic bandgap (PBG). This is a range of frequencies (wavelengths) where propagation through the crystal is forbidden.

The most widely used photonic crystal structures are periodic in two dimensions. The in-plane confinement is provided by the photonic band gap, while total internal reflection is used for the vertical confinement. In the holes there is no vertical confinement but radiation losses can be avoided by operating under the so-called light line. By perturbing the crystal, a localised mode or a set of closely spaced modes can exist having frequencies inside the photonic bandgap. These defect modes can not penetrate the rest of the crystal (since they are located in the photonic bandgap), and the light is pinned to the defect. A common way for perturbing the crystal is by removing holes or rows of holes. By removing a single or several holes, very small cavities can be created where the light can not easily escape. By removing a single row or several rows of holes (i.e. making a line defect), a waveguide can be created (Figure 5.1b). Losses are important in photonic crystals, even when working under the light line. Since the sidewall surface is larger than an equivalent photonic wire, they are more sensitive to scattering loss. Futhermore, inaccuracies in position (disorder) can cause additional loss.

The loss in a W_1[1] photonic crystal waveguide is still an order of magnitude higher than what has been achieved in conventional pho-

---

[1] A W_1 waveguide is obtained by removing a single row of holes from the crystal.

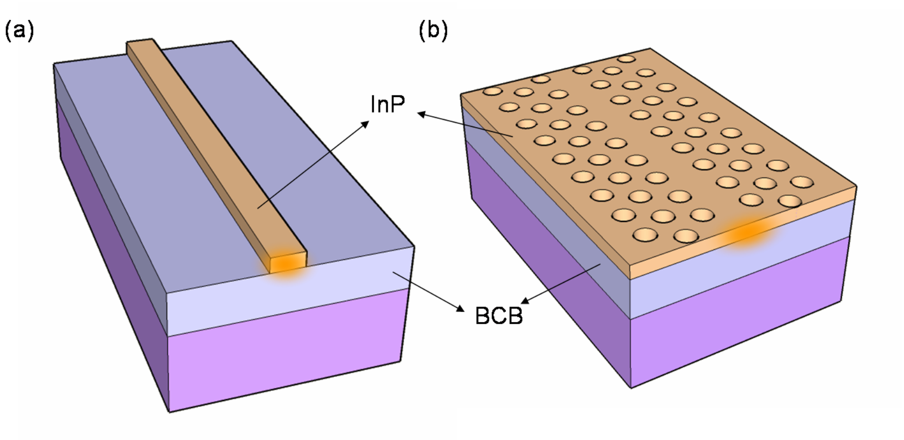

Figure 5.1: (a) Photonic wire waveguide. (b) Photonic crystal waveguide.

tonic wire waveguides. For SOI W_1 waveguides, a loss value of 14.2 dB/cm was reported in [5] using 193 nm DUV lithography. A similar value of 15 dB/cm was reported in [86] using e-beam lithography. For membrane W1 PhC waveguides using an air undercladding obtained by local underetching, the loss can be lower. Reported loss values are 2 dB/cm for Si [87], 5 dB/cm for GaAs [88] and 25 dB/cm for InP [89].

5.2 Photonic wire based devices

5.2.1 Photonic wire propagation loss

In order to determine the photonic wire propagation loss of our structures, we have fabricated photonic wires with different lengths. E-beam lithography and two-step etching were performed at TU Eindhoven, The Netherlands, on a 200 nm InP membrane. The photonic wires are etched completely through the InP membrane, while the light is coupled to and from the waveguides using third generation gratings (section 4.2.1) having a shallow etch.

On a first sample, the wire lengths are 500, 300, 100 and 50 μm. The fibre-to-fibre loss is shown in Figure 5.2. There is no difference in loss between a 500 μm, a 100 μm and a 50 μm long wire. We attribute the difference between these three measurements and the measurement for the 300 μm long wire (which is 0.6 dB) to a difference in grating coupler efficiency. However, from these measurements it is difficult to deduce a loss value in dB/cm because the wires are too short.

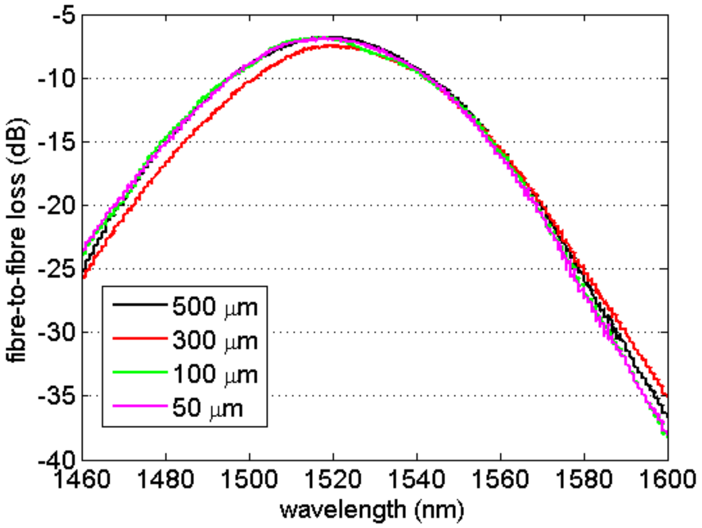

Figure 5.2: Fibre-to-fibre loss for wires with different lengths.

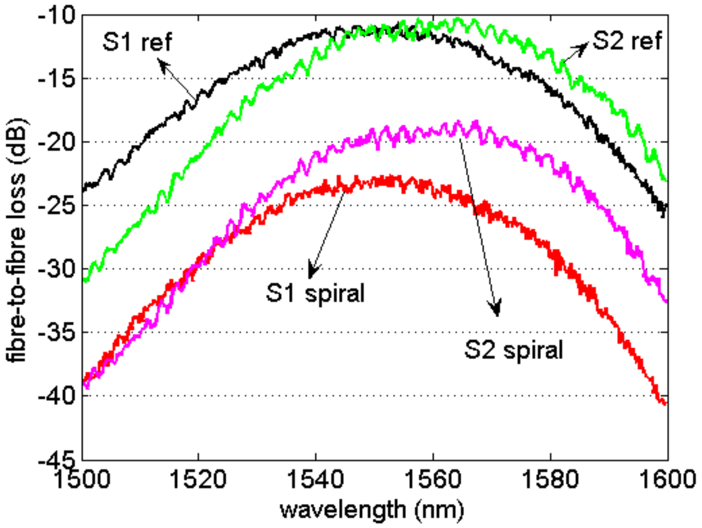

Figure 5.3: Fibre-to-fibre loss for long wires organised in a spiral as compared to reference structures with short 50μm long wire, on two samples S1 and S2.

Therefore, we have also fabricated wires with different lengths in the millimeter range. On two samples, the loss of a 5.6 mm long wire spiral (including 40 bends with radius of 10 μm) was compared to a reference structure with a short 50 μm wire. The excess loss due to the spiral is measured to be 11.7 dB (S1) and 8.3 dB (S2) (Figure 5.3). If we assume there is no excess loss introduced by the bends, this corresponds to a loss value of 20.9 dB/cm and 14.8 dB/cm respectively. These values give an upper limit of the propagation loss, since we have no information about radiation losses in the bend. Wires with longer lengths had defects after e-beam lithography and etching, resulting in low transmission. Therefore, they could not be used for determining a more precise loss value.

The loss of these InP membrane photonic wires is high as compared to state-of-the-art silicon photonic wires but not unacceptable for a first generation. Improvements on e-beam lithography and etching will result in significant decrease of the propagation loss.

5.2.2 Ring resonator notch filter

In the same run we have fabricated ring resonator based notch filters, as shown in Figure 5.4a. For small enough gaps between bus waveguide and bent waveguide light can couple between both. For specific wavelengths a resonance occurs due to constructive interference. In the case of a lossy filter, a drop in the transmission spectrum is then seen. A detailed study of ring resonator based filters can be found in [90].

The measured transmission spectrum for a ring resonator notch filter with radius of 4 μm and a fabricated gap of 150 nm is shown in Figure 5.4b, revealing a free spectral range (FSR) of 28.2 nm. A zoom of the resonance around λ=1603.5 nm is shown in Figure 5.5a. The extinction ratio is 16 dB and the loaded Q-factor, defined as f_0/FWHM [91] with f_0 the central frequency and FWHM the full width half maximum, is then 5830. We have fitted the measured transmission curve to the theoretical curve but due to the asymmetric nature of the latter, the fitting is not perfect. We obtain a fitted roundtrip loss in the ring of 0.13 dB and a coupling of 2.3%.

The asymmetric form of the curve indicates non-linear effects, similar to the behaviour of SOI ring resonators [92, 93]. Therefore, we have measured the transmission spectrum of the ring resonator structure for increasing input power of the tunable laser. The result is shown in Figure 5.5b. For the lowest input powers, the resonance wavelength

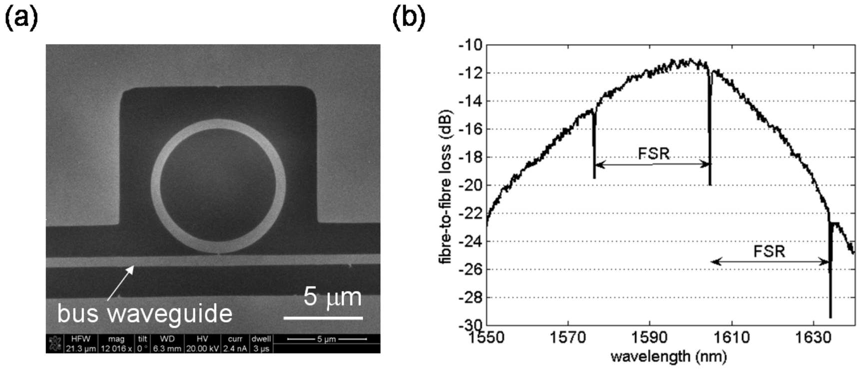

Figure 5.4: Ring resonator notch filter. (a) SEM picture. (b) Fibre-to-fibre transmission spectrum.

is slightly blue shifted as the input power is increased. For higher input powers, a wavelength red shift and bistability occurs. This can be explained as follows. Due to two photon absorption free carriers are generated, resulting in additional absorption (free carrier absorption) and an associated negative refractive index change due to free carrier dispersion. Recombination of these carriers results in heating and a positive thermal refractive index change. For the lower input powers, the free carrier dispersion effect is dominant, resulting in a blue shift of the resonance. For higher input powers, the thermal effects take over, resulting in a wavelength red shift and eventually bistability. For the SOI ring resonators in [93], thermal effects are dominant for all input powers and only a red shift of the resonance is observed. In [94], where III-V material is bonded onto SOI racetrack resonators, the blue shift due to free carrier dispersion is also observed.

5.2.3 MMI 3 dB splitter

In order to split the amount of incoming light into two equal paths, a 1x2 multi-mode interference (MMI) device can be used. Its operation is based on destructive and constructive interference between different modes in a multimode waveguide, resulting in self-imaging [95]. The input field profile is reproduced in single or multiple images at periodic lengths along the multimode waveguide.

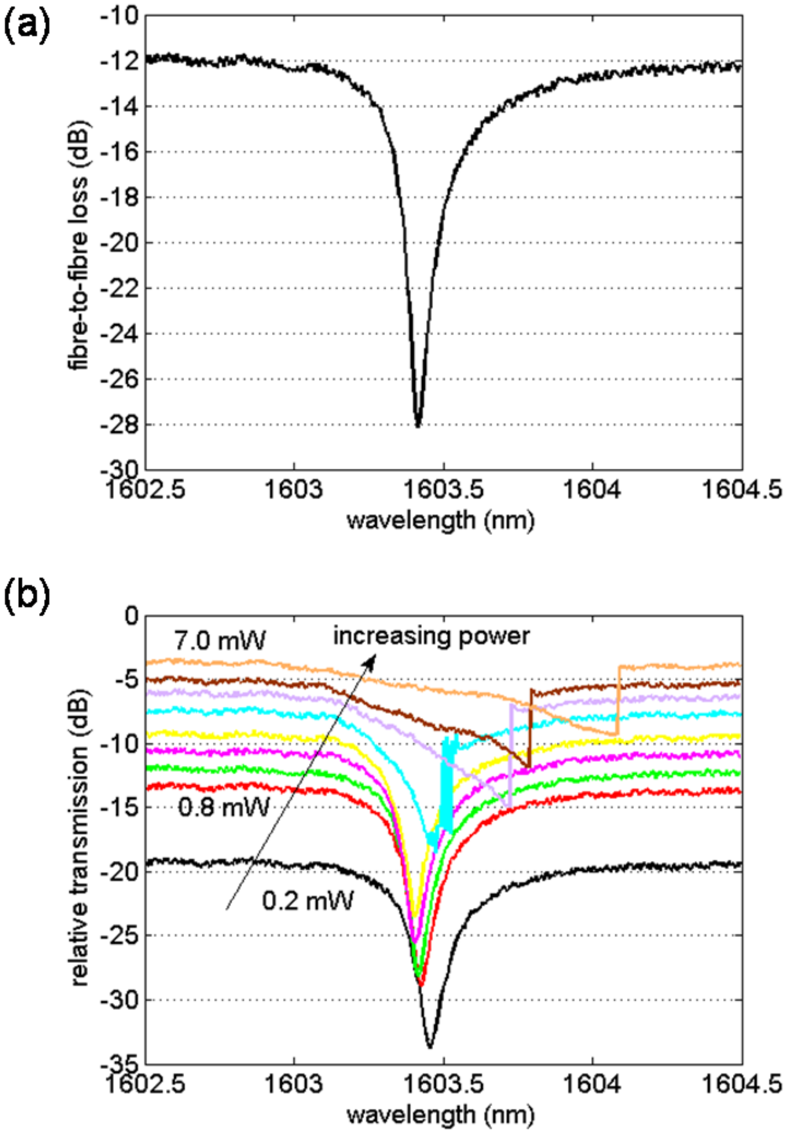

Figure 5.5: Ring resonator notch filter resonance. (a) Zoom of the resonance around λ=1603.5 nm . (b) Resonance for increasing input powers, resulting in bistability.

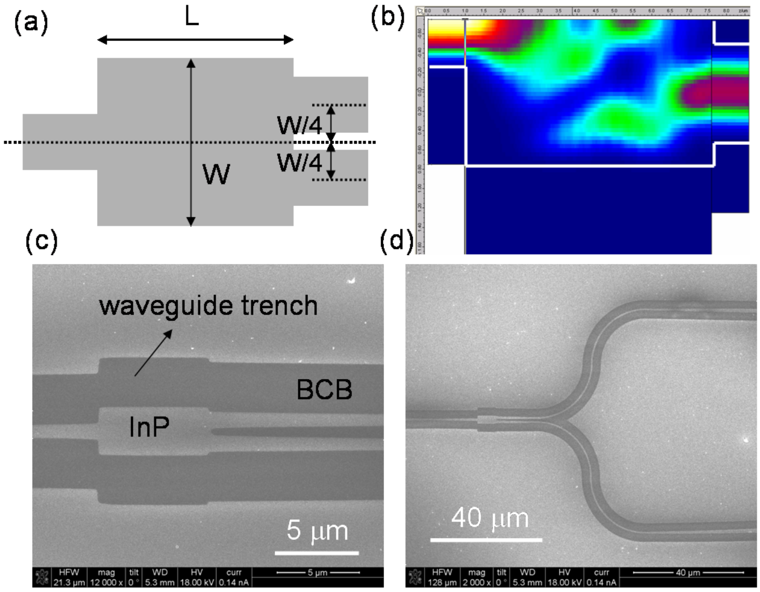

Figure 5.6: MMI 3dB-splitter. (a) Configuration. (b) Simulation result. Only half of the structure is simulated, based on symmetry. (c-d) SEM pictures after bonding.

Design

The design is done with FIMMWAVE [96], a commercially available fully vectorial mode solver, for a 200 nm BCB bonded InP membrane. A top view of the structure is shown in Figure 5.6a. The width W of the central multimode waveguide is chosen to be 3 μm. The input and output waveguides are 1 μm wide in order to minimise insertion losses. The input waveguide is placed in the middle of the central section, the output waveguides are placed at positions +W/4 and -W/4. With these parameters the optimal length of the central section is calculated to be L= 6.87 μm. A simulation result is shown in Figure 5.6b, where we simulate half the structure (based on symmetry). The simulated loss of the structure is 0.15 dB. SEM pictures of a device after bonding are shown in Figure 5.6c-d.

Characterisation

The characterisation procedure is as follows. First, the transmission through a reference waveguide is measured using third generation gra-

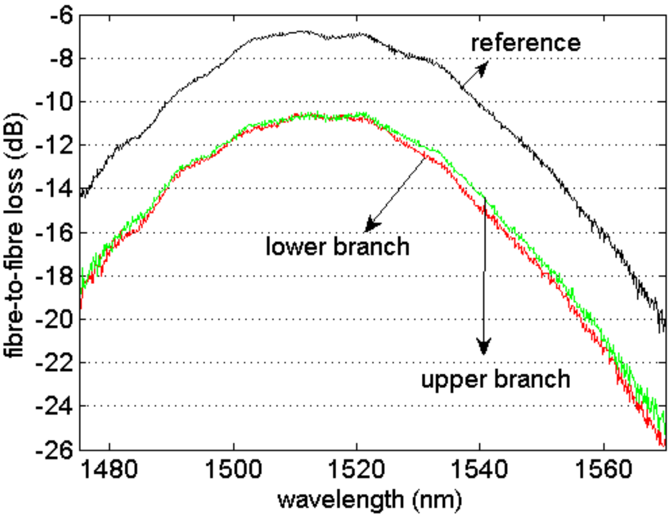

Figure 5.7: Characterisation of an MMI 3dB-splitter.

tings. Then, both outputs of the splitter are measured separately, for the same input coupling conditions. Both outputs show 3.6 dB lower transmission than the reference waveguide transmission. Hence, the measurement indicates a loss of the MMI splitter of 0.6 dB.

5.3 Photonic crystal based devices

5.3.1 Grating coupled photonic crystal demultiplexer

In the framework of the IST-FUNFOX project, we have implemented a grating coupled membrane version of the photonic crystal demultiplexer[2] described in [97, 98, 99] for substrate type InP/InGaAsP heterostructures. The demultiplexer is aimed at application in coarse WDM networks. The thickness of the membrane is 300 nm in this case.

Design

The operation principle of the demultiplexer (TAMIS) is the resonant intermodal coupling that occurs in multimode PhC waveguides at ministopbands (MSB) [100]. The design of the multiplexer is carried out at

---

[2] The demultiplexer received the name "TAMIS", French for "sieve". Wavelengths are "sieved" out a photonic crystal waveguide.

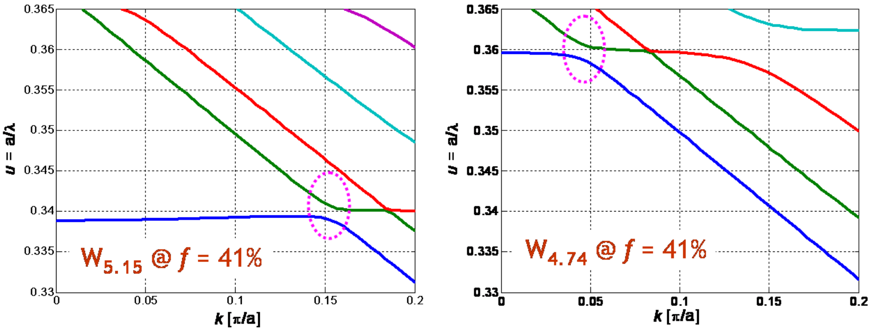

Figure 5.8: Band diagram of different W_N PhC waveguides, where the physical waveguide width= $(N+1)a\sqrt{\frac{3}{2}}$, a=PhC period (From Institut d'Optique, Palaiseau). MSB are located at the indicated anticrossings.

Institut d'Optique, Palaiseau, France. The basis of the design is a symmetric PhC W_5 waveguide (i.e. a waveguide formed by removing 5 rows of PhC holes). Figure 5.8 shows a band structure along ΓK of the PhC waveguide for two different waveguide widths around the reference W_5 width. The MSB is located at the indicated anticrossings. These are locations where the first order Bragg diffraction condition is satisfied. Mode coupling occurs provided that the mode parity is also satisfied. For symmetric waveguides, coupling is allowed between modes of identical parity. This way, the optical mode is converted into a higher-order mode and since this higher order mode penetrates deeper into the photonic crystal walls, it can be directionally extracted through a thinned PhC lateral cladding. The position of the MSB changes with the PhC waveguide width and demultiplexing operation is obtained by controlling the width of the local PhC guide to the MSB central frequency. A section length of $\sim 30\ \mu$m is enough for good extraction. An FDTD simulation result, showing lateral extraction of the higher order mode, is shown in Figure 5.9.

Characterisation

We have fabricated a TAMIS based on W_5 PhC waveguides with input fibre grating couplers in a 300 nm BCB bonded InP membrane. The TAMIS consists of different PhC sections with fixed (but different) width. The PhC period a=540 nm and the filling factor is 41%. Pictures of the device, prior to bonding and after bonding, are shown in Figure

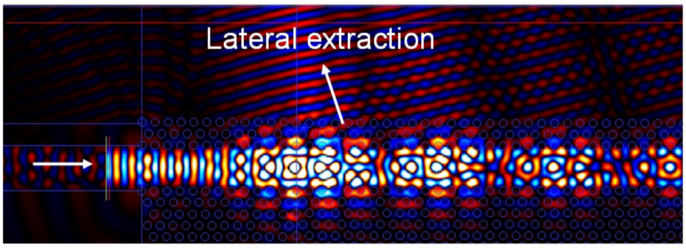

Figure 5.9: FDTD simulation of the PhC demultiplexer showing lateral extraction of the higher order mode (From Institut d'Optique, Palaiseau).

5.10. E-beam lithography is performed at University of St. Andrews, other processing steps at INTEC. The sample is etched with a two-step etch process: the TAMIS has a full membrane etch, while the gratings and waveguides have a shallow etch of 90 nm. After bonding the BCB is removed from the PhC holes using ICP-RIE etching.

For the characterisation, light from a tunable laser is coupled into a waveguide using a grating coupler. This waveguide feeds the TAMIS, where the different wavelengths are laterally extracted into broad channel waveguides. The light from the output channels is collected at a cleaved facet using an objective lens. The measurement setup is shown in Figure 5.11.

The TAMIS response is shown in Figure 5.12. The spectra are normalised to the grating coupler spectrum (i.e. we have removed the wavelength dependence of the grating coupler). We obtain a uniform channel spacing of 10 nm, as designed. The crosstalk between adjacent CWDM channels, whose spacing is 20 nm, is 8 dB. Through finetuning of the size and number of holes of the PhC cladding through which the signal is extracted, the MSB transfer function can be engineered which will result in lower crosstalk values[3]. From the through signal, the dropping of wavelengths can be clearly seen. One broad dip, rather than discrete dips is another indication of the high crosstalk.

5.4 Integration of waveguide detectors

Besides passive functionality of which examples have been given in the previous sections, active functions like light generation, amplification or detection need to be implemented. As a first step we have integrated

---

[3] We have implemented new designs in a new SOI fabrication run. Results were not available at the time of writing this thesis.

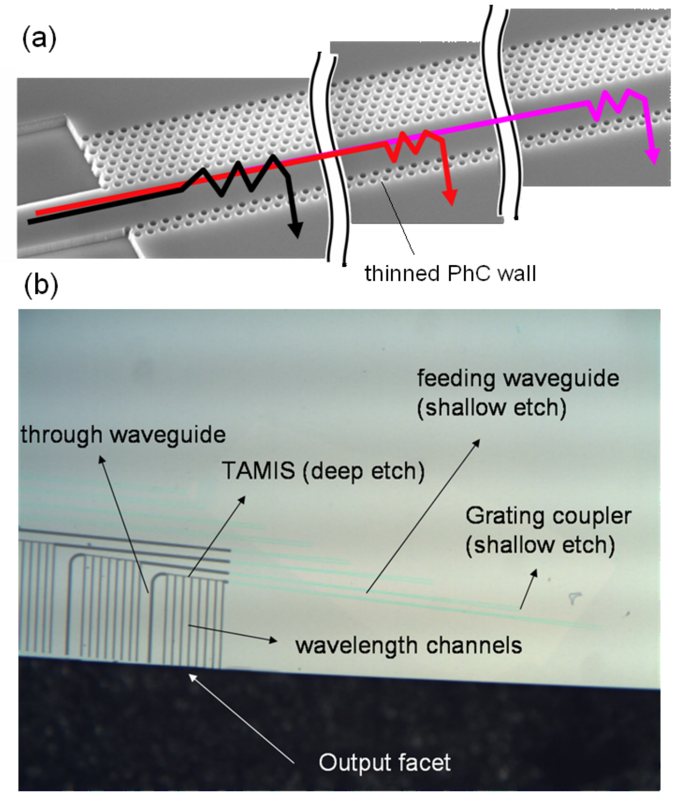

Figure 5.10: (a) Operating principle of the TAMIS (SEM pictures prior to bonding). (b) Sample layout after bonding.

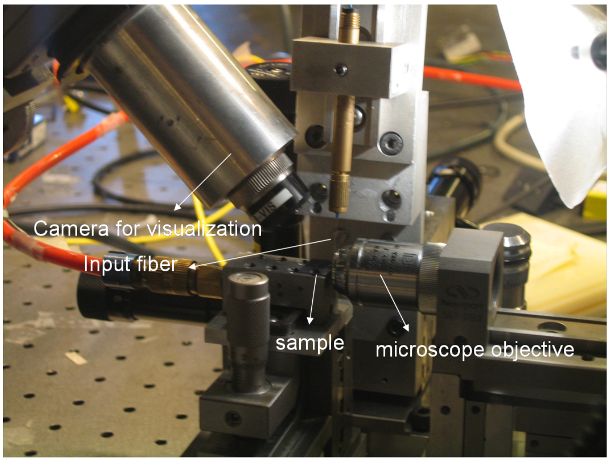

Figure 5.11: Measurement setup for characterisation of the TAMIS.

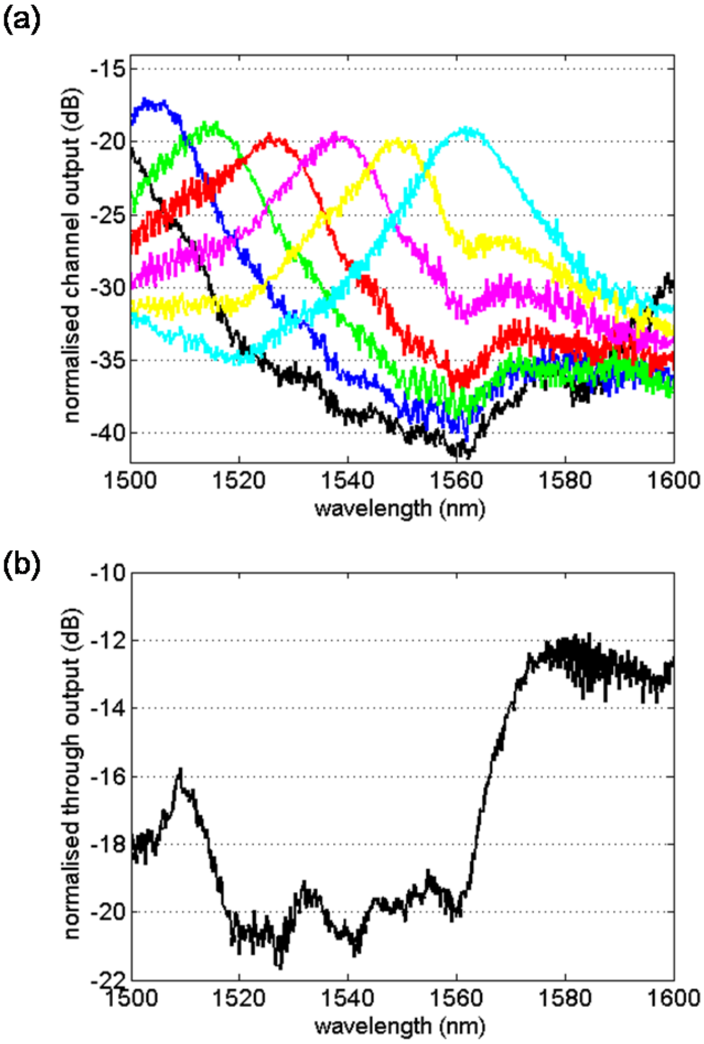

Figure 5.12: Response of a TAMIS. (a) channel outputs. (b) through signal.

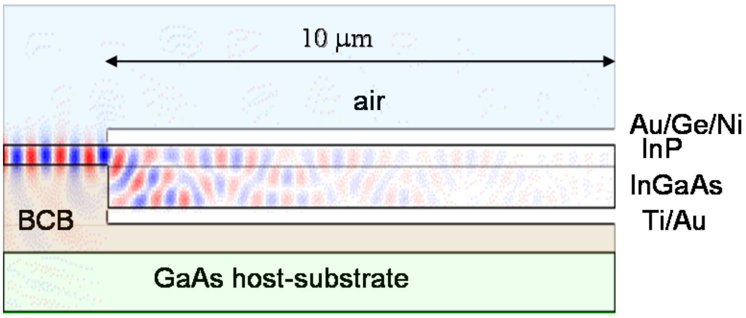

Figure 5.13: Detector layout and simulation result.

photodetectors onto the InP membrane platform. Most widely used detectors are p-i-n photodiodes and metal-semiconductor-metal (MSM) detectors. For waveguide detectors, the light has to be coupled from a non-absorbing waveguide layer to an absorbing detector layer. By applying an electrical field, carriers generated by the absorbed light are swept to metal electrodes creating a photocurrent. Important aspects in designing waveguide detectors are given in [101].

5.4.1 Design

Waveguide-detector coupling can be obtained either by butt-coupling or vertical coupling. Since butt-coupling requires regrowth, the vertical coupling approach is more elegant for our application. We have chosen to implement a p-i-n type detector[4] of which the layout is shown in Figure 5.13 together with a CAMFR simulation result. The light in an InP membrane waveguide is refractively coupled to an underlying absorbing (intrinsic) InGaAs layer. The InP membrane is slightly n-doped and has an n-type Au/Ge/Ni contact. At the bottom side, a Ti/Au p-contact is applied on a heavily p-doped InGaAs layer.

For this type of structure, absorption loss in the metal contacts plays an important role. As can be seen in Figure 5.13, the light bounces back and forth in the InP membrane layer and the InGaAs absorbing layer. For a thin InGaAs layer, the light needs several roundtrips before being totally absorbed, incurring competing absorption losses at the metal contact. If the InGaAs layer is thick enough, light can be absorbed in one roundtrip, minimising loss at the metal contacts. The thickness has

---

[4] MSM detectors require InAlAs layers, which could not be grown by the group supplying the epitaxy.

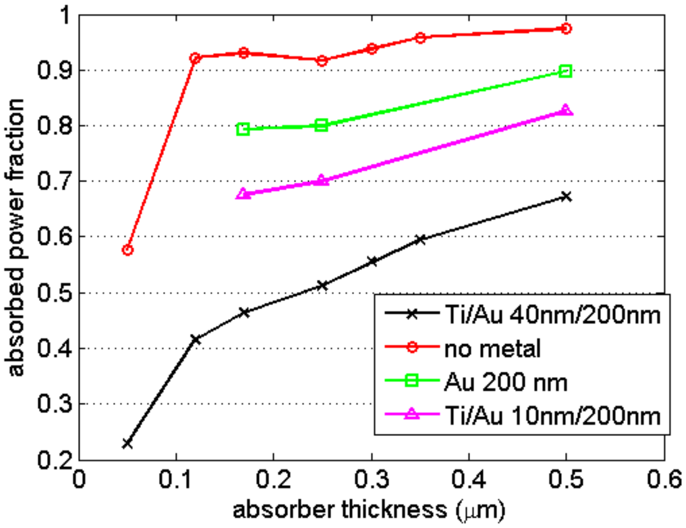

Figure 5.14: Influence of metal bottom contact on absorbed power in the InGaAs layer.

an important influence on the speed of the detector [101]. Making the absorber thicker increases the spacing between the electrodes and decreases the detector capacitance, which has a positive influence on the detector speed. However, it also increases the time for carriers to reach the electrodes (carrier transit time), which has a negative influence on the detector speed. As a result, there is a capacitance/transit time trade off.

The absorbed power is calculated from the CAMFR simulation from Figure 5.13 with [102]:

$$P_{abs} = -2k\sqrt{\frac{\epsilon_0}{\mu_0}} \int \int n_r n_i |E|^2 dx dz \tag{5.1}$$

with k=$\frac{2\pi}{\lambda_0}$, n$_r$ and n$_i$ the real and imaginary part of the refractive index of the absorbing material, and $|E|$ the absolute value of the electric field in the semiconductor. In Figure 5.14 we show the influence of the metal contacts. The absorbed power in the InGaAs layer is shown as a function of absorber thickness, for different compositions of the bottom Ti/Au contact and a detector length of 10 μm. The standard p-contact at INTEC is a Ti/Au layer with thickness 20nm/200 nm. For this composition there is substantial absorption in the metal, occurring mainly in the Ti layer. By decreasing the thickness of Ti in the Ti/Au contact, this metal absorption can be reduced. The Ti layer serves as an adhesion layer between the Au layer and the semiconductor. An InGaAs absorber thickness of 500 nm in combination with a 10nm/200nm Ti/Au contact is a reasonable compromise between efficiency and speed.

5.4.2 Detector characterisation

The devices are fabricated using the integration scheme described in section 3.4.3, on a 300 nm InP membrane. For detector characterisation, light from a tunable laser is coupled into a membrane waveguide using a grating coupler (Figure 5.15a, picture prior to bonding so the detector is at the top), and coupled to the underlying detector (Figure 5.15b, picture after bonding).

The I-V curves for a 12 μm x 10 μm detector are shown in Figure 5.16a for different values of the input power at the tunable laser. We observe a linear behaviour as a function of input power. The dark current of the detector is 4 nA at 0.5 V reverse bias. After taking into account the loss in the setup we are able to establish an external responsivity for the fibre-to detector system of 0.40 A/W at 1580 nm wavelength[5]. The grating coupler spectrum measured with the integrated detector is shown in Figure 5.16b. In order to check that the detector response is not wavelength dependent, we have added a fibre-to-fibre transmission measurement using grating couplers and a connecting waveguide. Both curves nearly coincide, and slight deviations are attributed to a difference in fabricated grating couplers.

The speed (or electrical bandwidth) of the detector could not be measured on this first generation detectors. The reason is the fact that the contact pad layout was not adapted for measuring with RF-probes, and only DC-probes could be used. In a second generation detectors, used in a coherent receiver chip, we have changed the contact layout and results on detector bandwidth will be given in Chapter 7.

5.4.3 Photonic crystal demultiplexer with integrated detectors

The same integration scheme is used to integrate a grating coupled membrane TAMIS with photodetectors. The device layout is shown in Figure 5.17. Light from a tunable laser is coupled into a membrane

---

[5] We do not have figures for the grating coupler efficiency on this sample. However, we estimate the coupling efficiency to be 33-40%, based on parameters extracted from a cross-section. From this, a detector efficiency of 78-95% is deduced.

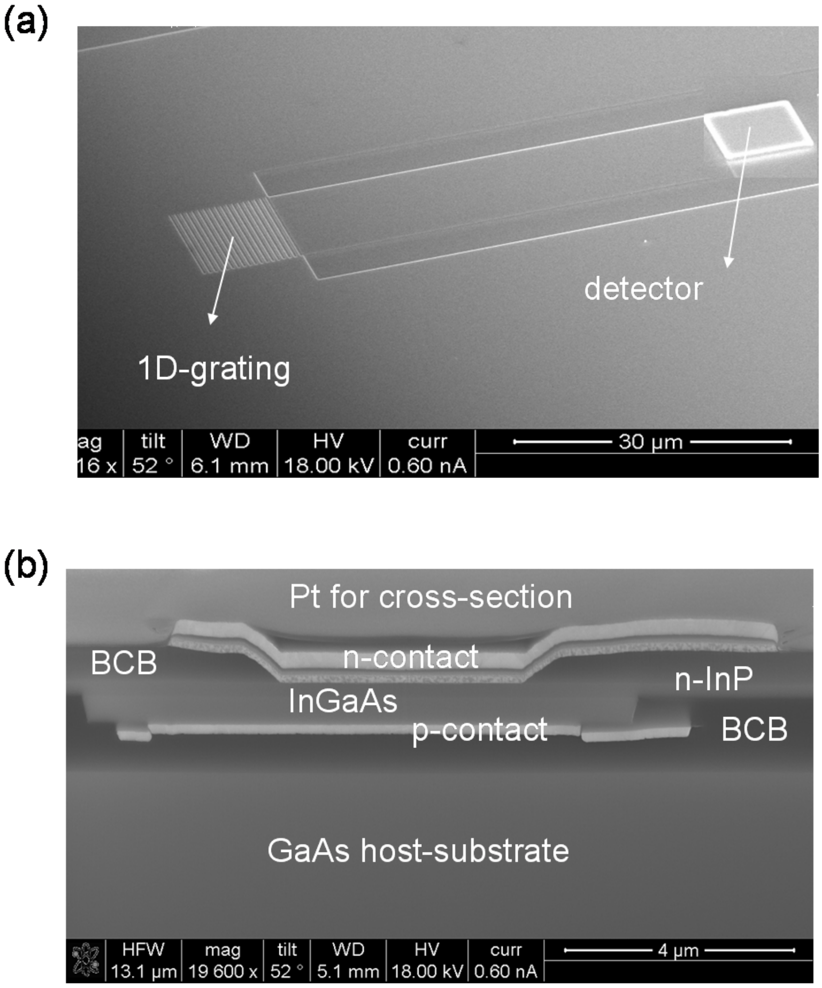

Figure 5.15: Pictures of fabricated detectors. (a) Coupling configuration: light is coupled to a waveguide using a grating coupler and then refractively to a detector. Picture before bonding, so the detector is still at the top side. (b) SEM picture of a detector cross-section made by FIB.

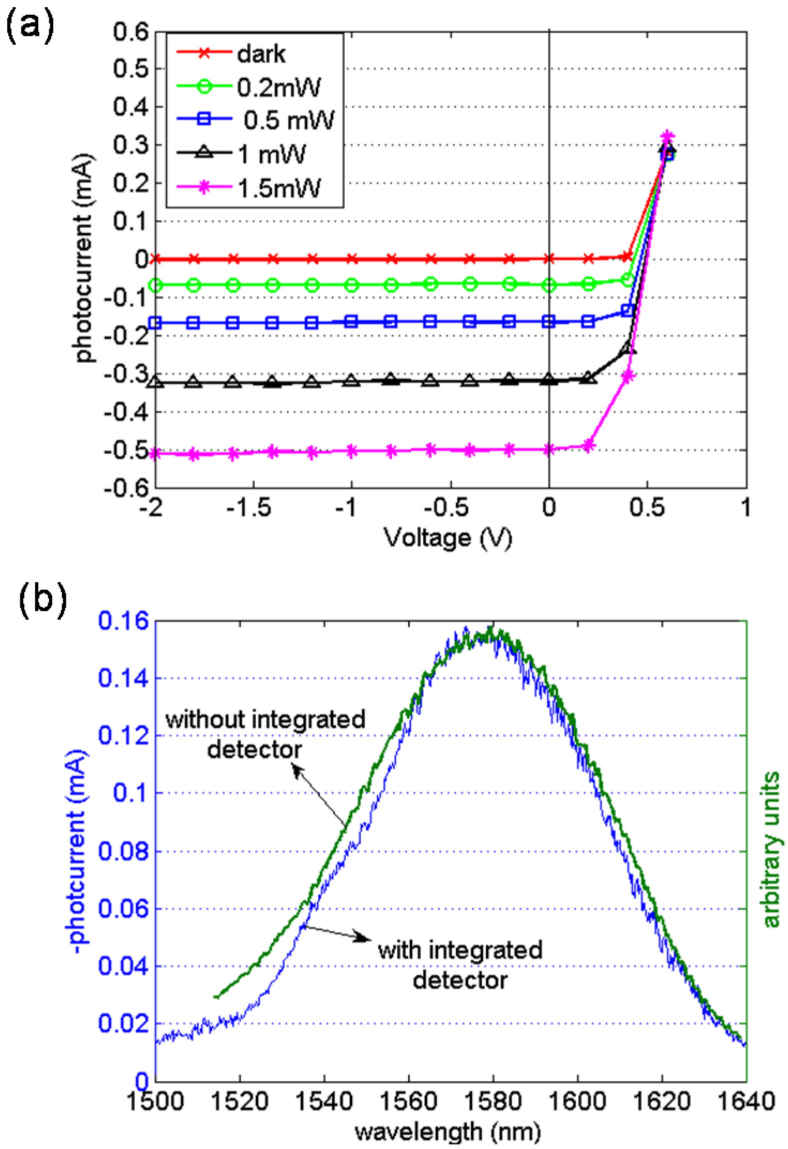

Figure 5.16: Detector characterisation. (a) I-V curves for different input powers. (b) Grating coupler spectrum measured with the integrated detector. For reference, a fibre-to-fibre transmission measurement is also included.

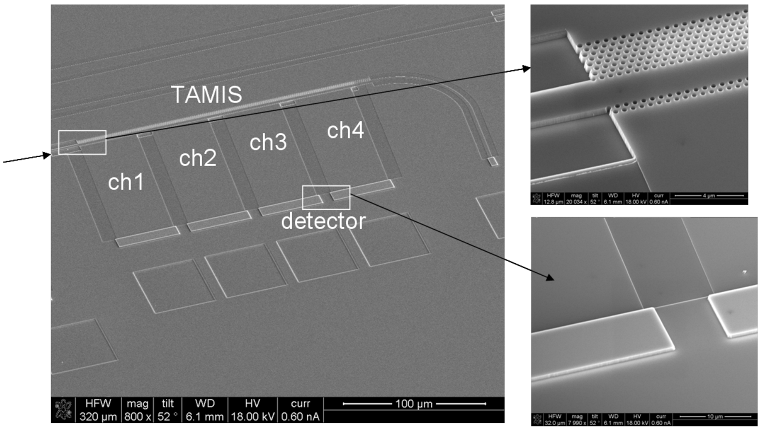

Figure 5.17: Layout of the InP membrane TAMIS with integrated photodetectors, pictures prior to bonding.

waveguide using a grating coupler and then fed into the PhC demultiplexer. The optical signal is extracted by 4 broad channels toward the integrated photodiodes and converted into photocurrent. The through signal goes to another integrated detector for reference. A very good correspondence is obtained between simulation (Figure 5.18a) and experiment (Figure 5.18b). The crosstalk between 20 nm spaced channels is around 5-6 dB. There might be some electrical crosstalk, since the crosstalk on all-optical devices is slightly better at around 8 dB. The electrical crosstalk could be eliminated by using guard rings or by removing semiconductor material around the detectors.

5.5 Conclusions

In this chapter we have integrated functional devices onto an InP membrane platform. Light was coupled to the devices using the grating couplers described in previous chapters. The loss of single-mode photonic wire waveguides is in the range of 15 dB/cm. Satisfying performance has been obtained for very compact ring resonators and MMI 3 dB splitters. Photonic crystal demultiplexers showed high cross-talk values, which will be improved in the future through new designs made at Institut d'Optique. P-i-n photodiodes were successfully integrated onto BCB bonded InP membrane and showed an external responsivity (fibre-to-detector) of 0.4 A/W. They were finally used to characterise a PhC demultiplexer.

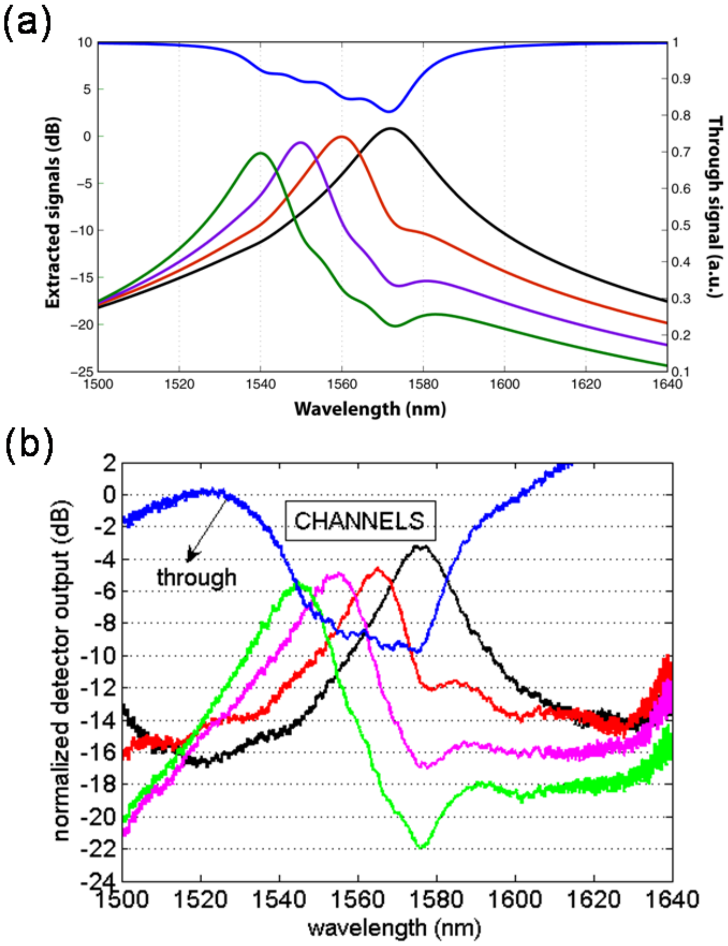

Figure 5.18: (a) Simulation of the TAMIS response, based on Coupled Mode Theory (performed at Institut d'Optique). (b) Measured TAMIS response with integrated detectors, normalised to the grating coupler spectrum.

Chapter 6

Polarisation diversity circuits

In this chapter we deal with the polarisation sensitivity of nanophotonic devices by implementing polarisation diversity using 2D grating couplers. The first part concentrates on the performance of the 2D couplers, while the last part describes more complex polarisation diversity integrated circuits.

6.1 Polarisation diversity 2D grating couplers

6.1.1 Principle

The 1D grating couplers from previous chapters are very polarisation selective. The reason is the large waveguide birefringence in high index contrast material systems. The effective index is substantially different for TE and TM polarisation and as a consequence a 1D grating coupler can only be designed for one polarisation. The orthogonal polarisation will be coupled at a completely different angle. The extinction ratio between both polarisations is 20 dB for a 1D grating coupler. However, this high polarisation selectivity can be used for implementing polarisation diversity.

The configuration for polarisation diversity using grating couplers is shown in Figure 6.1a. It consists of a 2D grating and two orthogonal waveguides. The 2D grating can in first approximation be described as a superposition of two orthogonal polarisation selective 1D gratings. As a result, both orthogonal polarisations are split and couple to their own (orthogonal) waveguide. In the waveguides the polarisation is

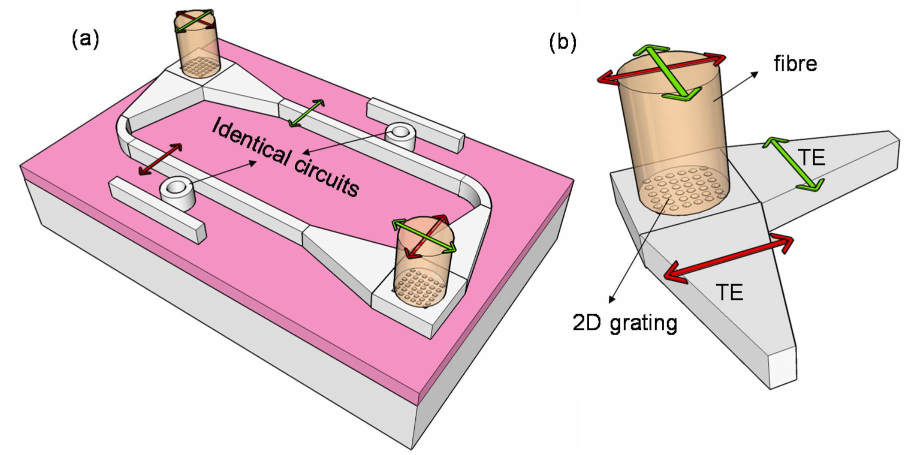

Figure 6.1: (a) Polarisation diversity using 2D grating couplers. (b) 2D grating used as a polarisation splitter.

TE (Figure 6.1b). Both arms then feed an identical polarisation sensitive nanophotonic device. At the output, they are recombined using another 2D grating.

6.1.2 Near vertical coupling

Vertical coupling results in large second order reflection. In order to avoid these reflections, angled coupling can be used which has important consequences on the coupling configuration. In order to preserve the symmetry the fibre must be tilted along the bisection line of the grating. However, this tilt reduces coupling to the fundamental waveguide mode due to a phase mismatch. In order to compensate for this mismatch, the waveguides (or the grating) have to be rotated slightly.

A theoretical description of these concepts was given in [39], while we have verified this experimentally for BCB bonded InP membrane couplers and SOI focusing grating couplers. We will summarise the important equations here. An instructive explanation can be given by using a k-vector diagram [39], which is shown in Figure 6.2. The relation

$$\overrightarrow{k}_{wg} = \overrightarrow{k}_{in,proj} + \overrightarrow{K} \tag{6.1}$$

with $\overrightarrow{k}_{wg}$ the wave vector of the optical waveguide mode, $\overrightarrow{k}_{in,proj}$ the projected wave vector of the incident fibre mode and $\overrightarrow{K}$ the reciprocal

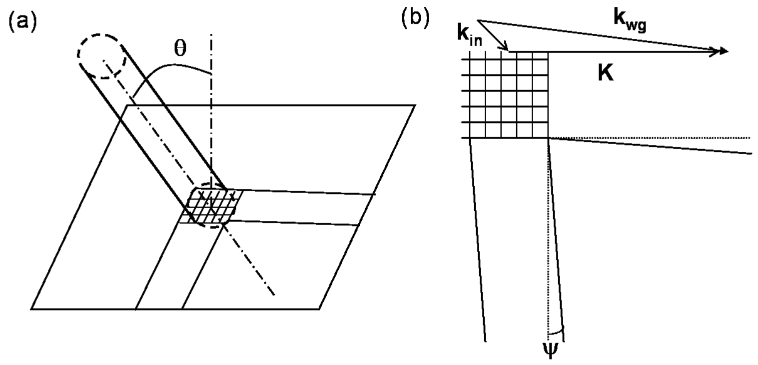

Figure 6.2: (a) 2D grating couplers with angled coupling and rotated waveguides. (b) K-vector diagram. From [39].

lattice vector of the grating, results in the following equations

$$\frac{2\pi}{\lambda} n_{eff} \sin\psi = \frac{2\pi}{\lambda} \sin\theta \cos\frac{\pi}{4} \tag{6.2}$$

$$\frac{2\pi}{\lambda} n_{eff} \cos\psi = \frac{2\pi}{\lambda} \sin\theta \cos\frac{\pi}{4} + \frac{2\pi}{\Lambda} \tag{6.3}$$

with θ the tilt angle of the optical fibre (Fig. 6.2a) and ψ the angle of the waveguide (Fig. 6.2b). For a given angle θ of the fibre, (6.2) can be used to calculate the waveguide angle ψ. And for these values θ and ψ, (6.3) can be used to calculate the grating period. The effective index n_{eff} is the effective index of the waveguide mode in the case of a weak grating. For the high index contrast gratings in this work this is an approximation. However, we have used these equations and will verify the outcome experimentally.

Another consequence of near vertical coupling is a wavelength dependence of the Polarisation Dependent Loss (PDL). The reason is that both orthogonal polarisations along the diagonal of the grating do not experience the same grating, as one polarisation is tilted out of a plane parallel to the grating (Figure 6.3). As a result, there is a wavelength shift between the coupling efficiency curves for both polarisations. In addition, the optimal waveguide angle is not identical for both polarisations. The combination of both effects yields the wavelength dependence of the PDL.

Preliminary simulations have been carried out using the 3D FDTD software MEEP [103] on a cluster with 60 nodes having 1 GB of me-

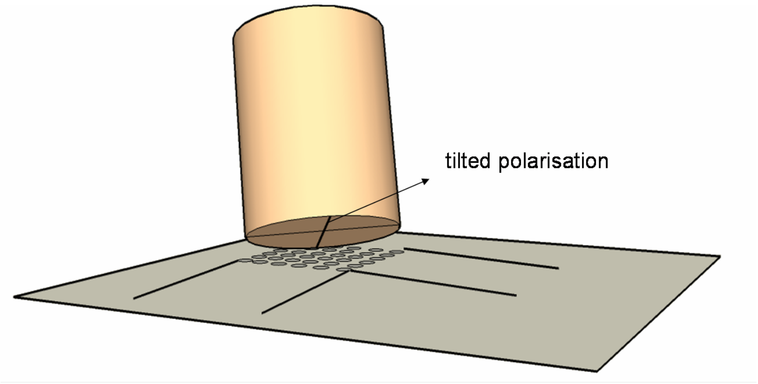

Figure 6.3: Near vertical coupling configuration. Both orthogonal polarisations along the diagonal of the grating experience different coupling.

mory each[1]. The resolution of the simulation was not yet high enough (minimum grid step of 30 nm) to achieve a high accuracy, but the predicted behaviour is obtained. The coupling from a Gaussian beam to an SOI waveguide is calculated for two orthogonal input polarisations along the diagonal of the grating as shown in Figure 6.4a. The results are shown in Figure 6.4b. The wavelength shift between both curves will result in a wavelength dependence of the PDL. We will verify this experimentally in the following sections.

6.2 2D grating couplers in InP membrane

We have applied the InP membrane technology first developed for 1D grating couplers to the 2D polarisation diversity grating couplers. A gold mirror is used to increase the coupling efficiency by avoiding radiation toward the substrate.

6.2.1 Design

In order to achieve sufficient resolution for the simulation, we have reduced the structure to one row of holes (20 periods) in the lateral direction for obtaining the grating parameters (Figure 6.5). We have performed 3D FDTD simulations on this reduced configuration and modelled the optical power that is radiated upwards (Figure 6.6a). From

---

[1] This cluster was only available at the end of the PhD and simulations are still in “developing phase”.

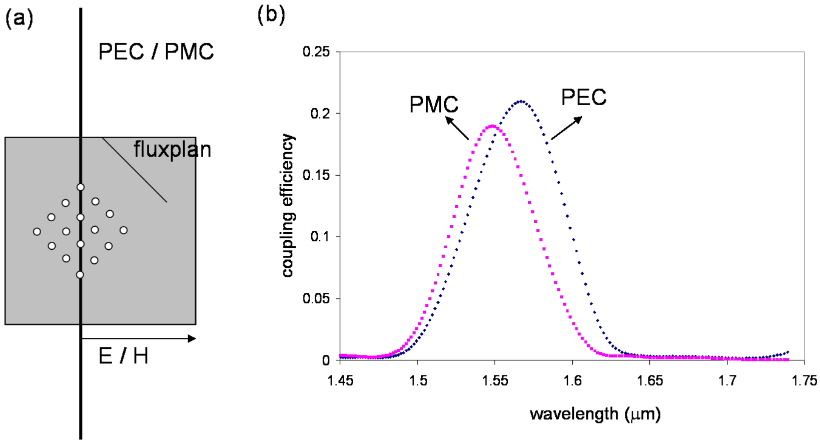

Figure 6.4: 3D FDTD simulations for an SOI 2D grating coupler and near vertical coupling, performed by G. Roelkens. (a) Simulation configuration exploiting symmetry (PEC=perfect electric conductor, PMC=perfect magnetic conductor). (b) Simulation results showing a wavelength shift in coupling efficiency curves for orthogonal polarisations along the grating diagonal.

this simulation, the leakage factor α is extracted and the etch depth and hole size is chosen to obtain the optimal α=0.13/μm (see section 2.3.3). The BCB buffer layer thickness is optimised for maximal upwards radiated power. These simulations result in a grating period of 640 nm, an etch depth of 100 nm, a hole diameter of 420 nm and an optimal BCB buffer layer (between grating and gold mirror) of 620 nm (Figure 6.6b).

Waveguide angle

(6.2) and (6.3) are used to calculate the required waveguide angle ψ when using angled coupling (θ=10°). For n$_{eff}$=2.73 (n$_{eff}$ of the waveguide) (6.2) results in ψ=2.57°. (6.3) then results in a period of 595 nm. The discrepancy with the simulated period of 640 nm is due to the fact that the equations assume weak gratings, which is not the case here.

6.2.2 Characterisation

Optimal waveguide angle

The layout of the fabricated sample is shown in Figure 6.7. Input and output gratings are placed at the intersection of two 12 μm wide nearly

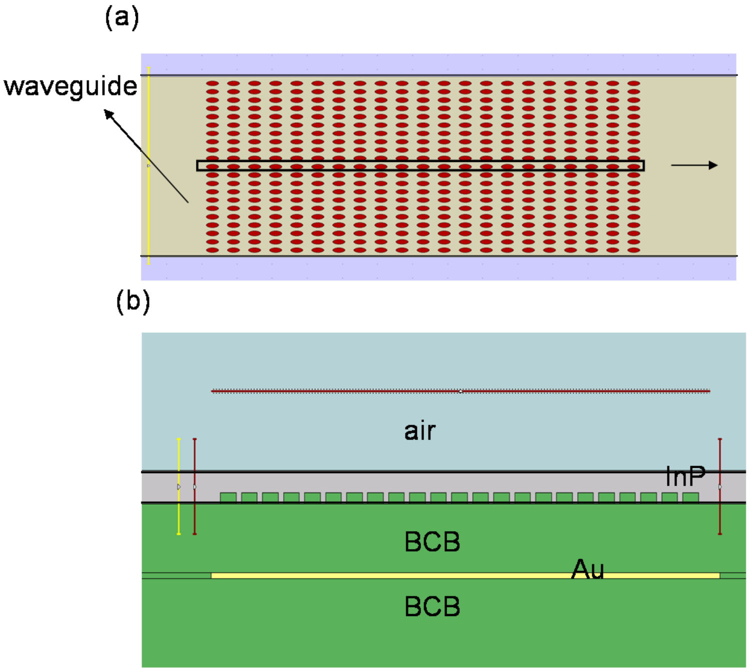

Figure 6.5: Simulation of 2D grating couplers. (a) Top view of the entire structure. For the simulation, the structure is reduced to one row of holes in the lateral direction. (b) Cross-section.

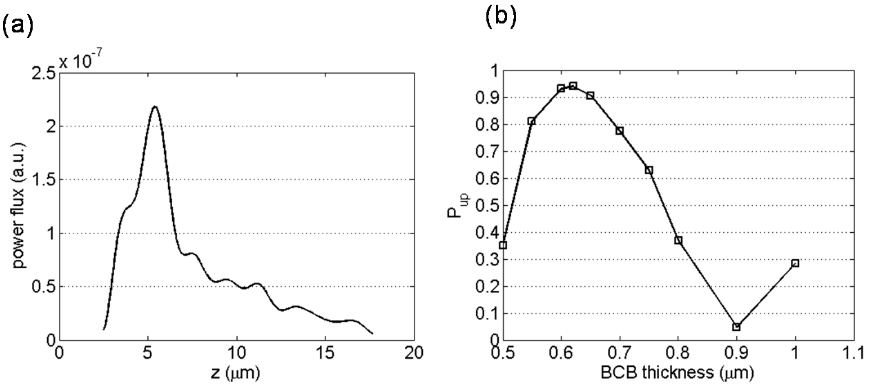

Figure 6.6: Design of 2D grating couplers using 3D FDTD on a reduced structure. (a) Radiated intensity profile from which the leakage factor α is deduced. (b) Determination of the optimal BCB buffer thickness.

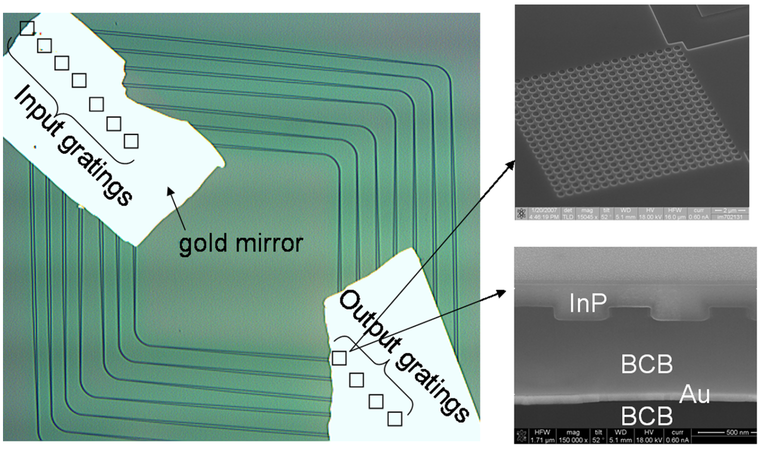

Figure 6.7: (Left) Microscope image of the sample before bonding (light hatched regions are gold covering the gratings. They will form the bottom mirror after bonding). Gratings are inside the rectangles. (Top right) Top SEM view of the grating before bonding. (Bottom right). Cross-section of a fabricated structure after bonding.

orthogonal waveguides. The wide waveguides are tapered adiabatically to single-mode bent waveguides (600 nm wide) in order to connect input and output. On the sample the waveguide angles are varied from ψ=2.0° to ψ=3.5° and the fibre-to-fibre transmission is measured. The input light for these measurements is linearly polarised, with the electric field along the diagonal of the 2D grating. For this polarisation the coupling efficiency to both waveguides is the same.

For waveguide angles ranging from ψ=2.3° to ψ=2.8° the transmission is maximum. These optimal waveguide angles are close to the designed (calculated) angle of ψ=2.57°. After taking into account losses in the waveguides and bends determined from reference structures, the experimental coupling efficiency of a single 2D grating coupler is determined to be 48%. For waveguide angles of 2.0° and 3.0° the transmission is 1.4 dB lower than the optimal case, while for an angle of 3.5° the transmission is 3 dB lower than the optimal case.

Polarisation Dependent Loss

In order to measure the Polarisation Dependent Loss the input polarisation is changed randomly over all polarisation states using polarisation control paddles (Lefevre loops) [104]. The fibre positions are optimised

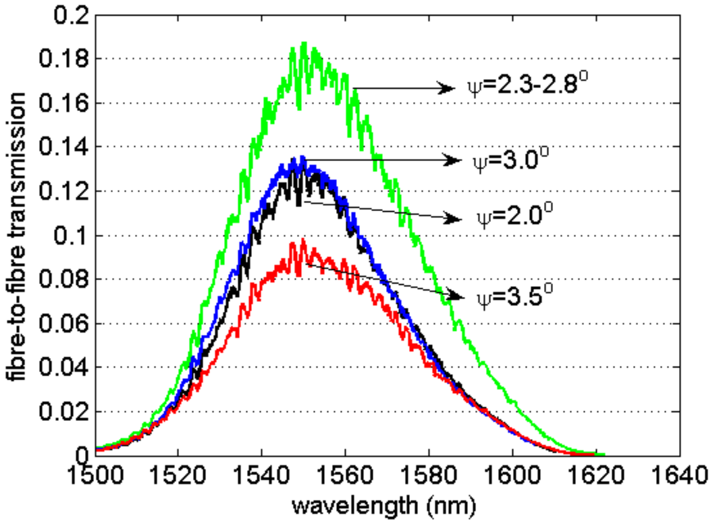

Figure 6.8: Influence of the waveguide angle.

for minimum Polarisation Dependent Loss (PDL) at the central wavelength of the grating coupler, resulting in a slightly lower coupling efficiency of 47%. The PDL is defined as the ratio between maximum and minimum transmission when varying the input polarisation over all states:

$$PDL(dB) = 10\log_{10}(\frac{T_{max}}{T_{min}}) \tag{6.4}$$

The PDL is measured to be 0.79 dB (Figure 6.9).

6.3 Focusing 2D grating couplers in SOI

For standard grating couplers a long adiabatic transition between wide waveguides and single-mode wires is required, compromising the integration density. We have shown for (polarisation selective) 1D gratings that this adiabatic transition can be omitted when using curved focusing gratings. In this section, we will extend the principle to 2D gratings in a polarisation diversity configuration. The layer structure that is used is SOI, but as usual the principles can be easily transferred to InP membrane.

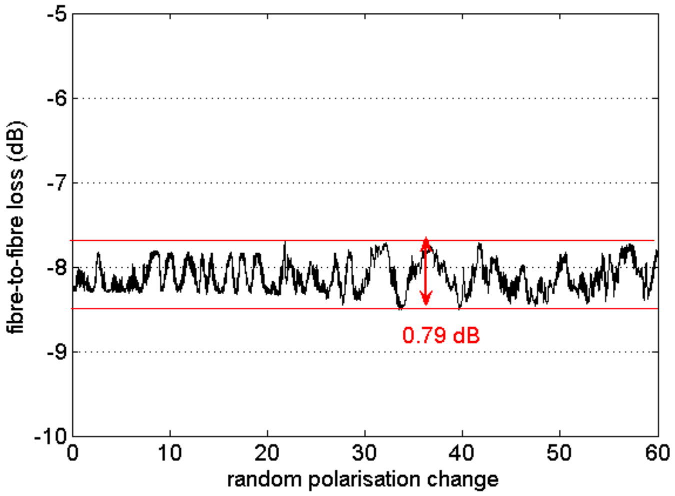

Figure 6.9: Measurement of the PDL.

6.3.1 Design

In analogy with standard 2D grating couplers, which can be considered as a superposition of two orthogonal standard 1D gratings, a focusing 2D grating coupler can be understood as a superposition of two orthogonal focusing gratings. We have made two different designs based on the design of a 1D focusing grating coupler for which the grating lines are obtained by solving (see section 2.4.2):

$$q\lambda_0 = n_{eff}\sqrt{y^2+z^2} - zn_t \sin\theta \tag{6.5}$$

with q an integer number for each grating line, θ the angle between the fibre and the chip surface normal, n_t the refractive index of the environment, λ_0 the vacuum wavelength and n_{eff} the effective index in the grating area. The right part of the equation calculates the phase difference between the focusing wave toward the wire and the input wave from the fibre.

Design 1 (θ=0°)

Here, we use θ=0° in (6.5) in which case the grating lines are concentric circles with the common center as the focal point. The 1D gratings are calculated in the same way as in section 2.4.2 depending on the configuration, now using the n_{eff} of the standard non focusing 2D grating

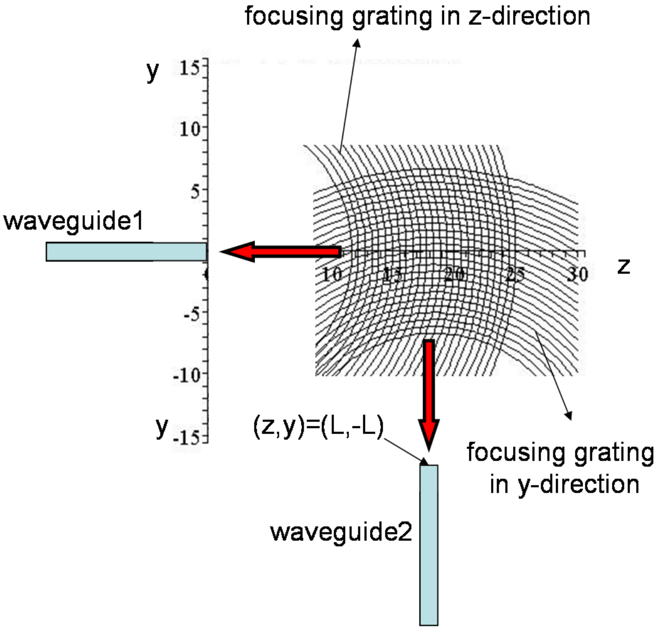

Figure 6.10: Overlay of two orthogonal focusing 1D grating couplers

obtained from the Bragg condition. The overlay of two orthogonal focusing gratings is shown in Figure 6.10. One grating focuses on the point with coordinates (z,y)=(0,0) and the other grating focuses on the point (z,y)=(L,-L). L is the distance from the focal point (z,y)=(0,0) to the center of the grating. The points of intersection of both gratings are calculated numerically. At these points a hole of 380 nm is placed, which is also used in non-focusing 2D gratings.

In practice, vertical coupling cannot be used as it induces large second order reflection. In order to avoid this, the fibre can still be tilted along the bisection of the grating lines. Then the waveguides will have to be rotated, as is the case for standard polarisation diversity 2D grating couplers.

Design 2 (θ=10°)

Here, we use θ=10° and modify the phase relation for the input wave for coupling at an angle along the bisection line of the grating. The output wave is still a spherical wave toward the photonic wire. The constructive interference condition for the grating lines of a 1D focusing

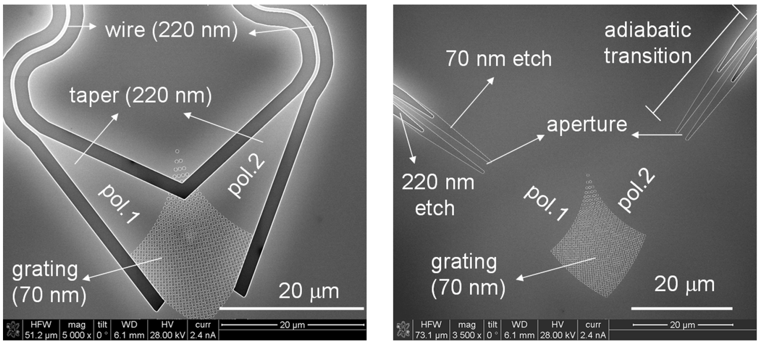

Figure 6.11: SEM pictures of focusing 2D grating couplers. (Left) Short taper configuration. (Right) Low contrast aperture configuration.

grating with the focal point at the origin becomes:

$$q\lambda_0 = n_{eff}\sqrt{y^2+z^2} - (y+z)n_t \sin\theta \sin\frac{\pi}{4} \tag{6.6}$$

Again we overlay two orthogonal focusing 1D gratings, one with the focal point at (z,y)=(0,0) and the other with the focal point at (z,y)=(L,-L). In this case, the waveguides do not need a rotation when using angled coupling since all phase relations are taken into account in the calculation of the grating.

The Matlab routines used for calculating the gratings for both designs are available in Appendix A.

6.3.2 Characterisation

Short taper vs. low contrast aperture

Design 2 is evaluated for the two configurations considered in 4.2.3, short taper and low contrast aperture (Figure 6.11). Figure 6.12 shows fibre-to-fibre transmission measurements where both input and output grating are focusing 2D gratings. We have calculated two different gratings with different focal distances corresponding with two low contrast aperture widths. The focal distance for a 2.0 μm aperture is 21.4 μm (q_{min}=36) and the focal distance for a 0.8 μm wide aperture is 11.9 μm (q_{min}=20). For both gratings we have also measured the performance for the short taper case. In that case, the taper length to the 500 nm photonic wire equals the above focal distances.

In all these measurements angled coupling in combination with orthogonal waveguides is used. For the grating with the largest focal

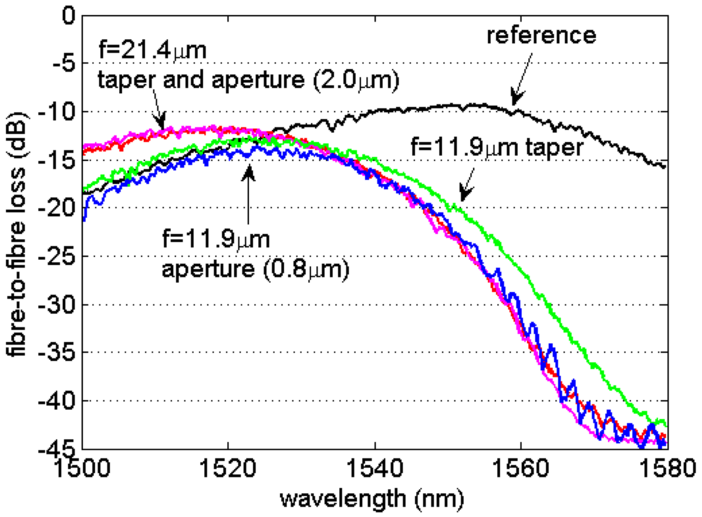

Figure 6.12: Fibre-to-fibre transmission measurements for different focusing gratings in short taper and low contrast aperture configuration. The reference curve is measured for a standard (non-focusing) 1D grating.

distance, the low contrast aperture (2.0 μm) and short taper configuration perform equally well. The measured fibre-to-fibre loss of 12 dB includes 0.8 dB propagation loss in the connecting photonic wire circuit. The coupling loss of a single grating is then 5.6 dB or a coupling efficiency of 27%. This is slightly better than standard 2D couplers without curved gratings having a coupling loss of 6.7 dB or a coupling efficiency of 21% [105]. For the grating with the smallest focal distance, the low contrast aperture (0.8 μm) configuration has 0.75-1 dB higher fibre-to-fibre loss (or 0.37-0.5 dB per coupler) than the short taper configuration. The reason is that the light cannot be focused to a spot as small as the aperture width (0.8 μm) resulting in excess loss, while in the short taper configuration, the light is confined and "guided" towards the photonic wire by the taper. The ripple on the transmission curves is higher in the low contrast aperture case, especially for the small aperture, which indicates that there are reflections at the interface. The grating with the shortest focal distance in short taper configuration has 0.5 dB excess loss per coupler as compared to the grating with longest focal distance, indicating that the "guiding" taper is too short in the first case.

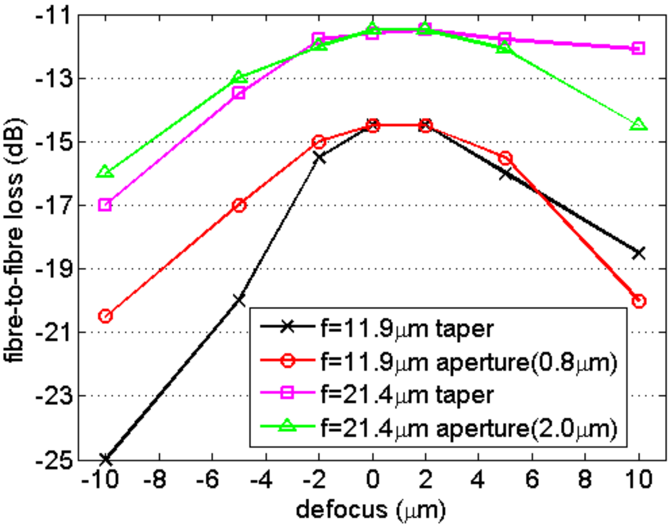

Figure 6.13: Influence of defocus for 2D focusing grating couplers.

Focal distance

We have investigated the tolerances on focal distance by varying the distance from grating to aperture or photonic wire around the value used in the calculations. The gratings to be considered are based on design 2 with focal length of 21.4 μm and 11.9 μm, both in low contrast aperture and short taper configuration. We have measured the transmission for a defocus of -10, -5, -2, 0, +2, +5 and +10 μm. The results are summarised in Figure 6.13.

For both cases, the optimal focus value is as calculated or slightly higher. In the longest focal distance design (f=21.4 μm) in short taper configuration, a defocus of -5 μm results in 1 dB excess loss per coupler, while a positive defocus (i.e. taper longer than necessary) has nearly no influence on performance. The taper is in that case long enough to guide the light onto the wire, without extra loss. A defocus of -10 μm results in very high excess loss, since the taper is very steep in that case. In the low contrast aperture (2.0 μm) configuration, a defocus of -5.0 μm results in 1 dB excess loss per coupler and a defocus of +10 μm in 1.5 dB excess loss per coupler. In the shortest focal distance design (f=11.9 μm) in short taper configuration, a defocus of -5 μm results in 3 dB excess loss per coupler, a positive defocus of 5 μm in 1 dB excess loss per coupler, and a 10 μm positive defocus in 2 dB excess loss per coupler. In this case, the taper is still too steep. Also, at the focal point the taper is wider than the focused spot, so its guiding effect is not fully exploited. For the 5 μm defocus, the taper is a bit steeper than for the 10 μm defocus case, but at the focal point the taper is narrower, so the guiding effect will be more exploited, explaining the higher transmission in this case. In the low contrast aperture (0.8 μm) configuration, a defocus of -5.0 μm results in 1dB excess loss per coupler, a positive defocus of 5.0 μm in 0.5 dB excess loss per coupler, and a defocus of +10 μm or -10 μm in 2.5 dB excess loss per coupler.

Waveguide angle

In paragraph 6.2, we have demonstrated that the waveguides have to be rotated inwards when using angled coupling along the bisection line of the grating. However, this is not the case for focusing 2D gratings using design 2, since the phase relations are included in the calculation of the grating. For design 1, which does not take into account angled coupling in the calculation, a rotation of the waveguides is still required.

We have fabricated both design 1 and design 2 with focal distance of 11.9 μm for three values of the inward tilt of the waveguides: ψ=0° (i.e. orthogonal waveguides), ψ=2° and ψ=3.1°. The value ψ=3.1° is the optimal value used for standard non-focusing 2D gratings. The transmission is measured when using near vertical coupling at 10°. The results are shown in Figure 6.14 for an input polarisation along the diagonal of the grating.

For design 1 (calculated for vertical coupling), this angled coupling results in a phase mismatch, which must be compensated by rotating the waveguides. Also, by tilting the fibre the wavelength is blue shifted as compared to vertical coupling, which explains the shorter wavelength of the coupler spectrum. The angle giving best transmission is 3.1°. A waveguide angle of 2° results in an excess loss of 1 dB per coupling interface, which increases to 7.5 dB for orthogonal waveguides.

For design 2 (calculated for angled coupling) the orthogonal waveguide case is optimal. A waveguide angle of 2° results in an excess loss of 2 dB per coupling interface, which increases to 5.5-7.5 dB for a waveguide angle of 3.1°.

Polarisation Dependent Loss

Ideally, the PDL should be low over a wide wavelength range. Due to the tilt of the fibre, however, this is not the case as described in section

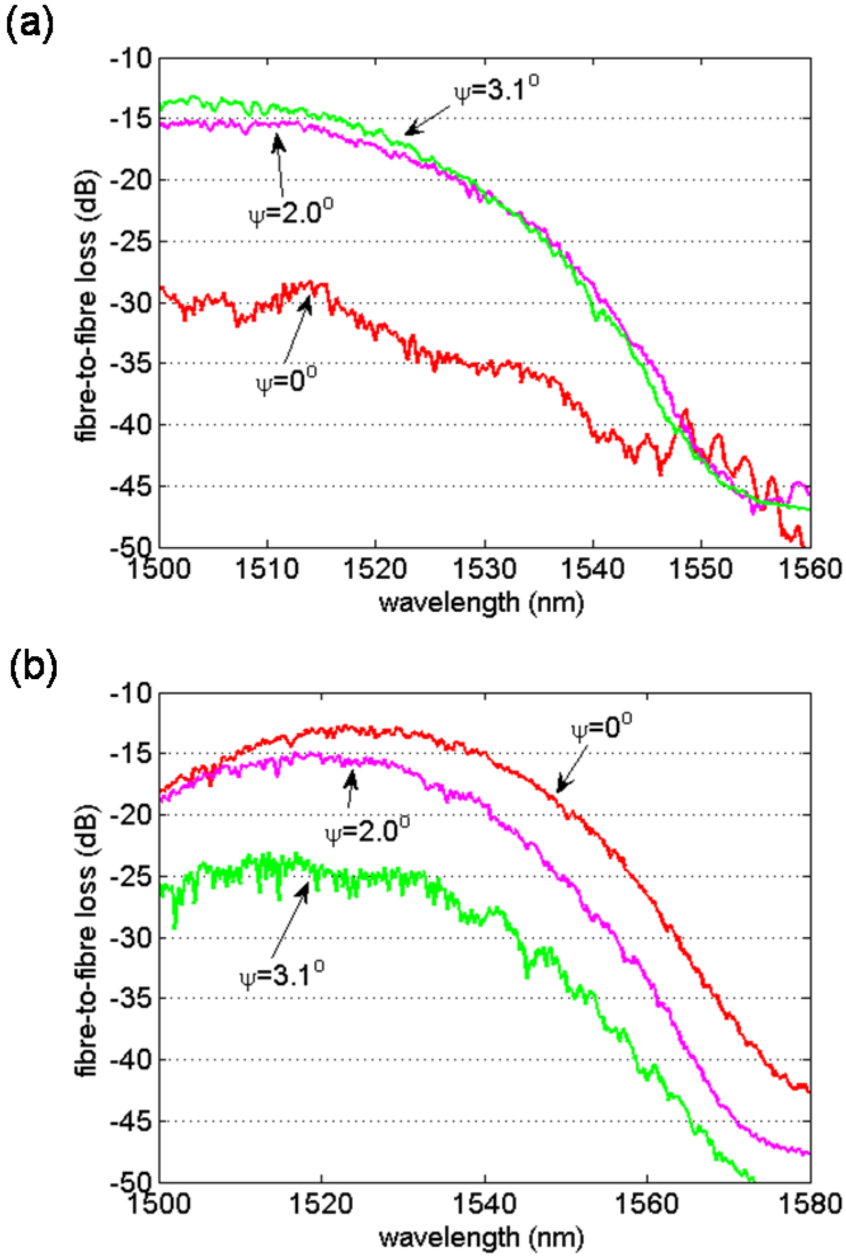

Figure 6.14: Influence of angled coupling on the waveguide angle. (a) Design 1, calculated for vertical coupling and measured for angled coupling. (b) Design 2, calculated and measured for angled coupling.

6.1.2. We have verified this experimentally on a 2D focusing grating designed for near vertical coupling (design 2) at 10° with f=21.4 μm in short taper configuration with orthogonal waveguides. We have done the measurement both for θ=10° and θ=8°, in order to investigate also the influence of the fibre angle.

The wavelength dependence of the PDL makes the alignment of the fibre not straightforward. We have carried out following procedure to obtain the results described below. First, a linear input polarisation along the diagonal of the grating is selected using a reference 1D grating. Using this input polarisation the fibres are aligned for maximum transmission and the wavelength dependence of the grating coupler is measured. Then, the fibres are realigned for minimum PDL at the measured peak wavelength. Afterwards, a longer wavelength is chosen where the PDL will be high and the input polarisation is changed for maximum and minimum transmission, each time measuring the wavelength dependence of the grating coupler. Both curves are shifted in wavelength (as simulated in Figure 6.4b) and at the wavelength $\lambda_{cross}$where they intersect, the PDL is minimum. Afterwards, the fibre alignment is further refined for minimum PDL at λ_{cross}, obtaining the final fibre alignment.

Now, the PDL is measured at discrete wavelengths, while keeping the same fibre alignment. At each wavelength, the polarisation is set for maximum and minimum transmission and the ratio between both determines the PDL. Figure 6.15 shows this maximum (magenta squares) and minimum (blue circles) transmission values as a function of wavelength for both fibre angles. Afterwards, we have set the wavelength to a value where the PDL is high and measured the wavelength dependence for two polarisations giving maximum (Figure 6.15 solid black curves) and minimum (Figure 6.15 dashed red curves) transmission. These curves experimentally demonstrate the simulated behaviour in Figure 6.4b. The discrete measured points swap between both curves at the intersection wavelength λ_{cross}.

For θ=10°, the wavelength shift between both curves is 18 nm (Figure 6.15a), while for θ=8°, this shift is 10 nm (Figure 6.15b). These measurements confirm that the PDL is more wavelength dependent if the fibre angle deviates more from vertical position. At the wavelength where maximum and minimum transmission curves intersect (λ_{cross}), the PDL is zero in theory. For longer wavelengths the ratio between maximum and minimum transmission, and thus PDL, will rapidly in-

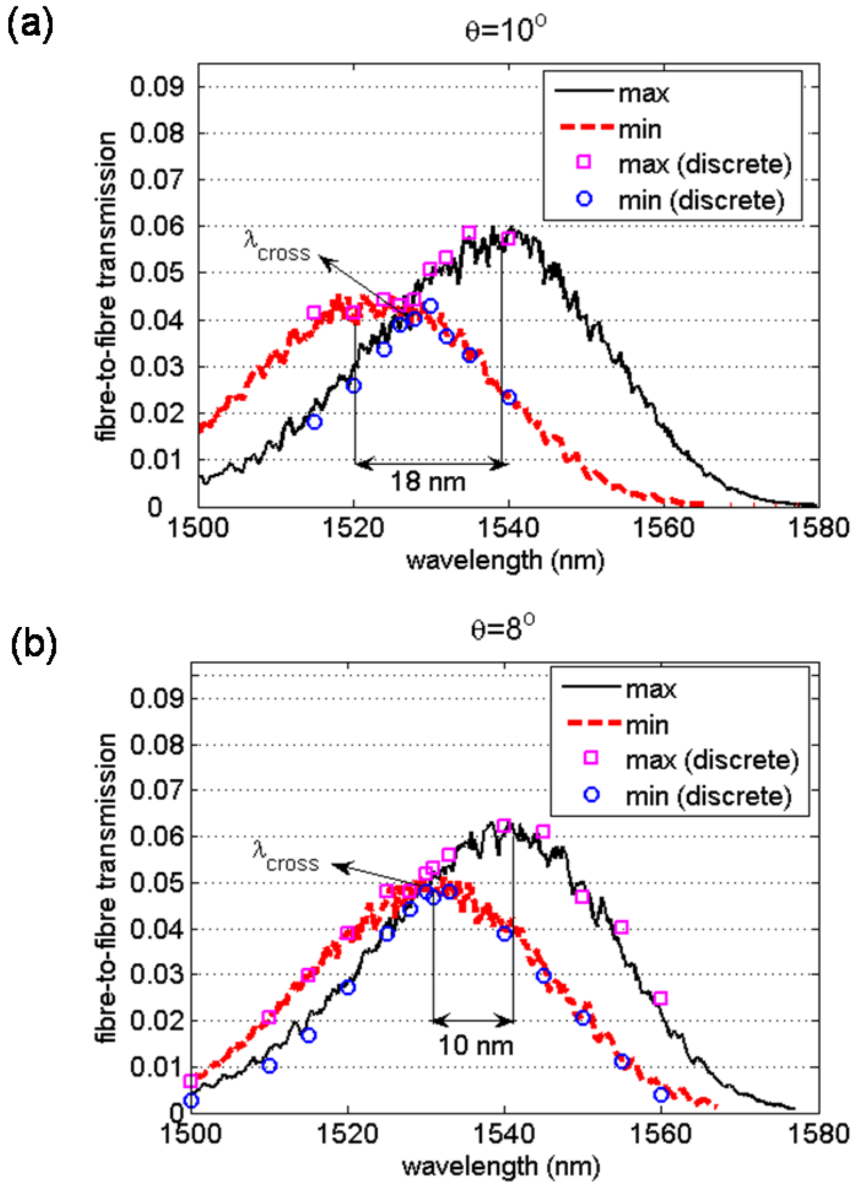

Figure 6.15: Wavelength dependence of the coupling for two input polarisations having maximum and minimum transmission. (a) θ=10°. (b) θ=8°.

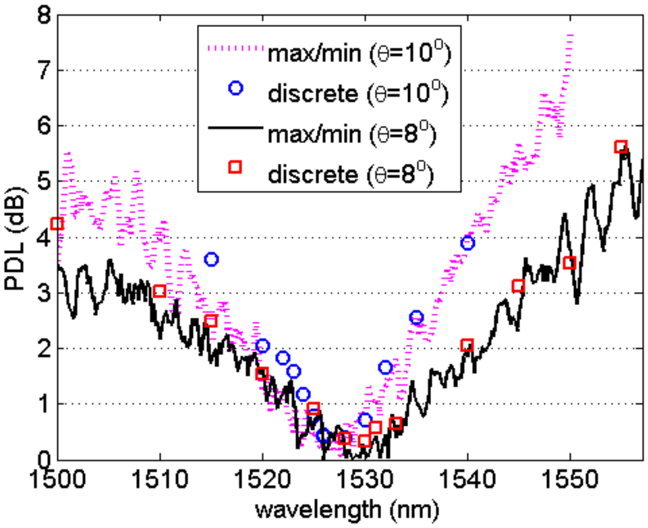

Figure 6.16: Wavelength dependence of the PDL, obtained by dividing maximum and minimum transmission curves from Figure 6.15 and by measuring maximum and minimum at discrete wavelengths.

crease. For shorter wavelengths both curves lie closer to each other and the PDL increases more slowly.

In Figure 6.16 the wavelength dependence of the PDL is shown for both fibre angles. The PDL is obtained by dividing the maximum and minimum transmission values measured at discrete wavelengths for different polarisations in Figure 6.15. However, the PDL can also be obtained by dividing the two continuous curves from Figure 6.15 (and take the absolute value).

In this case the wavelength dependence of two grating couplers is measured. The minimum fibre-to-fibre PDL is 0.4 dB at λ_{cross} (instead of zero), which is caused by slight asymmetry of the coupling configuration (fibre alignment, differences in both waveguide arms). However, the wavelength window with low PDL is very narrow. Decreasing the fibre angle further would increase that wavelength window, but vertical position (and angles close to it) can not be used due to reflections.

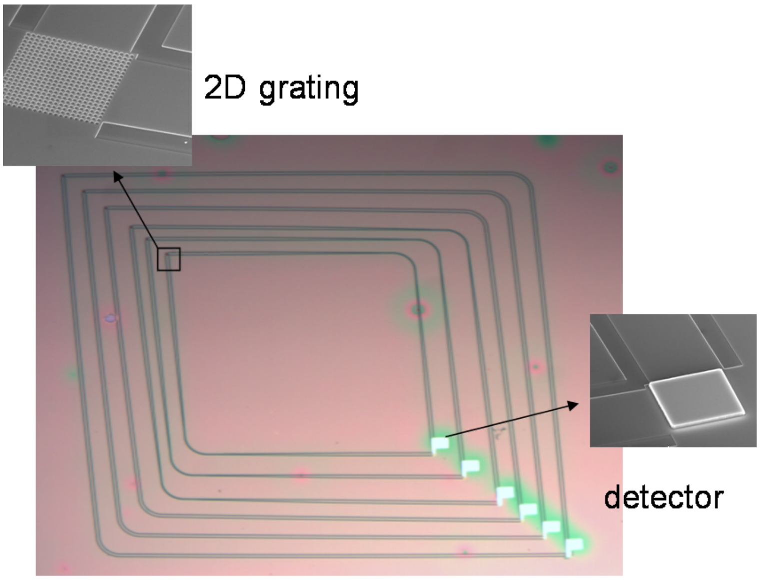

Figure 6.17: Layout of the sample implementing polarisation diversity from fibre to detector

6.4 Polarisation diversity integrated circuits in InP membrane

6.4.1 Fibre-to-detector polarisation diversity

Based on the integration scheme described in 3.4.3, we have implemented polarisation diversity from fibre to detector in InP membrane using standard 2D grating couplers. This way, we are able to characterise the PDL of a single grating coupler unambiguously. The layout is shown in Figure 6.17.

A 2D grating is put at the intersection of two (near) orthogonal waveguides, which are now recombined in a photodetector instead of another 2D grating. The photocurrent is measured at the detector while changing the polarisation randomly. The ratio I_{max}/I_{min} defines the Polarisation Diversity Loss (PDL).

We have measured the PDL at discrete wavelengths (but fixed fibre position) for two angles of the fibre, θ=10° and θ=8°. In Figure 6.18 the wavelength dependence of I_{max} and I_{min} is shown for both fibre angles. This measurement is similar to the discrete points in Figure 6.15.

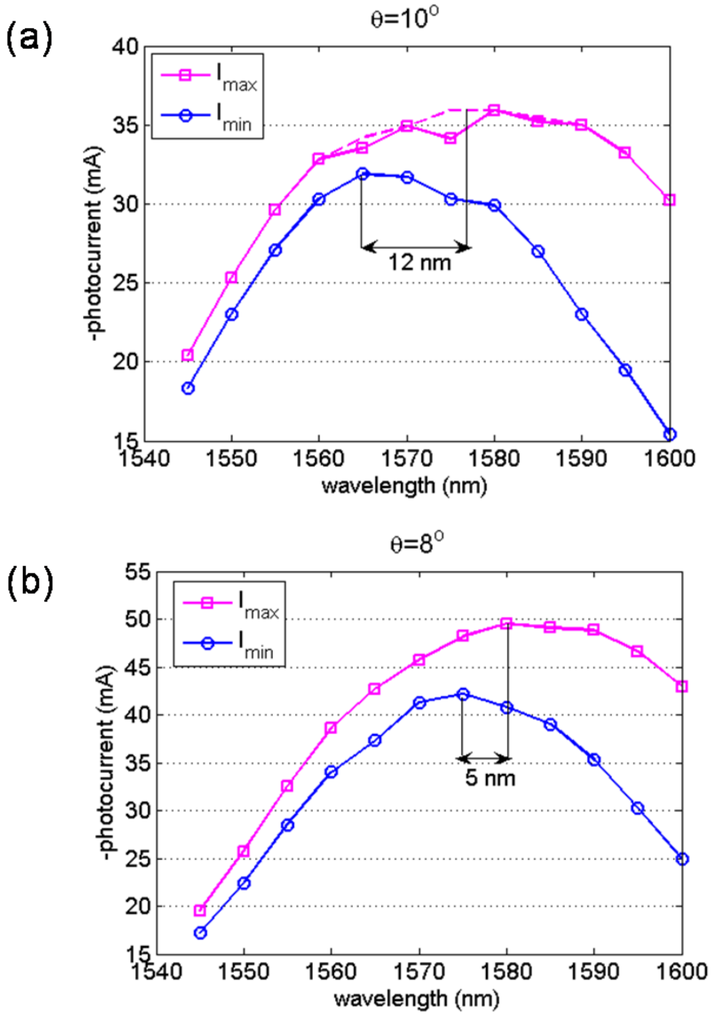

Figure 6.18: Wavelength dependence of the photocurrent when optimising the polarisation for maximum and minimum transmission, for two angles of the fibre. (a) θ=10°. (b) θ=8°).

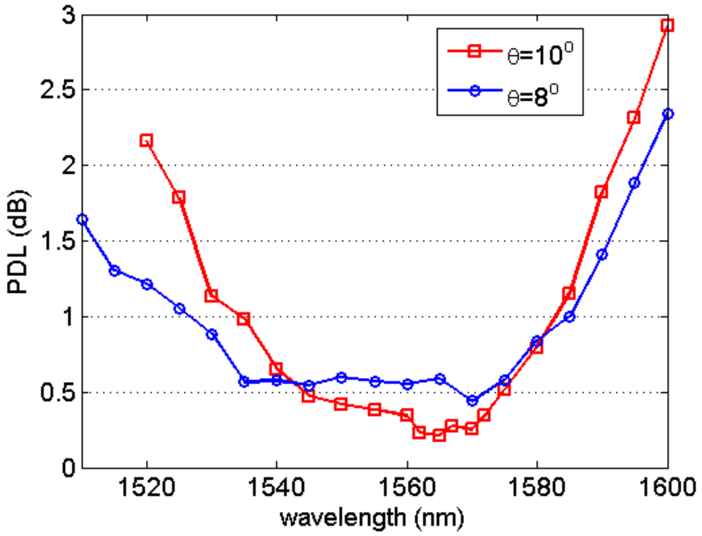

Figure 6.19: Wavelength dependence of PDL from fibre to detector.

Again, the wavelength shift between both curves increases when deviating more from vertical position and as a result, the PDL is more wavelength dependent for larger fibre angles. The wavelength dependence of the PDL is shown in Figure 6.19 for both angles. For θ=10°, the minimum PDL is 0.2 dB, and the PDL is smaller than 1 dB over more than 45 nm. For θ=8° the minimum PDL is slightly higher (0.4 dB), but the PDL is less wavelength dependent. The wavelength dependence is smaller compared to Figure 6.16. Here, we measure the wavelength dependence of a single grating coupler. The wavelength shift between maximum and minimum curves is also smaller as compared to Figure 6.16 (5 nm for θ=8° compared to 10 nm in Figure 6.16). The external responsivity is 0.23 A/W for θ=10° and 0.3 A/W for θ=8°, the difference being attributed to the waveguide angle which can not be optimal in both cases.

6.4.2 Polarisation diversity demultiplexer with integrated detectors

In previous sections, the performance of different types of polarisation diversity grating couplers was studied in different configurations.

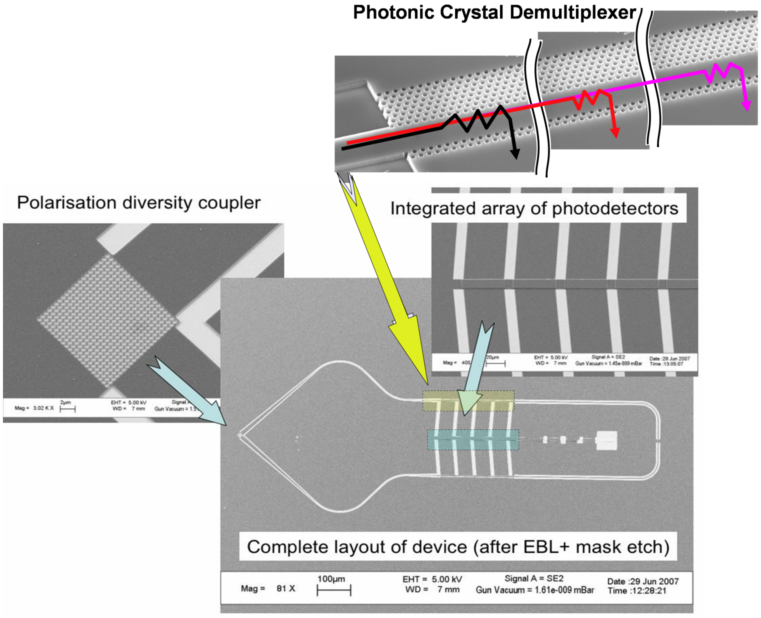

Figure 6.20: Layout of the polarisation diversity PhC demultiplexer with integrated photodetectors.

Here, we will use standard 2D gratings for obtaining a functional polarisation diversity circuit in bonded InP membrane.

The functional device is the photonic crystal demultiplexer from section 5.3.1. The layout of the sample is shown in Figure 6.20. The demultiplexer is duplicated, one in each waveguide arm, and the corresponding channel outputs and through signals of both demultiplexers are combined into a common integrated detector.

Figure 6.21 shows the detector photocurrent for three 10-nm spaced channels and the through signal. The detector of channel 4 was damaged. The PDL measurement is shown in Figure 6.22, again for the 3 channels and the through signal. The minimum PDL is 1.1 dB. The channel extraction wavelengths are at the fast increasing branch of the PDL curve. However, by changing the grating parameters (hole size, etch depth or period) or the TAMIS parameters it is possible to position the channels around the minimum PDL value and on the slowly increasing branch. The PDL is higher for this complex device because it is more difficult to achieve identity between the two arms for the respective input polarisations, each arm including a single mode bend, a strip waveguide-to-PhC transition and common detectors.

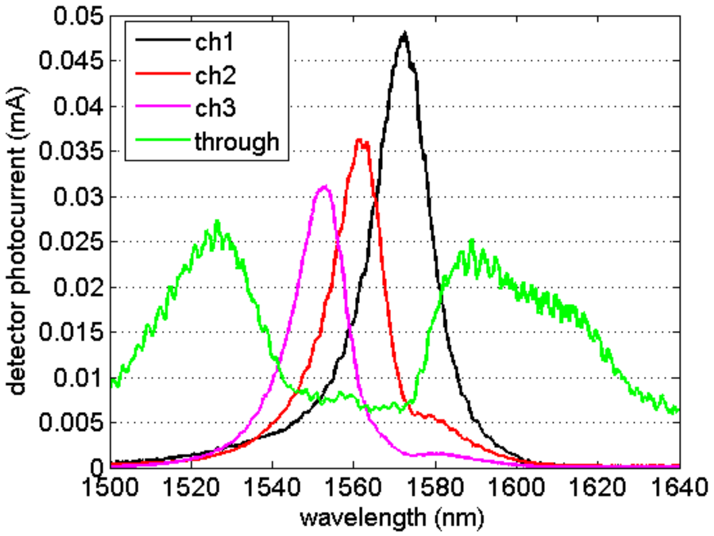

Figure 6.21: Detector output for the polarisation diversity PhC demultiplexxer (not normalised to the grating coupler, linear scale).

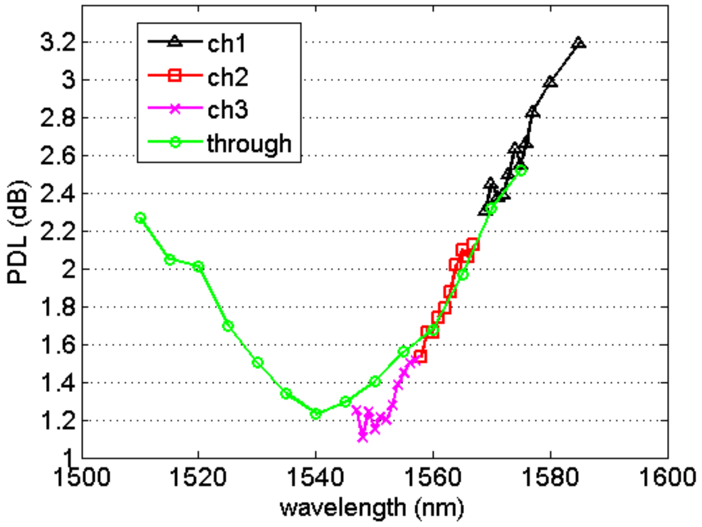

Figure 6.22: PDL as a function of wavelength for the polarisation diversity PhC demulitplexer.

6.5 Conclusions

In this chapter, we have demonstrated polarisation diversity integrated circuits using 2D grating couplers. First, the performance of the grating couplers was assessed. Grating couplers in BCB bonded InP membrane with a gold bottom mirror showed a coupling efficiency of 47% in polarisation diversity configuration. Focusing versions were demonstrated for Silicon-on-Insulator, resulting in an 8-fold length reduction of the coupling structure as compared to standard versions. Special attention was given to the influence of near vertical coupling. The PDL of a single InP membrane grating coupler was determined through a fibre-to-detector configuration in InP membrane and resulted in a minimum PDL of 0.2 dB. The PDL stays below 1 dB over a wavelength range of 45 nm. Finally, a complete polarisation diversity demultiplexer chip with integrated photodetectors was demonstrated. This resulted in normal demultiplexing behaviour and a minimum PDL of 1.1 dB.

Chapter 7

Coherent receiver

In this chapter we will describe a coherent receiver on InP membrane, based on the concepts developed in the previous chapters. We start with a theoretical description of coherent lightwave systems and then present the practical implementation and characterisation.

7.1 Coherent receivers

In the previous chapters, the devices were characterised using direct detection on integrated photodiodes. In that case, only the amplitude of the signal can be measured, while all phase information is lost. Another detection method, frequently used in radio and microwave communication systems, uses homodyne or heterodyne detection. For optical implementations of this type of detection the phase coherence is very important, and these receiver systems are therefore referred to as coherent receivers.

Coherent receivers were widely studied in the late 1980s early 1990s, but the development of the optical amplifier delayed its commercial breakthrough. Main advantage of the coherent detection approach is an improved receiver sensitivity, which can be up to 20 dB as compared to direct detection. Furthermore, the fibre bandwidth can be used more efficiently by achieving an increased spectral efficiency of WDM systems. The basics of coherent lightwave systems is well described in [106], we will lift out the important aspects here.

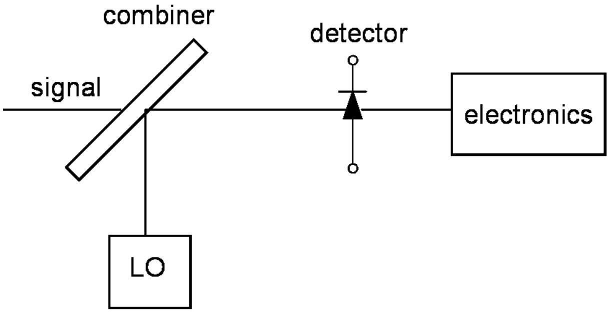

Figure 7.1: Coherent detection.

7.1.1 Basic concepts

In a coherent detection system, the optical signal is combined with a CW (continuous wave) local oscillator signal before detection occurs at a photodetector (Figure 7.1).

The optical signal is written as:

$$E_s = A_s \exp[-j(\omega_0 t + \phi_s)] \tag{7.1}$$

with ω_0 the carrier frequency, A$_s$ the amplitude and ϕ_s the phase. The field associated with the local oscillator can be written as:

$$E_{LO} = A_{LO} \exp[-j(\omega_{LO} t + \phi_{LO})] \tag{7.2}$$

with A$_{LO}$ the amplitude, ω_{LO} the frequency and ϕ_{LO} the phase. The fields are assumed to be identically polarised, and therefore the scalar notation is used. The photodetector responds to the optical intensity, which is given by

$$P = K|E_s + E_{LO}|^2 \tag{7.3}$$

with K a constant factor. Applying (7.3) with (7.1) and (7.2) results in:

$$P(t) = P_s + P_{LO} + 2\sqrt{P_s P_{LO}} \cos(\omega_{IF} t + \phi_s - \phi_{LO}) \tag{7.4}$$

with P_s=KA_s^2, P_{LO}=KA_{LO}^2 and ω_{IF}=ω_0-ω_{LO}. The frequency ν_{IF}=$\omega_{IF}/2\pi$ is called the intermediate frequency (IF) .

Homodyne detection

In homodyne detection ω_{LO}=ω_0 and the photocurrent measured at the detector is given by:

$$I(t) = R(P_s + P_{LO}) + 2R\sqrt{P_s P_{LO}} \cos(\phi_s - \phi_{LO}) \tag{7.5}$$

with R the responsivity of the detector. If we consider the case ϕ_s=ϕ_{LO} the homodyne signal becomes:

$$I_p(t) = 2R\sqrt{P_s P_{LO}} \tag{7.6}$$

In the direct detection case, the photocurrent is given by $I(t) = RP_s(t)$, indicating that with homodyne detection the average electrical power is enhanced by a factor of $4P_{LO}/\overline{P}_s$, with $\overline{P}_s$ the average optical power. As P_{LO} can be made much larger than $\overline{P}_s$, the power enhancement can be very large (more than 20 dB). Although the shot noise is also enhanced, this results in a substantially higher Signal-to-Noise Ratio (see further).

However, (7.5) reveals a phase sensitivity of the photocurrent. In practice, ϕ_s and ϕ_{LO} vary randomly over time. By using a phase-locked loop, the phase difference can be kept nearly constant, but its implementation is rather complicated.

Heterodyne detection

In heterodyne detection ω_{LO} differs from ω_0 such that ω_{IF} is in the microwave region. We get:

$$I(t) = R(P_s + P_{LO}) + 2R\sqrt{P_s P_{LO}}\cos(\omega_{IF}t + \phi_s - \phi_{LO}) \tag{7.7}$$

As $P_{LO} \gg P_s$, $R(P_s + P_{LO})$ is nearly constant and can be removed by using bandpass filters. The last term is the heterodyne signal. The local oscillator still amplifies the received signal, resulting in a SNR improvement which is 3 dB smaller than in the homodyne case due to the AC nature of the heterodyne photocurrent. However, a phase locked loop is no longer needed but phase fluctuations need to be controlled by using narrow linewidth lasers for the sources. In practice the heterodyne detection method is mostly used.

7.1.2 Advantages of coherent detection

The advantage of coherent detection can be made more clear when looking at the SNR. Both shot noise and thermal noise contribute to the noise of the receiver. The variance σ^2 of the photocurrent fluctuations is given by:

$$\sigma^2 = \sigma_s^2 + \sigma_T^2 \tag{7.8}$$

with $\sigma_s^2 = 2q(I + I_d)\Delta f$ the contribution of the shot noise, where I is given by (7.5) or (7.7) and I_d the detector dark current. Δf is the effective noise bandwidth of the receiver. The thermal noise is proportional to the temperature T and Δf. Since $P_{LO} \gg P_s$, I can be replaced in (7.8) by RP_{LO} for both homodyne and heterodyne detection.

In the heterodyne case, the SNR is given by:

$$SNR = \frac{< I_{ac}^2 >}{\sigma^2} = \frac{2R^2\overline{P}_s P_{LO}}{2q(RP_{LO} + I_d)\Delta f + \sigma_T^2} \tag{7.9}$$

P_{LO} can be made large enough that the receiver noise is determined by the shot noise, which makes the SNR:

$$SNR \approx \frac{R\overline{P}_s}{q\Delta f} \tag{7.10}$$

This equation indicates that by using coherent detection the receiver can work in the shot noise limit, even when using p-i-n detectors which are typically limited by thermal noise.

7.1.3 Balanced detectors

The introduction of the local oscillator has however a drawback, as it introduces intensity noise. Therefore, another term needs to be introduced in the equation of the SNR:

$$SNR = \frac{2R^2\overline{P}_s P_{LO}}{2q(RP_{LO} + I_d)\Delta f + \sigma_T^2 + 2R^2P_{LO}^2(RIN)\Delta f} \tag{7.11}$$

where the last term in the denominator is related to the Relative Intensity Noise (RIN) of the local oscillator. As described in the previous paragraph P_{LO} should be large enough in order to make the receiver operate in the shot noise limit. But large P_{LO} results in large intensity noise, which now scales quadratically with P_{LO}.

This problem can be solved by using balanced detectors. A schematic view of a coherent detector with balanced detectors is shown in Figure 7.2. The signal containing the information is mixed with the local oscillator using a 3 dB coupler. The optical fields at the output of the 3 dB coupler are given by [107]:

$$E_1 = \frac{1}{2}A_s \exp(-j(\omega_0 t + \phi_s)) + \frac{1}{2}A_{LO} \exp(-j(\omega_{LO} t + \phi_{LO} - \pi/2)) \tag{7.12}$$

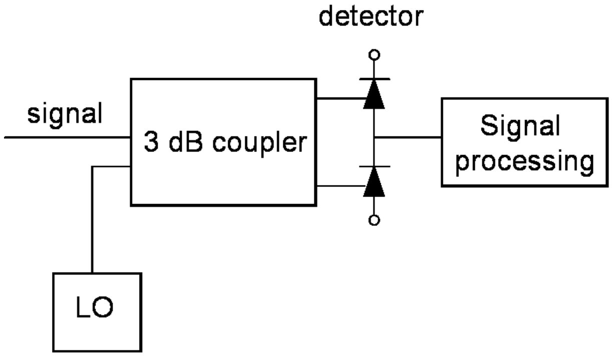

Figure 7.2: Coherent detection with balanced detectors. Photocurrents at both detectors are subtracted, eliminating a large part of the intensity noise.

$$E_2 = \frac{1}{2}A_s \exp(-j(\omega_0 t + \phi_s - \pi/2)) + \frac{1}{2}A_{LO} \exp(-j(\omega_{LO} t + \phi_{LO})) \quad (7.13)$$

The photocurrents are then given by:

$$I_1 = \frac{1}{2}R(P_s + P_{LO}) + R\sqrt{P_s P_{LO}} \cos(\omega_{IF} t + \phi_s - \phi_{LO} + \pi/2) \quad (7.14)$$

$$I_2 = \frac{1}{2}R(P_s + P_{LO}) - R\sqrt{P_s P_{LO}} \cos(\omega_{IF} t + \phi_s - \phi_{LO} + \pi/2) \quad (7.15)$$

After subtracting both currents only the intermediate frequency signal remains, and as a result, the LO intensity noise associated with the DC term is eliminated. The intensity noise associated with the IF-term is not eliminated, but due to the square root dependence of this term on P_{LO}, this is less severe. Another advantage of the balanced receiver approach is the fact that all power (signal and local oscillator) is used, while in a single arm implementation a 3 dB power penalty occurs in practice.

7.1.4 Polarisation

Equation (7.1) and (7.2) use scalar notation, since we have assumed identical polarisation for both the signal and the local oscillator. However, if this is not the case the beat term in equation (7.4) is reduced, and disappears if the polarisation states of the signal and the local oscillator are orthogonal (complete fading).

As the polarisation state of the local oscillator is determined by the laser, it remains fixed. The problem lies in the polarisation state of the

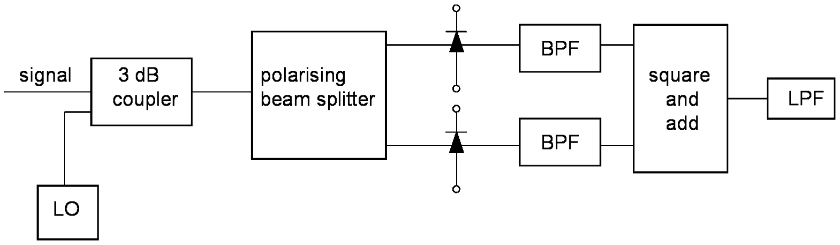

Figure 7.3: Polarisation diversity coherent detector. BPF=Band Pass Filter, LPF=Low Pass Filter.

signal, which varies over time. The polarisation problem in coherent receivers has been tackled by several approaches. One approach uses electronic tracking and feedback control to match both polarisations [108]. Another approach uses polarisation scrambling or spreading to change the polarisation of the signal randomly during a bit period (fast variations), which on average results in the same power received for each bit [109]. The most widely used method is polarisation diversity. A schematic view of such a polarisation diversity coherent receiver (without balanced detectors) is shown in Figure 7.3. The photocurrents in both detectors are given by:

$$I_1 = R\sqrt{2P_sP_{LO}}\cos\theta\cos(\omega_{IF}t + \phi_s - \phi_{LO}) \tag{7.16}$$

$$I_2 = R\sqrt{2P_sP_{LO}}\sin\theta\cos(\omega_{IF}t + \phi_s - \phi_{LO}) \tag{7.17}$$

with θ an angle determined by the polarisation state of the signal. If f_{IF} and the IF-bandwidth are much larger than the signal bandwidth, phase noise and polarisation fluctuations, it is proven in the appendix of [110] that the lowpass part of $I_1^2 + I_2^2$ is given by:

$$\text{lowpass}\ \{I_1^2 + I_2^2\} = R^2P_sP_{LO} \tag{7.18}$$

which is independent of the polarisation state of the signal (indicated by θ) and phase noise.

7.2 Practical implementation

A lot of practical realisations of coherent receivers or parts of it have been described in literature. Non-integrated polarisation diversity coherent receivers have been described in [111] (with balanced detectors) and [112] (with single detectors). However, we will focus on integrated versions.

The first demonstrations of heterodyne receiver chips featuring integrated laser, 3 dB coupler and single photodiodes have been reported in [113, 114]. A more recent implementation is reported in [115]. The first integrated polarisation diversity coherent receiver chip with balanced detectors is demonstrated in [116]. In work by Deri, both low speed [117] and high speed operation [118] of a monolithically integrated polarisation diversity receiver with balanced detectors is described. In that case, the local oscillator laser is not integrated onto the chip.

Receiver chip layout

We have implemented a coherent receiver chip on InP membrane (300 nm) without integrating the local oscillator laser. We will use an external tunable laser as the local oscillator. The integration scheme described in section 3.4.3 is used for integrating the detectors. An MMI 3 dB coupler (Figure 7.4a) is used for mixing the signal and the local oscillator. Its design is similar to the design in section 5.2.3. Simulation results are shown in Figure 7.4b-c. The central section has a width W=4.5 μm, input- and output waveguides are 1 μm wide. The waveguides are positioned at $\pm$W/6 and the optimal length of the central section is 11.74 μm.

The basic layout of the coherent receiver is shown in Figure 7.5. The signal containing the information and the local oscillator are coupled into the chip using grating couplers and mixed with an MMI coupler. The outputs of the MMI feed the integrated detectors.

7.3 Measurements

7.3.1 Detector bandwidth

For heterodyne detection, the detector bandwidth should extend to at least IF+R$_b$, with R$_b$ the bitrate [110]. A scheme of the setup for measuring the detector bandwidth is shown in Figure 7.6. The light of a tunable laser is modulated and coupled into a waveguide using a grating coupler. The light in this waveguide is coupled refractively to the underlying detector. The layout of the detector contact pads is adapted for measuring with an RF probe. As the interconnections are relatively

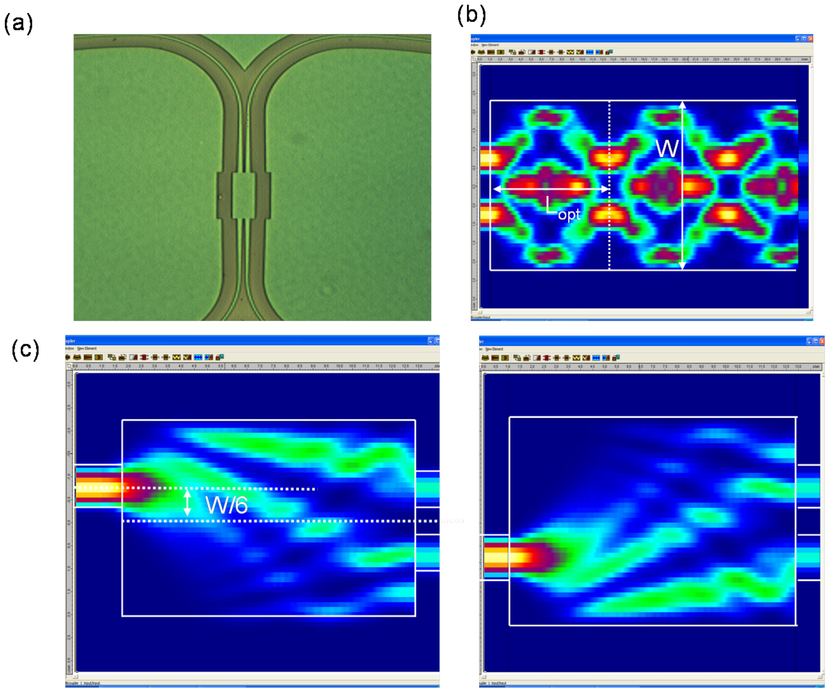

Figure 7.4: MMI 3 dB coupler. (a) Fabricated device. (b) Simulation result with two inputs excited. The length of the central section is not optimal showing multiple images. (c) Simulation results with one input excited, for optimal central section length.

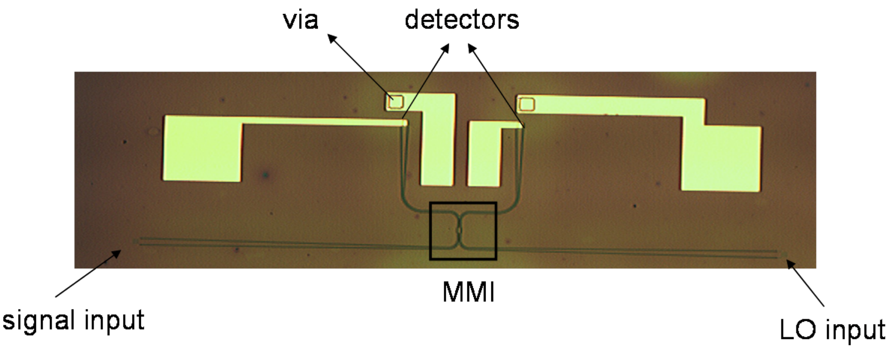

Figure 7.5: Basic layout of the coherent receiver chip. Detectors are not connected for on-chip current subtraction.

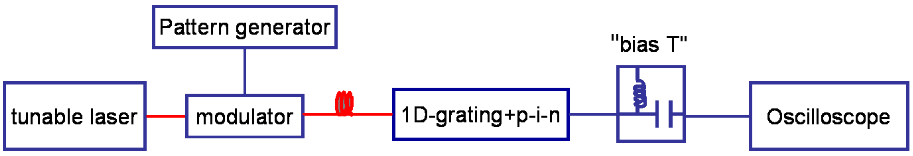

Figure 7.6: Setup for detector bandwidth measurement. An RF probe and a "bias T" is used to deliver the DC bias and extract the RF signal.

short, we have not used coplanar waveguide transmission lines on the chip. The DC reverse bias voltage for the detector is separated from the RF-signal using a "bias T". The electrical RF-signal from the detector is measured at an oscilloscope.

The modulator at INTEC is limited to frequencies around 9-10 GHz. The frequency response of the detector up to 9 GHz is shown in Figure 7.7, from which the 3 dB bandwidth is estimated to be around 10 GHz. Since we have no information on internal resistances and parasitic effects, it is difficult to indicate the bandwidth limiting factor. A similar detector structure described in [119] (footprint of 5 x 10 μm^2, intrinsic absorbing layer of 700 nm) has an expected 3 dB bandwidth of around 25 GHz, which is in their case limited by the carrier transit time.

The optical signal and the corresponding electrical signal at the detector, for an input frequency of 9 GHz, are shown in Figure 7.8a-b. Eye diagrams for 2 GHz, 4 GHz, 6 GHz and 8 GHz modulation are shown in Figure 7.9a-d. From the bandwidth measurement we would expect eye closing at frequencies above 10 GHz, while the measured eye closes already at 8 GHz. The measurement suffers from a lot of noise, both for low and high frequencies. However, the amplitude of the electrical signals in Figure 7.9 is only slightly decreasing when increasing the modulation frequency. There is also timing jitter,which is indicated by the width of the crossing of rising and falling edge (shown in Figure 7.9c). As the modulation frequency increases, this time error represents a larger portion of the cycle, causing the horizontal closing of the eye. Noise contributions come from the input tunable laser source, detector shot noise, load resistor thermal noise and possibly environmental contributions. Amplifying the electrical signal before the oscilloscope did not improve the measurement, which indicates that oscilloscope noise is negligible here. We did not adapt the contact layout for 50 Ω impedance matching, which might also be the cause of some of the above problems due to unwanted reflections.

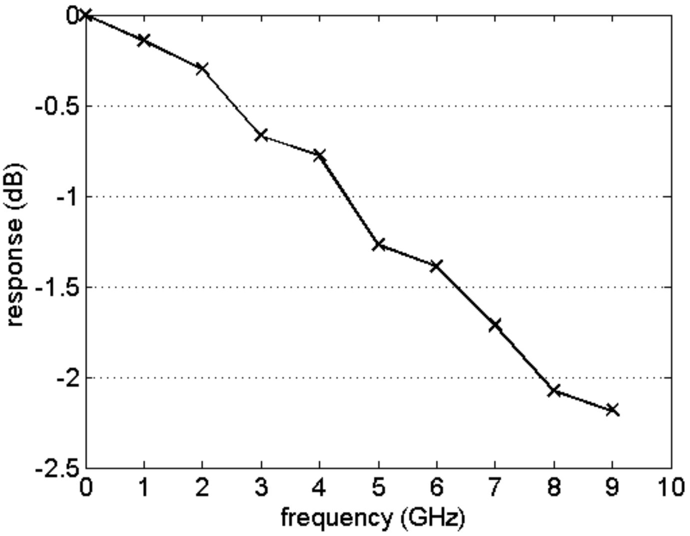

Figure 7.7: Frequency response of the detector.

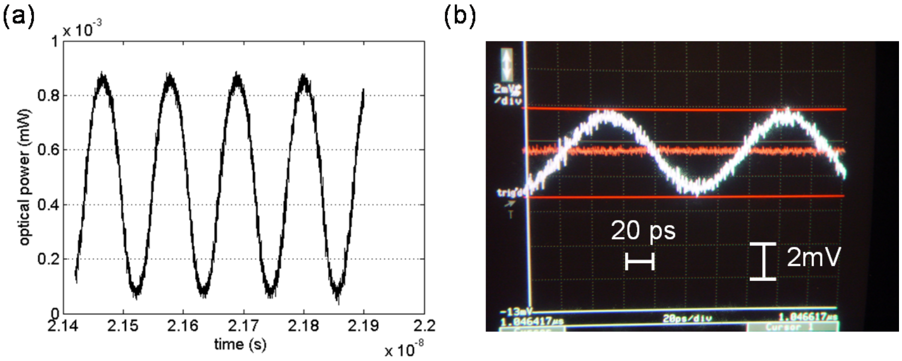

Figure 7.8: (a) Optical input signal. (b) Electrical output signal at the oscilloscope.

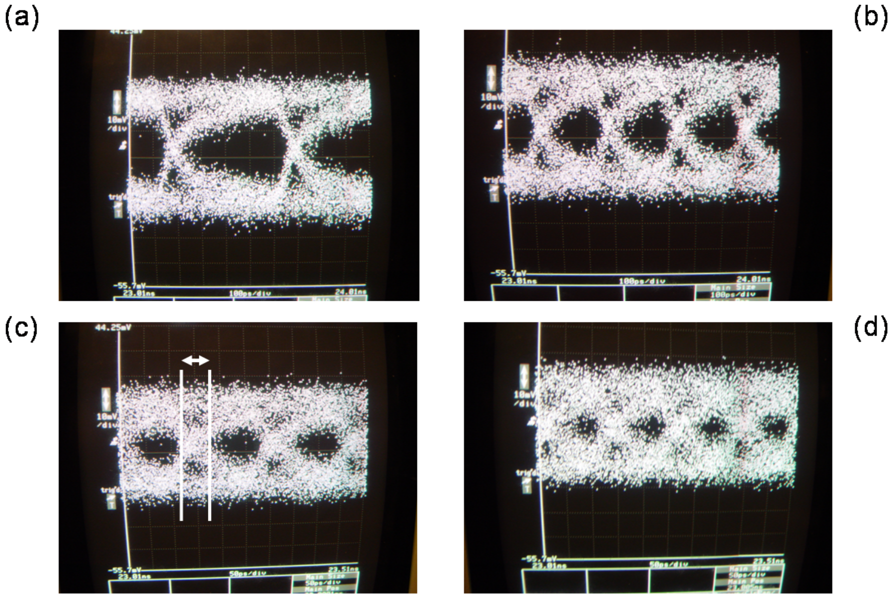

Figure 7.9: Eye diagrams at different modulation speeds. (a) 2 GHz. (b) 4 GHz. (c) 6 GHz. (d) 8 GHz.

7.3.2 Intermediate Frequency response

By mixing the optical signal with the local oscillator in the MMI coupler the intermediate frequency (IF) signal is obtained. The setup for measuring the intermediate frequency response is similar to Figure 7.6 except for the oscilloscope which is replaced by an electrical spectrum analyser. Two tunable lasers are used for the optical signal and the local oscillator respectively. In Figure 7.10, we superimpose the measured intermediate frequencies obtained by sequentially changing the wavelength difference of both tunable lasers. From this figure, a 3 dB IF-bandwidth of around 10 GHz is deduced.

Modulated signal

In practice, the information to be submitted is encoded in the modulation of the signal. We have transmitted a 101010... optical signal as shown in Figure 7.11a, where the duration of a bit is 0.25 ns. The measured frequency content of this (optical) pattern is shown in Figure 7.11b. The main frequency is 2 GHz, the harmonics having different amplitudes are spaced at 2 GHz.

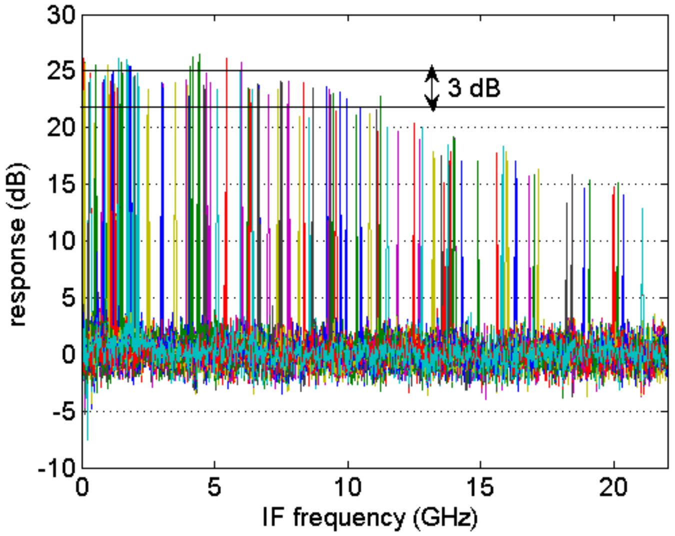

Figure 7.10: Intermediate Frequency response obtained by varying the wavelength difference between signal and local oscillator.

In Figure 7.11c the frequency response of the detector is shown when only the modulated signal is transmitted and measured at the detector (LO tunable laser off, direct detection). The 2 GHz frequency is measured, together with the strongest harmonics whose spacing is 4 GHz. The weakest harmonics do not extend above the noise floor. When turning the local oscillator on, the intermediate frequency signal appears together with the lower sidebands and the direct detected frequencies.

The presence of all these frequencies proves the correct operation of the mixing. However, in order to see this number of direct detected higher harmonics, the optical signal needs to be sufficiently strong for the harmonics to extend above the noise floor. In this case, the difference in power between signal and local oscillator could not be made high enough to see the advantage of coherent detection[1].

However, in practice the modulated signal is much weaker. In Figure 7.12 we show the heterodyne detected signal for a weak 1.5 GHz signal and a much stronger local oscillator. In Figure 7.12a the higher harmonics do not extend above the noise floor in this case. There is a

---

[1] The power of both tunable lasers was set at maximum, resulting in contributions of signal and local oscillator which are of the same order of magnitude.

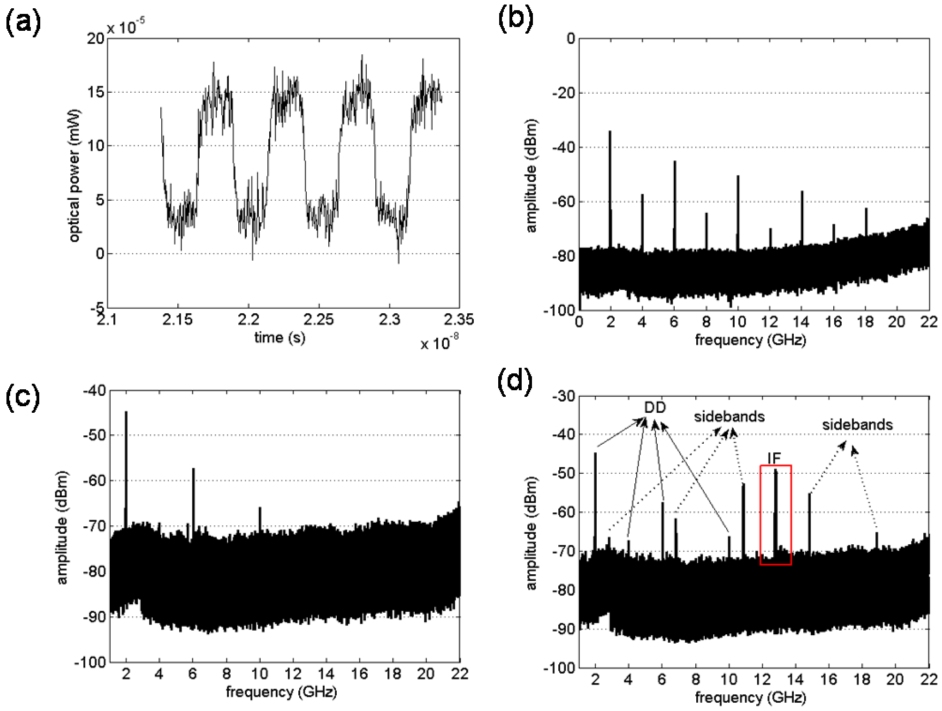

Figure 7.11: Coherent detection with strong modulated signals. (a) Optical signal to be transmitted. (b) Frequency content of the optical signal. (c) Direct detected signal (LO off). (d) Coherent detected signal (LO on), DD=Direct Detection.

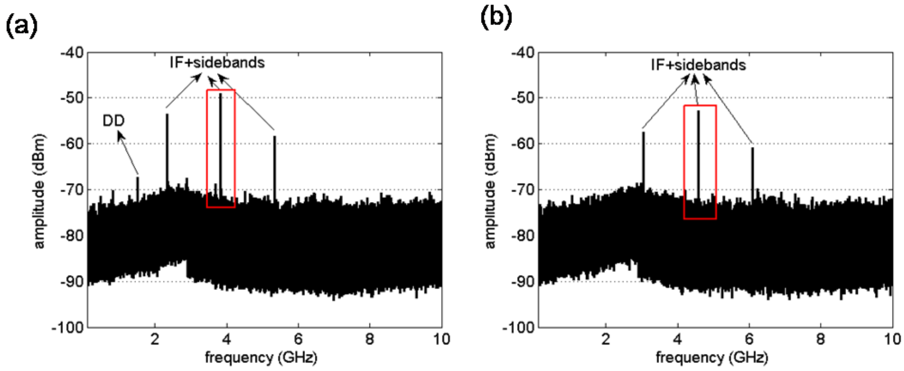

Figure 7.12: Coherent detection with weak modulated signals. (a) The directed detected term extends just above the noise floor (b) The signal is too weak to be directly detected.

14 dB difference in power between the direct detected 1.5 GHz signal and the lower sideband of the IF-signal. When further decreasing the power of the signal, the direct detected term completely disappears, while the IF-signal is still clearly detected (Figure 7.12b). Due to wavelength instability of the tunable laser for different output powers the IF-frequency is shifted 500 MHz between both measurements.

The demodulation of the signal is typically performed electronically, which we have not done here. This demodulation often consists of bandpass filtering the IF-signal and its first lower sideband, then mixing both using a square law device and finally filtering to baseband. An example of such a complete receiver is described in [115].

7.3.3 Common Mode Rejection Ratio (CMRR)

The Common mode Rejection Ratio (CMRR) is a measure for the local oscillator noise suppression. If the photocurrents of both detectors at the outputs of the 3 dB coupler are I_1 and I_2, the CMRR is defined as [118]:

$$CMRR = -20\log_{10}\frac{|I_1 - I_2|}{(I_1 + I_2)/2} \tag{7.19}$$

The CMRR is mainly determined by the splitting ratio of the 3 dB coupler and the identical efficiency of the photodetectors. For a perfect 50/50 splitting ratio and identical photodetectors, the local oscillator noise associated with the DC photocurrent is completely suppressed (see section 7.1.3).

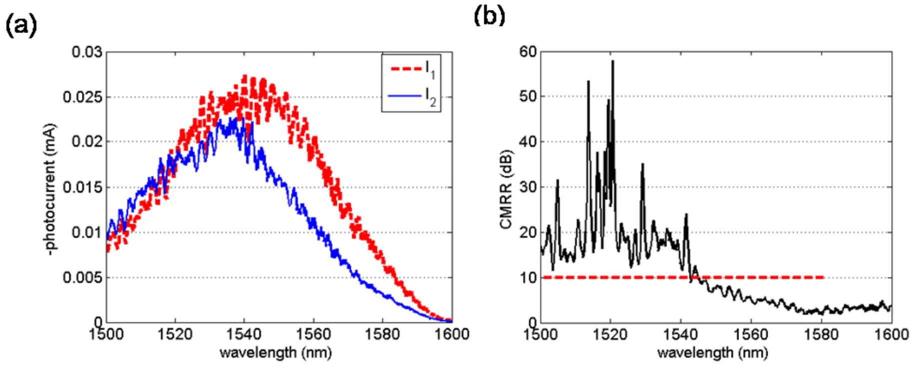

Figure 7.13: Characterisation of MMI+detectors using the local oscillator input. (a) photocurrent at both detectors. (b) CMRR calculated using (7.19).

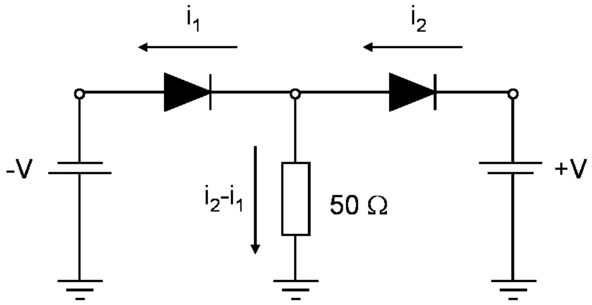

Figure 7.14: Interconnections for on-chip current subtraction.

We have characterised the splitting ratio of the combination of MMI + detectors using the local oscillator input. The detectors are not connected for balanced operation. The result is shown in Figure 7.13a. There is a peak wavelength shift of 5 nm between both detector photocurrents. (7.19) can be used to calculate the CMRR. The calculated CMRR stays below 10 dB over a broad wavelength range.

On-chip current subtraction

For current subtraction on the chip, both photodetectors need to be connected and biased as shown in Figure 7.14.

However, for the layer structure used in this work on-chip current subtraction was not possible, the reason being indicated in Figure 7.15. Due to residual conductivity of the n-doped InP membrane waveguide, a low resistance path occurs across one photodiode resulting in high

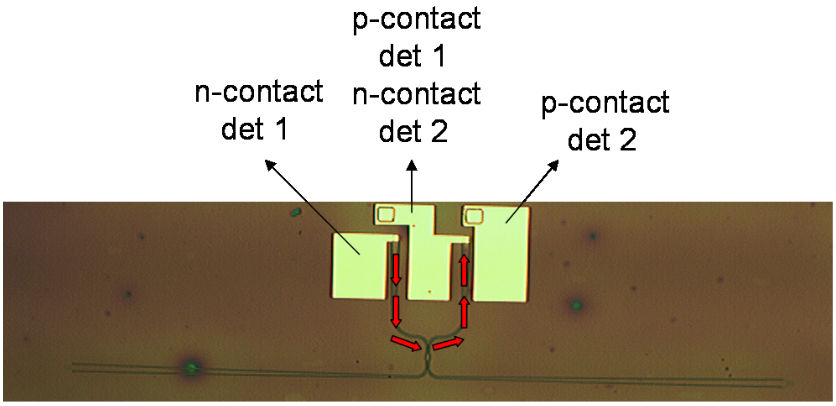

Figure 7.15: Interconnection for on chip current subtraction. Red arrows indicate a leakage path for one photodiode due to residual waveguide conductivity.

photocurrents even for small bias voltages. A possible solution would be to make a narrow (few tens of nm) slot in both output waveguides of the MMI, which would interrupt the electrical connection without causing too much excess optical loss. Another solution is making a detector design where detector and waveguide are electrically separated.

When using photodiodes which are not interconnected, the photocurrent of both photodiodes can still be subtracted using an external 0-180 ° shifted splitter combiner [120, 121].

7.3.4 Polarisation diversity

Polarisation diversity can be elegantly implemented using 2D grating couplers as shown in Figure 7.16. The photocurrent on each detector pair should first be subtracted for local oscillator noise suppression. Afterwards both IF-photocurrent signals should be squared and added electronically for polarisation independent operation (see section 7.1.4).

We have not measured the PDL of this device, since for aligning the fibers it is necessary to know the output of both detector pairs simultaneously. This would require a complete version (with electronics), which was not possible at the time of measuring. However, the polarisation diversity implementation is similar to what is described in Chapter 6, and the same results are expected.

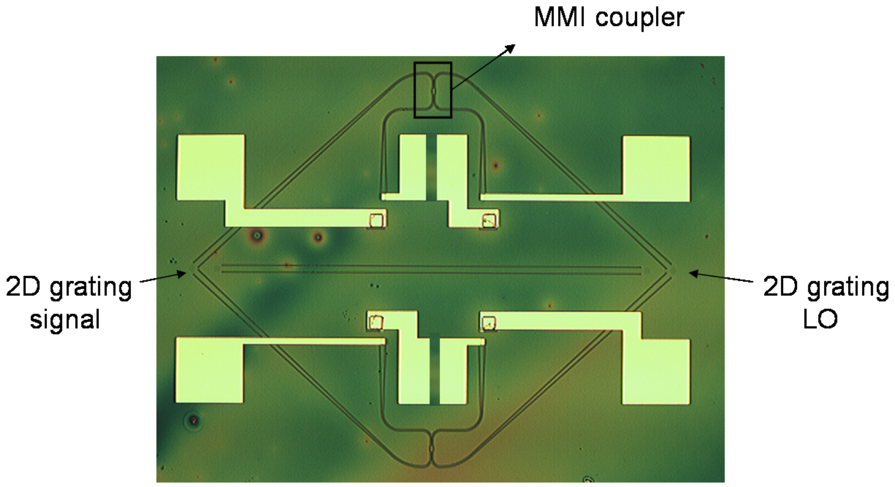

Figure 7.16: Polarisation diversity coherent receiver.

7.4 Conclusions

In this chapter we have demonstrated a coherent receiver chip on InP membrane. We have first given a theoretical description of coherent lightwave systems. Among others, improved receiver sensitivity is the main advantage of coherent detection. Then a practical implementation of a coherent receiver was described. The 3 dB bandwidth of the integrated detectors was determined to be around 10 GHz. By mixing the optical signal with a local oscillator signal an intermediate frequency (IF) signal is generated, the IF being the frequency difference between both. Current subtraction of balanced detectors, which is required for local oscillator noise suppression, was not possible due to residual conductivity of the InP membrane waveguide. For a complete coherent receiver, including polarisation diversity and demodulation to baseband, further electronic signal processing is required.

Chapter 8

Conclusions and perspectives

8.1 Conclusions

Optical communication has the potential for being the answer to the ever increasing demand for bandwidth. Like in electronics, integration and miniaturisation are key words towards optical communication at an acceptable price. They are also key words for summarising this work. The other important aspect is the choice for InP as the base material, which is motivated by the possibility for implementing active functionality in an efficient way.

We have used a reliable bonding technique using the polymer BCB for obtaining a high vertical index contrast InP membrane structure. This enables to make ultra-compact components for achieving a high integration density in InP material, in contrast to classical substrate type InP layer structures.

Two important problems in integrated optics have been tackled: fibre coupling and the inherent polarisation sensitivity of optical components on the chip. With regards to fibre coupling, we have transferred existing designs for Silicon-on-Insulator (SOI) grating couplers to InP membrane. This is possible due the the similar vertical refractive index contrast of both layer structures. Furthermore, we have described and experimentally demonstrated a substantial performance increase of these grating couplers both in terms of coupling efficiency and compactness. By including a bottom mirror into the layer structure, a coupling efficiency of 69% and 60% has been obtained experimentally for SOI and InP membrane gratings, respectively. Focusing gratings are used for omitting long adiabatic transitions in the coupling structure, resulting in an 8-fold length reduction. With regards to the polarisation problem, the same improvements have been implemented for 2D polarisation diversity grating couplers. A detailed experimental analysis of the influence of angled coupling has been presented.

These concepts on fibre coupling and polarisation diversity have been applied for demonstrating a series of integrated devices in bonded InP membrane. Both wire based and photonic crystal based devices can exist next to each other on the chip. Photonic wire based devices like ring resonators and power splitters and a photonic crystal based demultiplexer sustain our technological effort. Furthermore, we have implemented a complex fabrication scheme for integrating efficient waveguide detectors which have been used for characterising some of the integrated devices. The final demonstration is a coherent receiver chip with integrated detectors.

8.2 Perspectives

The series of well performing devices on InP membrane presented in this work prove that the used and developed technology has reached a satisfying level of maturity. Improvement on propagation loss can be expected from optimising the processes for pattern definition (lithography and etching).

On the device side, some photonic integrated circuit building blocks are still missing. We have integrated well performing p-i-n detectors onto the InP membrane platform but other active devices like lasers (e.g. for the local oscillator in a coherent receiver) and amplifiers are also required for achieving a complete transmitter/receiver chip. The main difficulty is the electrical contacting of membrane devices, due to the presence of the optical mode near the contacts. The low thermal conductivity of BCB, causing heating of the active devices, might be another problem.

Further improvement is required on the polarisation diversity implementation. Especially the wavelength dependence of the PDL needs to be reduced or even totally removed. One approach could be to switch to perfectly vertical coupling, in which case the second order reflection needs to be suppressed. This can be done by changing the grating design through inserting additional slits [122], but this might impose stringent fabrication tolerances. The other option is to compensate for the different coupling for both orthogonal polarisations. This will require extensive 3D simulations, where we have met the limits of computational resources. When using FDTD with an acceptably small grid step, the memory requirements are extremely high and optimising structures using optimisation algorithms takes unacceptable time. Performing parallel calculations on a cluster of simulation machines can be a solution. During the last months of this PhD, this kind of simulations have been started at INTEC, but further improvement on memory and stability is required. However, by approximating the structure to a more simple one, a lot of physical insight can already be gained in some cases, as we have demonstrated for focusing 2D grating couplers. A first step towards simplifying complex grating structures by reducing the 3D problem to a 2D problem has been described in the master's thesis of Elewout Hallynck [123].

Packaging of the chips with stable fibre inputs and outputs is another remaining task. We have tried to simply glue fibres onto the chip, but the results were not satisfying. The alignment of the fibres was not stable over time, and therefore a more robust approach is required. Also the wire bonding of the active devices needs special care as the force applied onto the membrane when making the bond might be too high.

Appendix A

Calculation of polarization diversity focusing gratings

In this appendix, we give the formulas and Matlab routines that can be used for calculating focusing polarization diversity grating couplers.

A.1 Design 1 (θ=0°)

This routine implements the required equations for overlaying the two orthogonal 1D-focusing gratings for design 1 (θ=0°).

```
function F = design1(x, q1, q2)

nt=1;
lambda=1.56;
neff=2.67;
qmiddle=33

L=qmiddle*lambda/neff;

F=[q1*lambda-neff*sqrt(x(2)*x(2)+x(1)*x(1));
q2*lambda-neff*sqrt((x(1)-L)*(x(1)-L)+(x(2)+L)*(x(2)+L));];
```

A.2 Design 2 (θ=10°)

This routine implements the required equations for overlaying the two orthogonal 1D-focusing gratings for design 2 (θ=10°).

```
function F = design2(x, q1, q2)

nt=1;
lambda=1.55;
theta=10*pi/180;
neff=2.73;
qmiddle=33

L=qmiddle*lambda/(neff-sin(theta)*cos(pi/4)*nt);

F=[q1*lambda+sin(theta)*cos(pi/4)*nt*(x(1)+x(2))
-neff*sqrt(x(2)*x(2)+x(1)*x(1));
q2*lambda+sin(theta)*cos(pi/4)*nt*((x(1)-L)+(x(2)+L))
-neff*sqrt((x(1)-L)*(x(1)-L)+(x(2)+L)*(x(2)+L));];
```

A.3 Calculate the intersection points

This routine is used to calculate the intersection of the overlay of both gratings. A first rough approximation of the solution needs to be given, from which Matlab calculates the right intersection coordinates. These coordinates are written to a text file.

```
clear all;
close all;
matrix_z=[];
matrix_y=[];
i=1;

for q1=21:1:45
    for q2=21:1:45
        j=q2-20;
        x0= [11,-5];% Approximation of the solution
        options = optimset('Display','off');
        x = fsolve(@(x) design1(x,q1,q2), x0, options);
```

```
        matrix_z(i)=x(1);
        matrix_y(i)=x(2);
        i=i+1;
        clear x
    end
end

gratingfile=['2Dgrating_z.cmd'];
fid=fopen(gratingfile, 'wt');
fprintf(fid, '%s\n %1.4f\n %1.4f\n', matrix_z);

gratingfile=['2Dgrating_y.cmd'];
fid=fopen(gratingfile, 'wt');
fprintf(fid, '%s\n %1.4f\n %1.4f\n', matrix_y);
```

Appendix B

Publications and awards

B.1 International Journals

1. F. Van Laere, M. Ayre, D. Taillaert, D. Van Thourhout, T. F. Krauss, R. Baets, Compact and efficient fibre-to-waveguide grating couplers in InP-membrane, *Electronics Letters*, 42(6): 343-345, 2006.
2. D. Taillaert, F. Van Laere, M. Ayre, W. Bogaerts, D. Van Thourhout, P. Bienstman, R. Baets, Grating couplers for coupling between optical fibers and nanophotonic waveguides, *Japanese Journal of Applied Physics (invited)*, 45(8A): 6071-6077, 2006.
3. F. Van Laere, G. Roelkens, M. Ayre, J. Schrauwen, D. Taillaert, D. Van Thourhout, T. F. Krauss, R. Baets, Compact and highly efficient grating couplers between optical fiber and nanophotonic waveguides, *Journal of Lightwave Technology*, 25(1): 151-156, 2007.
4. G. Vecchi, F. Raineri, I. Sagnes, K-H. Lee, S. Guilet, L. Le Gratiet, A. Talneau, A. Levenson, R. Raj, F. Van Laere, G. Roelkens, D. Van Thourhout, R. Baets, High contrast reflection modulation near 1.55 um in InP 2D photonic crystals on silicon wafer, *Optics Express*, 15(3): 1254-1260, 2007.
5. F. Van Laere, Maria V. Kotlyar, D. Taillaert, D. Van Thourhout, Thomas F. Krauss, R. Baets, Compact slanted grating couplers between optical fiber and InP-InGaAsP waveguides, *IEEE Photonics Technology Letters*, 19(6): 396-398, 2007.
6. G. Vecchi, F. Raineri, I. Sagnes, K.H.-Lee, S. Guilet, L. Le Gratiet, F. Van Laere, G. Roelkens, D. Van Thourhout, R. Baets, A. Leven-

son, R. Raj, Photonic-crystal surface-emitting laser near 1.55 m on gold-coated silicon wafer, *Electronics Letters*, 43(6): 343-345, 2007.

7. J. Schrauwen, F. Van Laere, D. Van Thourhout, R. Baets, Focused-ion-beam fabrication of slanted grating couplers in silicon-on-insulator waveguides, *IEEE Photonics Technology Letters*, 19(11): 816-818, 2007.

8. S. Scheerlinck, J. Schrauwen, F. Van Laere, D. Taillaert, D. Van Thourhout, R. Baets, Efficient, broadband and compact metal grating couplers for silicon-on-insulator waveguides, *Optics Express*, 15(15): 9625-9630, 2007.

9. F. Van Laere, T. Claes, J. Schrauwen, S. Scheerlinck, W. Bogaerts, D. Taillaert, L. O'Faolain, D. Van Thourhout, R. Baets, Compact focusing grating couplers for Silicon-on-Insulator integrated circuits, *IEEE Photonics Technology Letters*, 19(23): 1919-1921, 2007.

10. F. Van Laere, T. Stomeo, D. Taillaert, G. Roelkens, D. Van Thourhout, T. F. Krauss, R. Baets, Efficient polarization diversity grating couplers in bonded InP-membrane, *IEEE Photonics Technology Letters*, 20(4): 318-320, 2008.

11. T. Stomeo, F. Van Laere, M. Ayre, C. Cambournac, H. Benisty, D. Van Thourhout, R. Baets, T. F. Krauss, Integration of grating couplers with compact PhC demux on InP Membrane, *Optics Letters*, 33(8): 884-886, 2008.

12. D. Van Thourhout, G. Roelkens, R. Baets, W. Bogaerts, J. Brouckaert, P. Debackere, P. Dumon, S. Scheerlinck, J. Schrauwen, D. Taillaert, F. Van Laere, J. Van Campenhout, Coupling mechanisms for a heterogeneous silicon nanowire platform, *Semiconductor Science and Technology*, 23: 064004(9pp), 2008

13. F. Van Laere, T. Stomeo, C. Cambournac, M. Ayre, R. Brenot, H. Benisty, G. Roelkens, T. F. Krauss, D. Van Thourhout, R. Baets, Nanophotonic polarization diversity demultiplexer chip, accepted for publication in *Journal of Lightwave Technology*.

14. F. Van Laere, W. Bogaerts, P. Dumon, G. Roelkens, D. Van Thourhout, R. Baets, Focusing polarization diversity grating couplers in Silicon-on-Insulator, accepted for publication in *Journal of Lightwave Technology*.

B.2 International Conference Proceedings

1. F. Van Laere, D. Taillaert, D. Van Thourhout, R. Baets, M. V. Kotlyar, T. F. Krauss, A compact fibre-to-waveguide coupler based on angled slots, *European Conference on Optical Communication (ECOC)*, Glasgow, United Kingdom: p.Tu3.6.5, 2005.

2. F. Van Laere, G. Roelkens, J. Schrauwen, D. Taillaert, P. Dumon, W. Bogaerts, D. Van Thourhout, R. Baets, Compact grating couplers between optical fibers and Silicon-on-Insulator photonic wire waveguides with 69% coupling efficiency, *Optical Fiber Communications (OFC)*, Anaheim, United States: p.PDP15, 2006.

3. F. Van Laere, M. Ayre, D. Taillaert, D. Van Thourhout, T. F. Krauss, R. Baets, Compact and efficient fiber-to-waveguide grating couplers in InP-membrane, *SPIE Photonics Europe*, Strasbourg, France: 6182(174), 2006.

4. P. Bienstman, F. Van Laere, D. Taillaert, P. Dumon, W. Bogaerts, K. De Vos, D. Van Thourhout, R. Baets, High index-contrast silicon-on-insulator nanophotonics, *ICTON (invited)*, Nottingham, United Kingdom: p.Tu.D2.1, 2006.

5. P. Bienstman, P. Dumon, W. Bogaerts, D. Taillaert, F. Van Laere, K. De Vos, D. Van Thourhout, R. Baets, Silicon nanophotonics using deep-UV lithography, *APOC 2006 (invited)*, Gwangju, South Korea: 6351(99), 2006.

6. F. Van Laere, M. Ayre, D. Taillaert, D. Van Thourhout, T. F. Krauss, R. Baets, Compact and highly efficient grating couplers between optical fiber and nanophotonic waveguides in bonded InP-membranes, *European Conference on Optical Communication (ECOC)*, Cannes, France: p.Tu1.4.5, 2006.

7. H. Benisty, L. Martinelli, O. Khayam, M. Ayre, M. Kotlyar, T. F. Krauss, M. Midrio, R. Brenot, G. H. Duan, F. Van Laere, D. Van Thourhout, K. Janiak, H. Heidrich, M. Kamp, R. Houdre, L. A. Dunbar, D. Gallagher, Photonic-crystal-based optical functions for metropolitan area networks: polarisation control, linear amplification, wavelength selection, *European Conference on Optical Communication (ECOC)*, Cannes, France: p.We 1.2.2, 2006.

8. A. Mizutani, N. Ikeda, Y. Watanabe, N. Ozaki, Y. Takata, Y. Kitagawa, F. Van Laere, R. Baets, Y. Sugimoto, K. Asakawa, Planar focusing lens grating for vertical coupling on 2D photonic crystal slab waveguide, *IEEE LEOS Annual Meeting Conference Proceedings*, Montreal, Canada: p.843-844, 2006.
9. F. Van Laere, W. Bogaerts, D. Taillaert, P. Dumon, D. Van Thourhout, R. Baets, Compact focusing grating couplers between optical fibers and Silicon-on-Insulator photonic wire waveguides, *Optical Fiber Communications (OFC)*, Anaheim, United States: p.OWG1, 2007.
10. J. Schrauwen, F. Van Laere, D. Van Thourhout, R. Baets, Focused-ion-beam fabrication of slanted fiber couplers in silicon-on-insulator waveguides, *13th European Conference on Integrated Optics (ECIO)*, Copenhagen, Denmark, 2007.
11. S. Scheerlinck, F. Van Laere, J. Schrauwen, D. Taillaert, D. Van Thourhout, R. Baets, Gold grating coupler for silicon-on-insulator waveguides with 34 % coupling efficiency, *13th European Conference on Integrated Optics (ECIO)*, Copenhagen, Denmark, 2007.
12. F. Van Laere, T. Stomeo, M. Ayre, C. Cambournac, H. Benisty, D. Van Thourhout, T.F. Krauss, R. Baets, Multifunctional photonic crystal compact demux-detector on InP, *Optical Fiber Communications (OFC)*, San Diego, United States, p.OThM5, 2008.
13. F. Van Laere, D. Van Thourhout, R. Baets, T. Stomeo, T.F. Krauss, M. Ayre, C. Cambournac, H. Benisty, R. Brenot, Grating coupled photonic crystal demultiplexer with integrated detectors on InP-membrane, *International Conference on Indium Phosphide and related materials (IPRM)*, Versailles, France, p. MoB3.4, 2008.
14. H. Benisty, C. Cambournac, M. Ayre, F. Van Laere, D. Van Thourhout, R. Baets, T. Stomeo, T.F. Krauss, M. Kamp, H. Hoffman, A. Forchel, D.F.G. Gallagher, Functional photonic-crystal mini-stopband demux integrated in emitting and detecting devices, *14th European Conference on Integrated Optics (ECIO)*, Eindhoven, The Netherlands, p.O.044, 2008.
15. T. Stomeo, T.F. Krauss, F. Van Laere, D. Van Thourhout, R. Baets, C. Cambournac, M. Ayre, H. Benisty, Successful fabrication and integration of multifunctional photonic-crystal devices

on bonded InP membrane chip, *14th European Conference on Integrated Optics (ECIO)*, Eindhoven, The Netherlands, p.O.067, 2008.

16. F. Bordas, F. Van Laere, G. Roelkens, E.J. Geluk, F. Karouta, P. J. Van Veldhoven, R. Nötzel, D. Van Thourhout, R. Baets, M.K. Smit, Compact grating coupled MMI on DVS-BCB bonded InP-membrane, *14th European Conference on Integrated Optics (ECIO)*, Eindhoven, The Netherlands, p.O.024, 2008.

17. F. Van Laere, W. Bogaerts, P. Dumon, G. Roelkens, D. Van Thourhout, R. Baets, Focusing polarization diversity gratings for Silicon-on-Insulator integrated circuits, *5th International Conference on Group IV Photonics*, Sorrento, Italy, p.ThB3, 2008.

18. H. Benisty, C. Cambournac, O. Khayam, M. Ayre, F. Van Laere, D. Van Thourhout, R. Baets, T. Stomeo, T.F. Krauss, M. Kamp, H. Hofmann, A. Forchel, D.F.G. Gallagher, Compact integrated photonic crystal demultiplexer for emitting and receiving InP photonic integrated circuits, *European Conference on Optical Communication (ECOC)*, Brussels, Belgium, p.Th2D4, 2008.

B.3 International Workshops

1. F. Van Laere, Compact grating couplers in InP, *ePIXnet Winter School, Optoelectronic Integration - Technology and Applications*, Pontresina, Switzerland, 2006.

2. F. Van Laere, Compact grating couplers and wavelength monitoring in BCB-bonded InP-membranes,*WAPITI-PICMOS workshop*, Halle, Germany, 2006.

3. P. Bienstman, F. Van Laere, D. Taillaert, P. Dumon, W. Bogaerts, K. De Vos, D. Van Thourhout, R. Baets, High index-contrast silicon-on-insulator nanophotonics, *PPCM*, Belgium, p.4, 2006

4. F. Van Laere, T. Stomeo, M. Ayre, D. Taillaert, D. Van Thourhout, T. F. Krauss, R. Baets, Polarization diversity and wavelength monitoring in BCB-bonded InP-membranes, *ePIXnet Winter School - Applications of Photonic Integration*, Pontresina, Switzerland, 2007.

5. F. Van Laere, T. Stomeo, D. Taillaert, D. Van Thourhout, T. F. Krauss, R. Baets, Polarization diversity grating couplers in

bonded InP-membranes, *PECS VII*, Monterey, United States, 2007.

B.4 National Conference Proceedings

1. F. Van Laere, M. Ayre, D. Taillaert, D. Van Thourhout, T.F. Krauss, R. Baets, Realisation of compact and efficient fiber couplers in InP-membrane, *6th FirW PhD Symposium*, Belgium, nr. 26, 2005.

2. F. Van Laere, M. Ayre, D. Taillaert, D. Van Thourhout, T.F. Krauss, R. Baets, Compact and efficient fibre-to-waveguide grating couplers in InP-membrane, *IEEE/LEOS Symposium Benelux Chapter*, Mons, Belgium, 2005.

3. J. Schrauwen, F. Van Laere, D. Van Thourhout, R. Baets, Focused-ion-beam fabrication of slanted fiber couplers in silicon-on-insulator waveguides, *IEEE/LEOS Symposium Benelux Chapter*, Eindhoven, The Netherlands, 2006.

4. S. Scheerlinck, J. Schrauwen, F. Van Laere, D. Van Thourhout, R. Baets, Metal grating coupler for Silicon-on-Insulator, *Annual Workshop of the IEEE/LEOS Benelux Student Chapter*, The Netherlands, 2007.

5. F. Van Laere, T. Stomeo, D. Van Thourhout, T. F. Krauss R. Baets, Efficient polarization independent link in bonded InP-membrane, *8th FirW PhD Symposium*, Belgium, p. 50, 2007.

B.5 Awards

1. Second poster prize at the ePIXnet Winter School, Optoelectronic Integration - Technology and Applications, Pontresina, Switzerland, 2006.

2. First prize winner of the Corning Outstanding Student Paper Award Competition at the Optical Fiber Communications Conference (OFC) 2008, San Diego, USA with a paper entitled "Multifunctional photonic crystal compact demux-detector on InP.

Bibliography

[1] A. Sano, H. Masuda, Y. Kisaka, S. Aisawa, E. Yoshida, Y. Miyamoto, M. Koga, K. Hagimoto, T. Yamada, F. Furuta and H. Fukuyama. 14-Tb/s (140 x 111-Gb/s PDM/WDM) CSRZ-DQPSK transmission over 160 km using 7-THz bandwidth extended L-band EDFAs. In *European Conference on Optical Communication (ECOC)*, page Th4.1.1, 2006.

[2] G. K. Celler and S. Cristoloveanu. Frontiers of silicon-on-insulator. *Journal of Applied Physics*, 93(9):4955, 2003.

[3] Y. Akahane, T. Asano, B. S. Song and S. Noda. High-Q photonic nanocavity in a two-dimensional photonic crystal. *Nature*, 425(6961):944–947, 2003.

[4] T. Tanabe, M. Notomi, E. Kuramochi, A. Shinya and H. Taniyama. Trapping and delaying photons for one nanosecond in an ultrasmall high-Q photonic-crystal nanocavity. *Nature Photonics*, 1(1):49–52, 2007.

[5] M. Settle, M. Salib, A. Michaeli and T. F. Krauss. Low loss silicon on insulator photonic crystal waveguides made by 193 nm optical lithography. *Optics Express*, 14(6):2440–2445, 2006.

[6] W. Bogaerts, P. Dumon, D. Van Thourhout, D. Taillaert, P. Jaenen, J. Wouters, S. Beckx, V. Wiaux and R. Baets. Compact wavelength-selective functions in Silicon-on-Insulator photonic wires. *Journal of Selected Topics in Quantum Electronics*, 12(6):1394–1401, 2006.

[7] M. Rouviere, L. Vivien, X. Le Roux, J. Mangeney, P. Crozat, C. Hoarau, E. Cassan, D. Pascal, S. Laval, J. M. Fedeli, J. F. Damlencourt, J. M. Hartmann and S. Kolev. Ultrahigh speed germanium-

on-silicon photodetectors for 1.31 and 1.55 micron operation. *Applied Physics Letters*, 87(23):231109–231111, 2005.

[8] G. Masini, G. Capellini, J. Witzens and C. Gunn. A four-channel, 10 Gbps monolithic optical receiver in 130 nm CMOS with integrated Ge waveguide detectors. In *Optical Fiber Communications 2007*, page PDP31, 2007.

[9] Q. F. Xu, B. Schmidt, S. Pradhan and M. Lipson. Micrometre-scale silicon electro-optic modulator. *Nature*, 435(7040):325–327, 2005.

[10] H. S. Rong, A. S. Liu, R. Jones, O. Cohen, D. Hak, R. Nicolaescu, A. Fang and M. Paniccia. An all-silicon Raman laser. *Nature*, 433(7023):292–294, 2005.

[11] M. A. Green, J. H. Zhao, A. H. Wang, P. J. Reece and M. Gal. Efficient silicon light-emitting diodes. *Nature*, 412(6849):805–805, 2001.

[12] C. Seassal, C. Monat, J. Mouette, E. Touraille, B. Ben Bakir, H. T. Hattori, J-L. Leclercq, X. Letartre, P. Rojo-Romeo and P. Viktorovitch. InP bonded membrane photonics components and circuits: Toward 2.5 dimensional micro-nano-photonics. *Journal of Selected Topics in Quantum Electronics*, 11(2):395–407, 2005.

[13] O. Painter, R. K. Lee, A. Scherer, A. Yariv, J. D. O'Brien, P. D. Dapkus and I. Kim. Two-dimensional photonic band-gap defect mode laser. *Science*, 284:1819–1821, 1999.

[14] E. Tangdiongga, Y. Liu, J. H. Den Besten, M. van Geemert, T. Van Dongen, J. J. M. Binsma, H. De Waardt, G. D. Khoe, M. K. Smit and H. J. S. Dorren. Monolithically integrated 80-Gb/s AWG-based all-optical wavelength converter. *IEEE Photonics Technology Letters*, 18(15):1627–1629, 2006.

[15] M. Galarza, D. Van Thourhout, R. Baets and M. Lopez-Amo. Compact and highly-efficient polarization independent vertical resonant couplers for active-passive monolithic integration. *Optics Express*, 16(12):8350–8358, 2008.

[16] V. M. Menon, F. Xia and S. R. Forrest. Photonic integration using asymmetric twin-waveguide technology: Part II-Devices. *IEEE Journal of Selected Topics in Quantum Electronics*, 11(1):30–42, 2005.

[17] T. Van Caenegem, D. Van Thourhout, M. Galarza, S. Verstuyft, I. Moerman, P. Van Daele, R. Baets, P. Demeester, C. G. P. Herben, X. J. M. Leijtens and M. K. Smit. Monolithically integrated multi-wavelength laser by selective area growth with metal organic vapour phase epitaxity. *Electronics Letters*, 37(5):296–298, 2001.

[18] J. Dubowski, Y. Feng, P. Poole, M. Buchanan, S. Poirier, J. Genest and V. Aimez. Monolithic multiple wavelength ridge waveguide laser array fabricated by Nd:YAG laser induced quantum well intermixing. *Journal of Vacuum Science Technology*, A20(4):1426–1429, 2002.

[19] X. Yan, M. L. Masanovic, E. J. Skogen, Z. Hu, D. J. Blumenthal and L. A. Coldren. Optical mode converter integration with InP-InGaAsP active and passive waveguides using a single regrowth process. *IEEE Photonics Technology Letters*, 14(9):1249–1251, 2002.

[20] http://www.infinera.com/.

[21] R. Nagarajan *et al*. 400 Gbit/s (10 channel x 40 Gbit/s) DWDM photonic integrated circuits. *Electronics Letters*, 41(6):347–349, 2005.

[22] T. Mitze, M. Schnarrenberger, L. Zimmermann, J. Bruns, F. Fidorra, J. Kreissl, K. Janiak, S. Fidorra, H. Heidrich and K. Petermann. Hybrid integration of III/V lasers on a silicon-on-insulator optical board. In *Group IV Photonics*, pages 210–212, 2005.

[23] http://www.luxtera.com/.

[24] D. Fehly, A. Schlachetzki, A. S. Bakin, A. Guttzeit and H. H. Wehmann. Monolithic InGaAsP optoelectronic devices with silicon. *Optics Express*, 37(10):1246–1252, 2001.

[25] G. Roelkens, D. Van Thourhout, R. Baets, R. Nötzel and M. K. Smit. Laser emission and photodetection in an InP/InGAAsP layer integrated on and coupled to a Silicon-on-Insulator waveguide circuit. *Optics Express*, 14(18):8154–8159, 2006.

[26] A. W. Fang, R. Jones, H. Park, O. Cohen, O. Raday, M. J. Paniccia and J. E. Bowers. Integrated AlGaInAs-silicon evanescent racetrack laser and photodetector. *Optics Express*, 15(5):2315–2322, 2007.

[27] I. Moerman, P. P. Van Daele and P. M. Demeester. A review on fabrication technologies for the monolithic integration of tapers with III-V semiconductor devices. *IEEE Journal of Selected Topics in Quantum Electronics*, 3(6):1308–1320, 1997.

[28] N. Yoshimoto, K. Kawano, H. Takeuchi, S. Kondo, and Y. Noguchi. Spot size convertors using InP/InAlAs multiquantum well waveguides for low-loss singlemode fiber coupling. *Electronics Letters*, 28(17):1610–1611, 1992.

[29] R. Zengerle, O. Leminger, W. Weiershausen, K. Faltin and B. Hübner. Laterally tapered InP-InGaAsP waveguides for low-loss chip-to-fiber butt coupling: a comparison of different configurations. *IEEE Photonics Technology Letters*, 7(5):532–534, 1995.

[30] A. Sure, T. Dillon, J. Murakowski, C. Lin, D. Pustai and D. W. Prather. Fabrication and characterization of three-dimensional silicon tapers. *Optics Express*, 11(36):3555–3561, 2003.

[31] T. Shoji, T. Tsuchizawa, T. Watanabe, K. Yamada and H. Morita. Low loss mode size converter from 0.3 μm square Si wire waveguides to singlemode fibres. *Electronics Letters*, 38(25):1669–1670, 2002.

[32] S. McNab, N. Moll and Y. Vlasov. Ultra-low loss photonic integrated circuit with membrane-type photonic crystal waveguides. *Optics Express*, 11(22):2927–2939, 2003.

[33] V. R. Almeida, R. R. Panepucci and M. Lipson. Nanotaper for compact mode conversion. *Optics Letters*, 28(15):1302–1304, 2003.

[34] G. Z. Masanovic, G. T. Reed, W. Headley, B. Timotijevic, V. M. N. Passaro, R. Atta, G. Ensell and A. G. R. Evans. A high efficiency input/output coupler for small silicon photonic devices. *Optics Express*, 13(19):7374–7379, 2005.

[35] T. W. Ang, G. T. Reed, A. Vonsovici, A. G. R. Evans, P. R. Routley and M. R. Josey. Effects of grating heights on highly efficient unibond SOI waveguide grating couplers. *IEEE Photonics Technology Letters*, 12(1):59–61, 2000.

[36] R. Orobtchouk, A. Layadi, H. Gualous, D. Pascal, A. Koster and S. Laval. High-efficiency light coupling in a submicrometric silicon-on-insulator waveguide. *Applied Optics*, 39(31):5773–5777, 2000.

[37] S. Lardenois, D. Pascal, L. Vivien, E. Cassan, S. Laval, R. Orobtchouk, M. Heitzmann, N. Bouzaida and L. Mollard. Low-loss submicrometer silicon-on-insulator rib waveguides and corner mirrors. *Optics Letters*, 28(13):1150–1152, 2003.

[38] B. Wang, J. H. Jiang and G. P. Nordin. Embedded, slanted grating for vertical coupling between fibers and silicon-on-insulator planar waveguides. *IEEE Photonics Technology Letters*, 17(9):1884–1886, 2005.

[39] Dirk Taillaert. *Grating couplers as interface between optical fibres and nanophotonic waveguides*. PhD thesis, Ghent University, 2004.

[40] J. B. D. Soole, M. R. Amersfoort, H. P. LeBlanc, N. C. Andreadakis, A. Rajhel, C. Caneau, M. A. Koza, R. Bhat, C. Youtsey and I. Adesida. Polarization independent InP arrayed waveguide filter using square cross-section waveguides. *Electronics Letters*, 32(4):323–324, 1996.

[41] G. T. Reed, G. Z. Mashanovic, W. R. Headley, B. Timotijevic, F. Y. Gardes, S. P. Chan, P. Waugh, N. G. Emerson, C. E. Png, M. J. Paniccia, A. Liu, D. Hak and V. M. N. Passaro. Issues associated with polarization independence in silicon photonics. *IEEE Journal of Selected Topics in Quantum Electronics*, 12(6):1335–1343, 2006.

[42] H. Takahashi, Y. Hibino and I. Nishi. Polarization-insensitive arrayed waveguide grating wavelength multiplexer on silicon. *Optics Letters*, 17(7):499–501, 1992.

[43] H. Bissessur, F. Gaborit, B. Martin, P. Pagnod-Rossiaux, J. L. Peyre and M. Renaud. 16 channel phased-array wavelength demultiplexer on InP with low polarization sensitivity. *Electronics Letters*, 30(4):336–337, 1994.

[44] M. Zirngibl, C. H. Joyner and P. C. Chou. Polarisation compensated waveguide grating router on InP. *Electronics Letters*, 31(19):1662–1664, 1995.

[45] H. H. Yaffe, C. H. Henry, R. F. Kazarinov and M. A. Milbrodt. Polarisation-independent silica-on-silicon mach-zehnder interferometers. *Journal of Lightwave Technology*, 12(1):64–67, 1994.

[46] J.-J. He, E. S. Koteles, B. Lamontagnem, L. Erickson, A. Delage and M. Davies. Integrated polarization compensator for WDM

waveguide demultiplexers. *IEEE Photonics Technology Letters*, 11(2):224–226, 1999.

[47] N. Zhu, J. Song, L. Wosinski and S. He. Design of a polarization-insensitive echelle grating demultiplexer based on silicon nanophotonic wires. *IEEE Photonics Technology Letters*, 20(10):860–862, 2008.

[48] T. Barwicz, M. R. Watts, M. A. Popovic, P. T. Rakich, L. Socci, F. X. Kärtner, E. P. Ippen and H. I. Smith. Polarization-transparent microphotonic devices in the strong confinement limit. *Nature Photonics*, 1(1):57–60, 2007.

[49] H. Fukuda, K. Yamada, T. Tsuchizawa, T. Watanabe, H. Shinojima and S. Itabashi. Silicon photonic circuit with polarization diversity. *Optics Express*, 16(7):4872–4880, 2008.

[50] J. J. G. M. van der Tol, J. W. Pedersen, E. G. Metaal, F. Hakimzadeh, Y. S. Oei, F. H. Groen and I. Moerman. Realization of a short integrated optic passive polarization converter. *IEEE Photonics Technology Letters*, 7(8):1286–1288, 1995.

[51] L. M. Augustin, R. Hanfoug, J. J. G. J. van der Tol, W. J. M. de Laat, M. K. Smit. A compact integrated polarization splitter/converter in InGaAsP-InP. *IEEE Photonics Technology Letters*, 19(17):1286–1288, 2007.

[52] M. V. Kotlyar, L. Bolla, M. Midrio, L. O'Faolain and T. F. Krauss. Compact polarization converter in InP-based material. *Optics Express*, 13(13):5040–5045, 2005.

[53] I. Kiyat, A. Aydinli and N. Dagli. A compact silicon-on-insulator polarization splitter. *IEEE Photonics Technology Letters*, 17(1):100–102, 2005.

[54] Y. Ma and D. Huang. A compact silicon-on-insulator MMI-based polarization splitter. In *2007 IEEE/LEOS International Conference on Optical MEMS and Nanophotonics*, page TuP34, 2007.

[55] Z. Wang and D. Dai. Ultrasmall si-nanowire-based polarization rotator. *JOSA B*, 25(5):747–753, 2005.

[56] D. Taillaert, H. Chong, P. Borel, L. Frandsen, R. M. De La Rue and R. Baets. A compact two-dimensional grating coupler used as a

polarization splitter. *IEEE Photonics Technology Letters*, 15(9):1249–1251, 2003.

[57] M. L. Dakss, L. Kuhn, P. F. Heidrich and B. A. Scott . Grating coupler for efficient excitation of optical guided waves in thin films. *Applied Physics Letters*, 16(12):523–525, 1970.

[58] H. Kogelnik and T. P. Sosnowski . Holographic thin film couplers. *The Bell System Technical Journal*, 49(7):1602–1608, 1970.

[59] T. Tamir and S. T. Peng . Analysis and design of grating couplers. *Applied Physics*, 14(3):235–254, 1977.

[60] T. Tamir. *Topics in Applied Physics: Integrated Optics*. Springer-Verlag New York Heidelberg Berlin, 1979.

[61] R. Waldhäusl, B. Schnabel, P. Dannberg, E-B. Kley, A. Bräure and W. Karthe. Efficient coupling into polymer waveguides by gratings. *Applied Optics*, 36(36):9383–9390, 1997.

[62] Peter Bienstman. *Rigorous and efficient modelling of wavelength scale photonic components*. PhD thesis, Ghent University, 2001.

[63] http://www.photond.com/products/omnisim.htm.

[64] T. Suhara and H. Nishihara. Integrated-optics components and devices using periodic structures. *IEEE Journal of Quantum Electronics*, 22(6):845–867, 1986.

[65] R. M. Emmons and D. G. Hall, . Buried-oxide Silicon-on-Insulator structures. 2. Waveguide grating couplers. *IEEE Journal of Quantum Electronics*, 28(1):164–175, 1992.

[66] G. Roelkens, D. Van Thourhout and R. Baets. High efficiency silicon-on-insulator grating coupler based on a poly-silicon overlay. *Optics Express*, 14(24):11622–11630, 2006.

[67] Bert Luyssaert. *Compact Planar Waveguide Spot-Size Converters in Silicon-on-Insulator*. PhD thesis, Ghent University, 2005.

[68] personal communication with Wim Bogaerts.

[69] B. Wang, J. H. Jiang and G. P. Nordin. Compact slanted grating couplers. *Optics Express*, 12(15):3313–3326, 2004.

[70] M. Hagberg, N. Eriksson and A. Larsson. Investigation of high-efficiency surface-emitting lasers with blazed grating outcouplers. *IEEE Journal of Quantum Electronics*, 32(9):1596–1605, 1996.

[71] R. J. Shul and S. J. Pearton. *Handbook of advanced plasma processing techniques*. Springer-Verlag Berlin Heidelberg, 2000.

[72] M. V. Kotlyar, L. O'Faolain, R. Wilson and T. F. Krauss . High-aspect-ratio chemically assisted ion-beam etching for photonic crystals using a high beam voltage-current ratio. *Journal of Vacuum Science and Technology B*, 22(4):1788–1791, 2004.

[73] K. Hjort. Sacrificial etching of III-V compounds for micromechanical devices. *Journal of Micromechanics and Microengineering*, 6(4):370–375, 1996.

[74] C.-J. Kim, J. Y. Kim and B. Sridharan. Comparative evaluation of drying techniques for surface micromachining. *Sensors and Actuators A: Physical*, 64(1):17–26, 1998.

[75] C. T. Pan, H. Yang, S. C. Shen, M. C. Chou and H. P. Chou. A low-temperature wafer bonding technique using patternable materials. *Journal of Micromechanics and Microengineering*, 12(5):611–615, 2002.

[76] W. P. Eaton, S. H. Risbud and R. L. Smith. Silicon wafer-to-wafer bonding at T-less-than-200-degrees-C with polymethylmethacrylate. *Applied Physics Letters*, 65(4):439–441, 1994.

[77] H. Lin, K. Chang, G. W. Pickrell, K. Hsieh and K. Cheng. Low temperature wafer bonding by spin on glass. *Journal of Vacuum Science and Technology B*, 20(2):752–754, 2002.

[78] Ilse Christiaens. *Vertically Coupled Microring Resonators Fabricated with Wafer Bonding*. PhD thesis, Ghent University, 2005.

[79] Günther Roelkens. *Heterogeneous III-V/Silicon Photonics: Bonding Technology and Integrated Devices*. PhD thesis, Ghent University, 2007.

[80] Wim Bogaerts. *Nanophotonic Waveguides and Photonic Crystals in Silicon-on-Insulator*. PhD thesis, Ghent University, 2004.

[81] P. Dumon, W. Bogaerts, V. Wiaux, J. Wouters, S. Beckx, J. Van Campenhout, D. Taillaert, B. Luyssaert, P. Bienstman, D. Van Thourhout, and R. Baets. Low-loss SOI photonic wires and ring resonators fabricated with Deep UV lithography. *IEEE Photonics Technology Letters*, 16(5):1328–1330, 2004.

[82] M. Gnan, S. Thomas, D. S. Macintyre, R. M. De La Rue and M. Sorel. Fabrication of low-loss photonic wires in silicon-on-insulator using hydrogen silsesquioxane electron-beam resist. *Electronics Letters*, 44(2):115–116, 2008.

[83] D. Lauvernier, S. Garidel, M. Zegaoui, J. P. vilcot, D. Decoster. GaAs/polymer optical nanowires: fabrication and characterisation. *Electronics Letters*, 42(4):217–219, 2006.

[84] D. P. Kelly, M. W. Pruessner, K. Amarnath, M. Datta, S. Kanakaraju, L. C. Calhoun and R. Ghodssi. Monolithic suspended optical waveguides for InP MEMS. *IEEE Photonics Technology Letters*, 16(5):1298–1300, 2004.

[85] J. D. Joannopoulos, R. D. Meade and J. N. Winn. *Photonic crystals: molding the flow of light*. Princeton university press, 1995.

[86] E. Kuramochi, M. Notomi, S. Hughes, A. Shinya, T. Watanabe and L. Ramunno. Disorder-induced scattering loss of line-defect waveguides in photonic crystal slabs. *Physical Review B*, 72(16):161318, 2005.

[87] E. Kuramochi, M. Notomi, S. Mitsugi, A. Shinya, T. Tanabe and T. Watanabe. Ultrahigh-Q photonic crystal nanocavities realized by the local width modulation of a line defect. *Applied Physics Letters*, 88:041112, 2006.

[88] S. Combrie, E. Weidner, A. DeRossi, S. Bansropun and S. Cassette. Detailed analysis by Fabry-Perot method of slab photonic crystal line-defect waveguides and cavities in aluminium free material system. *Optics Express*, 14(16):7353–7361, 2006.

[89] A. Talneau, K. H. Lee, S. Guilet and I. Sagnes. Efficient coupling to W1 photonic crystal waveguide on InP membrane through suspended access guides. *Applied Physics Letters*, 92:061105, 2008.

[90] P. Dumon. *Ultra-compact integrated Optical filters in silicon-on-insulator by means of wafer-scale technology*. PhD thesis, Ghent University, 2007.

[91] O. Schwelb. Transmission, group delay, and dispersion in single-ring optical resonators and add/drop filters- A tutorial overview. *Journal of lightwave technology*, 22(5):1380–1394, 2004.

[92] G. Priem. *Nonlinear behaviour in nanophotonic waveguides and resonators for ultrafast signal processing*. PhD thesis, Ghent University, 2006.

[93] G. R. A. Priem, P. Dumon, W. Bogaerts, D. Van Thourhout, G. Morthier and R. Baets. Optical bistability and pulsating bahaviour in Silicon-on-Insulator ring resonator structures. *Optics Express*, 13(23):9623–9628, 2005.

[94] G. Roelkens, L. Liu, D. Van Thourhout, R. Baets, R. Nötzel, F. Raineri, I. Sagnes, G. Beaudoin and R. Raj. Light emission and enhanced nonlinearity in nanophotonic waveguide circuits by III-V/silicon-on-insulator heterogeneous integration. *Journal of Applied Physics*, 104:033117, 2008.

[95] L. B. Soldano and E. C. M. Pennings. Optical multi-mode interference devices based on self-imaging: principles and applications. *Journal of Lightwave Technology*, 13(4):615–627, 1995.

[96] http://www.photond.com/products/fimmwave.htm.

[97] E. Viasnoff-Schwoob, C. Weisbuch, H. Benisty, C. Cuisin, E. Derouin, O. Drisse, G-H. Duan, L. Legouézigou, S. Golka, H. Heidrich, H. J. Hensel and K. Janiak. Compact wavelength monitoring by lateral outcoupling in wedged photonic crystal multimode waveguides. *Applied Physics Letters*, 86:101107, 2005.

[98] L. Martinelli, H. Benisty, O. Khayam, G. H. Duan, H. Heidrich and K. Janiak. Analysis and optimization of compact demultiplexer monitor based on photonic crystal waveguide. *IEEE Journal of Lightwave Technology*, 25(9):2385–2394, 2007.

[99] L. Martinelli, H. Benisty, O. Drisse, E. Derouin, F. Pommereau, O. Legouzigou and G. H. Duan. Impact of lithographic grid irregularity assessed on photonic crystal device selectivity. *IEEE Photonics Technology Letters*, 19(5):282–284, 2007.

[100] S. Olivier, H. Benisty, C. J. M. Smith, M. Rattier, C. Weisbuch and T. F. Krauss. Transmission properties of two-dimensional photonic crystal channel waveguides. *Optical and Quantum Electronics*, 34(1-3):171–181, 2002.

[101] R. J. Deri. Monolithic integration of optical waveguide circuitry with III-V photodetectors for advanced lightwave receivers. *Journal of Lightwave Technology*, 11(8):1296–1313, 1993.

[102] A. W. Snyder and J. D. Love. *Optical waveguide theory*. Chapman and Hall, 1983.

[103] http://ab initio.mit.edu/wiki/index.php/Meep.

[104] H. C. Lefevre . Single-mode fiber fractional wave devices and polarization controllers. *Electronics Letters*, 16(20):778–780, 1980.

[105] W. Bogaerts, D. Taillaert, P. Dumon, D. Van Thourhout, R. Baets and E. Pluk. A polarization-diversity wavelength duplexer circuit in silicon-on-insulator photonic wires. *Optics Express*, 15(4):1567–1578, 2007.

[106] G. P. Agrawal. *Fiber-optic communication systems*. John Wiley & Sons, 2002.

[107] G. L. Abbas, V. W. S. Chan and T. K. Yee. A dual detector optical heterodyne receiver for local oscillator noise suppression. *Journal of Lightwave Technology*, LT-3(5):1110–1122, 1985.

[108] T. Okoshi. Polarization-state control schemes for heterodyne or homodyne optical fiber communications. *Journal of Lightwave Technology*, 3(6):1232–1237, 1985.

[109] M. W. Maeda and D. A. Smith. New polarization-insensitive direction scheme based on fiber polarization scrambling. *Electronics Letters*, 27(1):10–12, 1991.

[110] L. G. Kazovsky. Phase- and polarization-diversity coherent optical techniques. *Journal of Lightwave Technology*, 7(2):279–291, 1989.

[111] L. D. Tzeng, W. L. Emkey C. A. Jack. Polarization-insensitive coherent receiver using a double balanced optical hybrid system. *Electronics Letters*, 23(22):1195–1196, 1987.

[112] B. Glance. Polarization independent coherent optical receiver. *Journal of Lightwave Technology*, LT-5(2):274–276, 1987.

[113] T. L. Koch, U. Koren, R. P. Gnall, F. S. Choa, F. Hernandez-Gil, C. A. Burrus, M. G. Young, M. Oron B. I. Miller. GaInAs/GaInAsP multiple-quantum-well integrated heterodyne receiver. *Electronics Letters*, 25(24):1621–1623, 1989.

[114] H. Takeuchi, K. Kasaya, Y. Kondo, H. Yasaka, K. OE and Y. Imamura. Monolithic integrated coherent receiver on InP-substrate. *IEEE Photonics Technology Letters*, 1(11):398–400, 1989.

[115] F. Xia, S. Datta and S. R. Forrest. A monolithically integrated optical heterodyne receiver. *IEEE Photonics Technology Letters*, 17(8):1716–1718, 2005.

[116] R. Kaiser, D. Trommer, F. Fidorra, H. Heidrich, S. Malchow, D. Franke, W. Passenberg, W. Rehbein, H. Schroeter-Janβen, R. Stenzel and G. Unterbörsch. Monolithically integrated polarisation diversity heterodyne receivers on GaInAsP. *Electronics Letters*, 30(17):1446–1447, 1994.

[117] R. J. Deri, E. C. M. Pennings, A. Scherer, A. S. Gozdz, C. Caneau, N. C. Andreadakis, V. Shah, L. Curtis, R. J. Hawkins, J. B. D. Soole and J.-I. Song. Ultracompact monolithic integration of balanced, polarization diversity phototdetectors for coherent lightwave receivers. *IEEE Photonics Technology Letters*, 4(11):1238–1240, 1992.

[118] R. J. Deri, R. Welter, E. C. M. Pennings, C. Caneau, J. L. Jackel, R. J. Hawkins, J. J. Johnson, H. Gilchrist and C. Gibbons. High-speed heterodyne operation of monolithically integrated balanced polarisation diversity photodetectors. *Electronics Letters*, 28(25):2332–2334, 1992.

[119] P.R.A. Binetti, X.J.M. Leijtens, M. Nikoufard, T. de Vries, Y.S. Oei, L. Di Cioccio, J.-M. Fedeli, C. Lagahe, R. Orobtchouk, C. Seassal, J. Van Campenhout, D. Van Thourhout, P.J. Van Veldhoven, R. Nötzel and M.K. Smit. InP-based membrane photodetectors for optical interconnects to Si. In *4^{th} International Conference on Group IV Photonics, Tokyo, Japan*, page WB4, 2007.

[120] G.-K. Chang, W.-P. Hong, J. L. Gimlett, R. Bhat and C. K. NGuyen. High-performance monolithic dual-MSM photodetector for long-

wavelength coherent receivers. *Electronics Letters*, 25(16):1021–1023, 1989.

[121] T. L. Koch and U. Koren. Semiconductor photonic integrated circuits. *IEEE Journal of Quantum Electronics*, 27(3):641–653, 1991.

[122] G. Roelkens, D. Van Thourhout and R. Baets. High efficiency grating couplers between silicon-on-insulator waveguides and perfectly vertical optical fibers. *Optics Letters*, 32(11):1495–1497, 2007.

[123] E. Hallynck. Optimalisatie van roosterkoppelaars tussen optische vezel en nanofotonische componenten. Master's thesis, Ghent University, 2008.